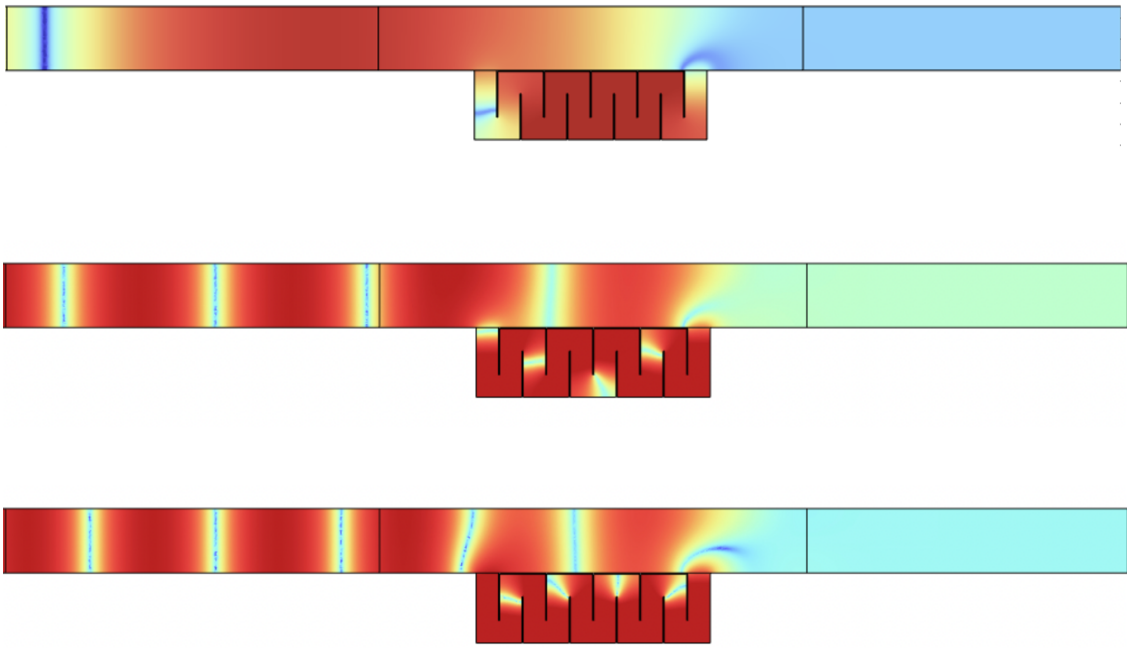

Design and Simulation of Acoustic Metamaterials for Noise Reduction in Open-Flow Systems

Master's thesis in Mechanics and Maritime Sciences

Chenya Ji
Prajwal S Reddy

DEPARTMENT OF Mechanics and Maritime Sciences

CHALMERS UNIVERSITY OF TECHNOLOGY
Gothenburg, Sweden 2024
www.chalmers.se

Master's thesis 2024

Design and Simulation of Acoustic Metamaterials for Noise Reduction in Open-Flow Systems

Chenya Ji
Prajwal S Reddy

CHALMERS
UNIVERSITY OF TECHNOLOGY

Department of Mechanics and Maritime Sciences
Chalmers University of Technology
Gothenburg, Sweden 2024

Design and Simulation of Acoustic Metamaterials for Noise Reduction in Open-Flow Systems
Chenya Ji
Prajwal S Reddy

Supervisors:
Wei Na, Volvo Group Trucks Technology
Christina Keulemans Westlin, Volvo Group Trucks Technology
Examiner:
Huadong Yao, Mechanics and Maritime Sciences

Master's Thesis 2024
Department of Mechanics and Maritime Sciences
Chalmers University of Technology
SE-412 96 Gothenburg

Cover: The simulated sound pressure levels in an exhaust pipe with a metamaterial cell at frequencies of 330 Hz, 1210 Hz, and 1360 Hz

Typeset in LaTeX
Printed by Chalmers Reproservice
Gothenburg, Sweden 2024

Design and Simulation of Acoustic Metamaterials for Noise Reduction in Open-Flow Systems
Chenya Ji
Prajwal S Reddy
Department of Mechanics and Maritime Sciences
Chalmers University of Technology

Abstract

The growing demand for larger and more efficient cooling systems in heavy-duty trucks has led to increased noise levels, particularly from cooling fans, which poses challenges to both environmental standards and user comfort. Conventional techniques for sound absorption typically restrict particle motion, which will also impede flow and increase temperature in a situation when fans are present. Acoustic metamaterial (AMM) solutions have been explored to address these problems.

A systematic methodology for designing a single metamaterial cell is presented, encompassing four stages: specification of geometrical parameters, parametrization, parametric design, and optimization. Noise characterization of a vehicle's cooling fan, based on Lu's study[20], revealed broadband noise and tonal harmonics centred on the blade passing frequency (BPF).

In response, a double-layer micro-perforated panel (DLMPP) structure was designed to reduce noise over a broad frequency range; a space-coiling structure was created to target specific tonal noise. Theoretical calculations show that both structures have excellent noise absorption performance. Simulations of the space-coiling cell with a flow field were then conducted. Although the absorption coefficients show slight deviations from theoretical calculations, the results remain promising for this study and warrant further investigation. A simulation of an under-cab environment was also studied by applying the acoustic impedance of DLMPP on target surfaces under conditions with and without flow. The results demonstrate that the present AMMs can significantly reduce cooling fan noise while maintaining thermal management efficiency.

Keywords: cooling fan noise, acoustic metamaterial design, acoustics metamaterial simulation, broadband noise reduction, tonal noise reduction, computational fluid dynamics, passive noise control, aeroacoustics, micro-perforated panel, space-coiling structure

Acknowledgements

We would like to express our deepest gratitude to all those who supported us throughout the course of this thesis. First and foremost, we want to thank our supervisors, Huadong Yao and Wei Na, for their invaluable guidance, insightful feedback, and continuous encouragement during this research. Their expertise and advice were essential in shaping the direction of this work. We would also like to extend our appreciation to Volvo GTT for providing the necessary resources and support that made this thesis possible. Special thanks to the research group and colleagues for their camaraderie, helpful discussions, and assistance during challenging moments.

Prajwal's Acknowledgements

A heartfelt thank you goes to my family and friends for their unwavering emotional support, patience, and understanding throughout this journey. Your belief in me kept me motivated and focused.

Finally, I am grateful to all those who contributed to this work, directly or indirectly, for their assistance and support.

Prajwal S Reddy, Gothenburg, 2024

Chenya's Acknowledgements

My gratitude extends to all people at the Division of Applied Acoustics. Especially Wolfgang Kropp, his selfless contribution and unwavering support always give me priceless insights. Thanks, Alexander Lendon, Rushi Ganapathi Apadanda, Vincent Ratay and all of my colleagues, who are also close friends of mine, have given me a wealth of knowledge over this trip. I am grateful that I had Wen by my side at the crossroads of life. Her wise counsel gave me a positive path to pursue my acoustics career.

I want to express my most special thanks to my dearest friend, Jiali Cheng. A work like this will never be grounded without her strong support for the past two years.

Lastly, I am eternally grateful to my family and friends in China for their unconditional love and support every single day.

Chenya Ji, Gothenburg, 2024

Artificial Intelligence Tool Disclosure

- The grammar and typos of some sentences are checked and polished with Chat-GPT 4 and Quillbot.
- No longer sections of text have been generated or rewritten entirely by artificial intelligence.
- No data processed from any artificial intelligence.
- No graphs, schemes or photographs generated from artificial intelligence.
- No code generated from artificial intelligence.
- No models created by artificial intelligence.

Statement of Contribution

The work was distributed between Chenya Ji(C.J.) and Prajwal S Reddy(P.S.R.).

P.S.R. contributed to Chapter 1 and Chapter 2 except for Section 2.2.1-2.2.4 and Section 2.4.1. The rest were explained by C.J..

C.J. proposed an acoustic metamaterial design method described in Section 4.1 and P.S.R. described a CFD-acoustic simulation method in Section 4.2.1 and Section 4.3.

C.J. then analysed the sound source and its environment in Chapter 3 C.J. presented the design and a simulation with exhaust pipe results of the space-coiling cell in Section 5.1-5.3.

P.S.R. presented under-cab simulation results and analysis in Section 5.4-5.6.

The conclusions were described by both P.S.R. and C.J..

List of Acronyms

Below is the list of acronyms that have been used throughout this thesis listed in alphabetical order:

AMM	Acoustic Metamaterial
BEM	Boundary Element Method
BPF	Blade Passage Frequency
CFD	Computational Fluid Dynamics
CHT	Conjugate Heat Transfer
DD	Domain Decomposition
DLMPP	Double-Layer Micro-Perforated Panel
DNS	Direct Numerical Simulation
EEC	Equivalent Electrical Circuit
FEA	Finite Element Analysis
FEM	Finite Element Method
GMRES	Generalized Minimal Residual
IDDES	Improved Detached Eddy Simulation
LES	Large Eddy Simulation
LNSE	Linearized Navier-Stokes Equation
MPP	Micro-Perforated Panel
MRF	Moving Reference Frame
MUMPS	Multifrontal Massively Parallel Sparse Direct Solver
PARADISO	Parallel Direct Solver
PML	Perfectly Matched Layer
PSO	Particle Swarm Optimization
RANS	Reynolds Averaged Navier-Stokes
RPM	Resolution of Fan per Minute
RPS	Rotational Speed per Second
SPL	Sound Pressure Level
SST	Shear Stress Transport
TAP	Total Acoustic Pressure
TMM	Transfer Matrix Method

Contents

List of Figures

List of Tables

1

Introduction

The growing need for enhanced cooling solutions in the automotive industry, particularly with the advent of new propulsion systems, has led to increased demand for fan performance. Consequently, the noise levels produced by high-speed fans have risen, causing disturbances to both vehicle users and the surrounding environment. Direct noise control at the source is complex, as it often affects the performance of cooling components, making it difficult to achieve an optimal balance. However, passive noise control techniques offer a viable alternative. These methods intervene along the path between the noise source and the receiver but cannot rely on traditional noise barriers, which may obstruct airflow. To address this challenge, metamaterials present a promising solution. Composed of individually engineered units, metamaterials can be tailored to meet specific requirements, with the combination of these units forming the complete component.

1.1 Literature Review

1.1.1 Truck Cooling Fan

Providing efficient cooling systems is an important part of the thermal management of heavy-duty equipment such as trucks which must function under severe operation conditions. For this purpose, the region of operating conditions for the cooling fan and for the under-hood airflow systems must be appropriately designed to ensure satisfactory aerodynamic and thermodynamic efficiency. There have been studies undertaken in many studies which focus on the dynamics of cooling airflow with the aim of increasing the degree of cooling offered while reducing the amount of cooling airflow drag and noise. This subsection consists of the most pertinent material relating to the truck cooling fan design with a multifaceted thermodynamics-aerodynamics- and airflow approach.

- **Cooling Airflow in Heavy Trucks – Impact of Fan and Shroud Design:** Hallqvist's (2008) [12] research on the back-up of cooling airflow in heavy trucks is significant as it exposes factors that determine the cooling efficiency. The study looks into such aspects, as the fan shrouds and the fan geometry, and assesses their effect on the general airflow distribution. The findings of the research are such that the depth and the configuration of the fan shrouds influence the cooling effectiveness by even dispersing the airflow over the heat

exchangers, reducing the losses in pressures encountered and increasing the rate of cooling.

In particular, Hallqvist cites an instance where fan shrouds that are not designed properly can cause the cooling system flow to become irrotational leading to flow recirculation or radiative maldistribution which is not acceptable for an efficient cooling system. This study illustrates the importance of sufficient optimization of fan attachment structures to the radiators in relation to cooling performance and aerodynamics.

- **CFD Simulation of Under-Hood Aero-Thermal Flow:** Zhang et al. (2017) [41] set out to extend the view of the under-hood aerothermal flow dynamics by utilizing 3D Computational Fluid Dynamics (CFD). The study investigates the coupled systems that exist in the engine compartment, including the radiator, cooling fans, and other heat exchangers. As the conditions of vehicle speed and thermal load were varied, the components that transferred heat through conduction, convection, and radiation were observed.

  One of the significant contributions of the work done at Zhang's includes the use of a moving reference frame (MRF) for fan rotation modeling. The importance of the cooling fan effect on the airflow was thus modeled more accurately. According to Zhang and colleagues, effective airflow patterns, the modification of which the heat system operates, Zhou observed that indeed the rotation of a fan in conjunction with wheel effects had an apparent influence on airflow systems in an under-hood aerodynamics system. It was reported that there are designs of fans that can lead to considerable improvements in the operational efficiency of a cooling system without a rise in fuel use and meeting the emission limits.
- **Noise and vibration analysis for automotive radiator cooling fan:** Razak et al. (2020) [28] focus on the noise and vibration characteristics of automotive radiator cooling fans, a critical component in vehicle thermal management systems. The study addresses how the operational noise and vibrations of cooling fans impact vehicle NVH (Noise, Vibration, and Harshness) levels, which are essential for both performance and passenger comfort. By analyzing these characteristics, the researchers aim to understand the primary contributors to fan-generated noise and vibration, including aerodynamic factors, fan blade design, and operational speed.

  The study uses experimental methods to assess how modifications in fan geometry, materials, and mounting configurations affect noise levels and vibration behavior. These findings contribute valuable insights to the field, supporting the design of quieter and more efficient cooling systems in automotive applications.
- **Early-Stage Simulation Approaches for Truck Cooling Systems:** Pan et al. (2010) [26] describes a hybrid simulation strategy in regard to the truck cooling system design in its early development phases. The authors employ a 1D and a 3D simulation – a system of simulation containing a 1D model for straightforward efficiency and a 3D CFD model for detailed analysis. This hybrid approach provides an integrated approach to analyse airflow and thermal characteristics of the cooling system in the truck considering the cooling

system parameters such as flow rate, heat load and pressure of the system. In the beginning phases of design, 1D models are useful in that they are relatively fast at providing system-level insight on the cooling circuit. However, these models may lack some details in regions of the high complexity of airflow and heat transfer. So the study makes up for this shortcoming by employing 3D CFD in the important regions and is able to provide detailed simulation of heat transfer and airflow around particular components. The hybrid method is shown to be valid by experimental results, proving its ability to give reasonable estimates of thermal performance across different designs. This method provides participation for early parametric analysis allowing engineers to quickly and cost-effectively try many configurations. The early identification of the optimal cooling design is beneficial in reducing physical prototyping costs and guarantees the designs will be able to meet the emission and performance specifications. In addition, the combination of 1D and 3D in these tools enables the designer to use a global as well as a localized perspective which is very important in designing intricate truck cooling systems.

- **Thermal Management with CFD Tools in Commercial Vehicles:** Ayyar et al. (2017) [2] investigate Computational Fluid Dynamics (CFD) for analysis and optimization of vehicle cooling systems, in particular the front-end cooling module. The CFD tool Fluent is applied for predicting airflow and temperature distribution around external cooling parts of the vehicle, as well as recognizing possible problems such as whether hot air is being re-circulated in a way that could damage the thermal efficiency. The results show in particular how FEA serves to improve the efficiency of front-end cooling modules which are essential in preserving the thermal balance of the engine in a commercial vehicle. To some extent, CFD is able to assist in building regulations related to the control of emissions and fuel economy, which are gaining importance within the industry by solving cooling efficiency and recirculation problems. The authors perform tests on physical prototypes of the designed systems and compare the results of fusion-simulation modeling with the corresponding test results. This two-way process of performing computer modeling followed by experiments is said to be the best approach in the industry. The results showed a strong correlation between simulated and experimental data, similar studies have reported a high correlation of over 90% between CFD and prototype testing results. Although CFD is a potent tool, the research recognizes that there will be limitations owing to the differences that may be experienced in real-world conditions which would influence the accuracy of the simulations. The authors propose that further work might include some actual testing in other environmental scenarios in order to enhance even more the predictive capability of the model.

1.1.2 Numerical Study

- **Large Eddy Simulation (LES) for Noise Reduction:** The study conducted by Mo and Choi (2020) [22] investigated the feasibility of using Large Eddy Simulation (LES) as a technique for modelling unsteady cooling fan

airflow aiming at turbulence and eddy induced aerodynamic noise. Since aerodynamics involves turbulent flow, airflow structures of higher turbulence can easily be captured using this method in comparison to this structural method. Their experiments showed that tonal noise—one of the main components of the total noise radiated by the fan—was generated near the blade radius region's leading edge because of augmented radial flow. Applying perturbed LES together with the Ffowcs-Williams-Hawkings (FW-H) acoustic analogy, they managed to suggest modifications of the shape of the fan blades to effectively bring the noise level down by as much as 5 dB with no adverse effects on the efficiency of airflow by changing the pitch and spacing of blades.

This research clearly demonstrates the importance of applying LES for improving the noise effectiveness of the fan design without sacrificing its cooling efficiency. The downside of the RANS approaches is that most available turbulence closures are relatively ineffective in capturing time-dependent transitional phenomena, such as vortex shedding, etc. which, however, are key elements in noise generation capabilities.

- **CFD for Airflow Optimization:** Srinivasa et al. (2014) conducted a comprehensive study using CFD simulations to optimize the performance of truck cooling fans by adjusting key design parameters, such as the fan immersion ratio and shroud geometry. By simulating the airflow patterns across different fan configurations, the researchers were able to assess how changes in fan-to-core distance and shroud chamfer length affected the distribution of airflow over the radiator. Their findings revealed that a well-optimized fan-shroud configuration can significantly reduce aerodynamic drag while ensuring more uniform airflow through the radiator core, leading to improved cooling efficiency and fuel savings.

  CFD is particularly useful for studying recirculation zones and pressure losses, both of which can reduce the effectiveness of the cooling system if not properly managed. The study demonstrated that optimizing airflow distribution can minimize such inefficiencies, which is crucial for maintaining engine temperatures under various operational conditions [34].

- **Conjugate Heat Transfer (CHT) and Finite Element Analysis (FEA) for Thermal Stress and Durability:** Thermal stress and mechanical fatigue are critical considerations in the design of cooling fans, particularly when they operate under high-speed conditions. Wang and Jiang (2017) [38] employed Conjugate Heat Transfer (CHT) modeling, which integrates CFD with Finite Element Analysis (FEA), to assess both the thermal behavior and the mechanical durability of truck cooling fans. CHT simulations are essential for understanding how heat transfer occurs within the cooling system, especially in high-load scenarios where the engine generates significant heat that must be dissipated efficiently.

  By coupling FEA with CFD, Wang and Jiang were able to predict areas of stress concentration in the fan blades that could lead to failure over time. The study also showed that blade thickness and material selection are critical in reducing thermal and mechanical fatigue, ensuring the fan's long-term performance. These findings highlight the importance of integrating thermal and

structural simulations when designing cooling systems, as they allow engineers to predict both cooling performance and structural integrity under various operating conditions.

- **Aeroacoustic Analysis and Blade Optimization:** Xu et al. (2024) [13] have concentrated on the cooling fan aeroacoustics, using FEM noise predictions. This type of research showed that fan blades and the air movement create special noise which spreads over a broad range, particularly, close to the tips of the blades where the airflow becomes chaotic. In this regard, by modeling both the near field acoustic pressure as well as the far field noise propagation, Xu et al. suggested constructive changes in the fan that would enable operating at lower noise levels without prejudice to the cooling ability of the fan.
  In particular, the research showed that variations of the trailing edge shape of fan blades can reduce the vorticity that causes the noise. Implementing BEM greatly improved the estimation of the amount of noise generated inside the fan directly caused by the pressure fluctuations, which will assist the design of noise-compliant cooling devices that do not compromise on performance.
- **Improved Delayed Detached Eddy Simulation (IDDES) for Transient Flow Modeling:** According to Lakzayi et al. (2024) [18], Improved Delayed Detached Eddy Simulation (IDDES) was used to investigate the unsteady flow phenomena around automotive cooling fans. IDDES is a hybrid modeling technique, which uses RANS to model parallel flows and includes LES as a means of modeling separated flows and turbulent eddies. Evaluation of this method demonstrated its suitability in modeling unsteady internal fluid movements that happen around rotating fan blades which is often impossible by only modeling the fan using a steady state approach.
  This study has also stressed that there are significant advantages in predicting aerodynamic noise when transient flow simulations using IDDES are conducted rather than steady-state methods are employed. This enables Lakzayi and co-workers to determine those regions where shedding of vortices and separation of flows occurs thereby improving fan design techniques that achieve quieter operation without compromising air movement. It was shown that the advanced turbulence models like IDDES, offer additional factors improving cooling fan operations by capturing moving parts in normal operation.

1.2 Motivation

The problem this study wants to address is the increasing noise pollution from cooling fans in heavy-duty trucks, a situation that is made worse by the need for large cooling fans because of increased cooling needs. The same cooling fans are used in trucks to provide auxiliary power and this invariably leads to poor thermal unit support. However, industries have seldom faced it as a hurdle either arguably due to regulation issues or pragmatic interface considerations because mechanical noise from cooling fans particularly when operated at elevated speeds in the applications is arguably excessive [40].
These noises are tonal noise and broadband noise due to the operation of the fan in

the truck's body. Tonal noise is specifically picked up at the blade passage frequency which occurs when fan blades rotate in the air, while broadband noise is produced by turbulence due to wind that blows on the fan blades. As fan diameter is increased, so is the blade tip speed hence many of these noise components are compounded. It's catcher 22, where larger fans give the required cooling airflow but are also unacceptably noisy.

This concern is of utmost importance in heavy-duty trucks for a number of reasons. Most of all, there are laws that do not allow vehicle noise emission above certain levels and more such laws are likely to emerge which makes it necessary for manufacturers to reduce noise outside the vehicle. It remains very difficult to engineer systems that will be compliant with these regulations and still achieve efficient cooling. Another one is the driver's ergonomics have on immersion inside the cultivator's cabin because fumes and cabin noise, which build after some time, promote fatigue and inattentiveness and create a distressful scenario to work in. High volumetric noise level perhaps for long periods of time is not only a comfort factor but a serious safety concern as well.

The use of standard approaches with classic means of reducing noise such as sound-absorbing materials or minor changes to the fan design has proved ineffective when dealing with this issue, especially for reducing noise without compromising on the cooling. This standard technology is being replaced by the more advanced one—in particular—by Acoustic Metamaterials (AMMs) as they seem to present more solutions. They are materials made with waves in mind that have been constructed such that they are able to act on sound in a manner that ordinary materials would fail. They make it possible to focus noise such as that produced by the BPF while the necessary air for cooling remains in place.

The sound propagation control capability of AMMs, which does not interfere with air exchange, presents a viable remedial approach to the load noise problem of cooling fans. When using AMMs, the designer can use them in some of the fan or fan surround designs so as to target some of the aerodynamic noise that may be produced by the fan and therefore increase the number of quiet trucks that will be able to meet the regulations and still have the engine well cooled.

This thesis, in particular, proposes the use of acoustic metamaterials for suppressing aerodynamic noise in heavy-duty trucks with cooling fans housed in the engine enclosure. In other words, this study aims at developing appropriate designs of AMMs and embedding them into the fan system to suppress noise at designed levels. The specific objectives are as follows:

- First, investigate the noise generated by cooling fans: The first step in the current research involves consideration of the noise of the cooling fans used in heavy-duty trucks. This will include evaluating the tonal and broadband noise due to fan measurements and the frequency spectrum of such noise. The objective here will be to locate the frequency areas that are most responsible for the overall subjective rating of the noise and the mechanisms that generate these noise sources such as vortex shedding and turbulence.
- Unit for creating and developing the Acoustic Metamaterials: In the present case the task is focused on designing acoustic metamaterials having applica-

tion in high-efficiency cooling fan systems for reducing noise. In this regard, AMMs will be developed by targeting the specific noise frequencies that were determined in the previous objective. Resonators, membrane metamaterials, and bulk Metamaterials that do not obstruct the path of air but can suppress sound. The design also aims if the AMMs will be used in real-life applications that will be in the cooling system of the truck.

- Simulation and Optimization of Acoustic Metamaterials: Once the first drawings are made, the components will be subjected to Computational Fluid Dynamics (CFD) and Finite Element Analysis (FEA) simulations hoping to ascertain their noise reduction performance empirically tested. They will also predict the acoustic metamaterials in motion and how they will be used in changing the propagation of noise and carrying air to ensure that no excess disturbances arise that would lead to potential aerodynamic drag to cooling systems. The aim is to increase the performance of AMM so that the performance of noise reduction is maximized without compromising the cooling performance.
- Prototyping and Experimental Validation: Following the end of the simulation, it will be as well developed the parameters of the prototype test developed AMM that was especially highly effective in a virtual environment. In this case, AMM prototypes will be installed in realistic tram operation conditions, with the possibility to measure both heat exchange effectiveness and noise suppression. The studies would help to understand how AMM designs perform and how feasible they are in practice in terms of noise and heat rather than just heat or noise.
- Trade-off Analysis and Final Optimization: The thesis work establishes one more objective – it is to avoid negative interference coming from implementing the noise-reducing factors into the cooling system. This objective focuses on carefully analyzing the relations between the two variables: noise reduction and the ability of the device to cool and determining their optimal compromise. This will entail the Arctic Mouthpiece Manikin that further increases and at the same time modifies, the design based on empirical data, as well as Realistic Artistic Surgery further models to help fine-tune the AMM forms.

2

Theory

There are two divisions in this section. The first covers the pertinent fluid mechanics modelling and the second talks about acoustics. It is essential to understand the physics that governs both fluids and acoustics internally to be able to comprehend the relation between them. One has also mentioned some theories on the solvers used in this study after discussing the acoustic theory involved.

2.1 Computational Fluid Dynamics

The Navier-Stokes equations, which are composed of the *momentum equations*, the *energy equation*, and the *continuity equation*, regulate all aspects of fluid dynamics. These equations when combined explain the physics of fluid flow, deformation, compression, and energy transfer. Nevertheless, the energy equation can be disregarded for this project because the fluid's temperature dependency is minimal. This leaves an equation system made up of three momentum equations for the x, y, and z directions and one continuity equation.
The conservation of mass is thereafter governed by the continuity equation, which takes the form

$$\frac{\partial \rho}{\partial t} + \operatorname{div}(\rho \boldsymbol{u}) = 0, \tag{2.1}$$

where $\boldsymbol{u}$ is the velocity vector and ρ indicates the fluid's density. The momentum equations, which have the following form, then control the conservation of momentum.

$$\begin{cases} \frac{\partial(\rho u)}{\partial t} + \operatorname{div}(\rho u \boldsymbol{u}) &= -\frac{\partial P}{\partial x} + \operatorname{div}\Big(\mu \operatorname{grad}(u)\Big) \\ \frac{\partial(\rho v)}{\partial t} + \operatorname{div}(\rho v \boldsymbol{u}) &= -\frac{\partial P}{\partial y} + \operatorname{div}\Big(\mu \operatorname{grad}(v)\Big) \\ \frac{\partial(\rho w)}{\partial t} + \operatorname{div}(\rho w \boldsymbol{u}) &= -\frac{\partial P}{\partial z} + \operatorname{div}\Big(\mu \operatorname{grad}(w)\Big), \end{cases} \tag{2.2}$$

Where μ represents the dynamic viscosity and P denotes the pressure field within the fluid domain. Typically, both the density and dynamic viscosity exhibit significant dependence on pressure. Additionally, the pressure field and its gradient remain undetermined [36].
Thus, it can be deduced that the system of equations encompasses four variables: the pressure field P and the velocities u, v, and w. While the system is theoretically solvable, practical resolution has been challenging, with no analytical solutions found to date. As such, an appropriate discretisation scheme must be adopted to address the problem numerically using the finite volume method [36]. Additionally,

the inclusion of a turbulence model is essential for accurately simulating turbulent phenomena [7].

2.1.1 Turbulence Modeling

Solving the Navier-Stokes equations (2.1) and (2.2) directly using the finite volume method is possible and is referred to as *Direct Numerical Simulations* (DNS). Nevertheless, for turbulent flows, this method requires substantial computational resources. Therefore, it is common to use *Reynolds decomposition* and implement a turbulence model to lessen the computational burden.

2.1.1.1 RANS Equations

Begin with Reynolds decomposition to initiate the selection of a turbulence model. Reynolds decomposition separates mean and fluctuating components of velocity and pressure, specifically,

$$\begin{cases} \boldsymbol{u} = \bar{\boldsymbol{u}} + \boldsymbol{u}', \\ P = \bar{P} + P', \end{cases} \tag{2.3}$$

where $\bar{\boldsymbol{u}}$ is the time-averaged velocity, $\boldsymbol{u}'$ is the velocity fluctuation, $\bar{P}$ is the time-averaged pressure field, and P' is the pressure fluctuation. Inserting (2.3) into the Navier-Stokes equations (2.1) and (2.2), and subsequently time-averaging, yields the *Reynolds-Averaged Navier-Stokes* (RANS) equations. The RANS continuity and momentum equations respectively are often written in Einstein notation as

$$\begin{cases} \dfrac{\partial \bar{u}_i}{\partial x_i} = 0, & \text{(2.4a)} \\ \dfrac{\partial(\rho \bar{u}_I)}{\partial t} + \dfrac{\partial}{\partial x_j}\Big(\rho \bar{u}_I \bar{u}_j\Big) = -\dfrac{\partial \bar{P}}{\partial x_j} + \mu \dfrac{\partial^2 \bar{u}_I}{\partial x_j \partial x_j} - \dfrac{\partial}{\partial x_j}\Big(\rho \overline{u'_I u'_j}\Big), & \text{(2.4b)} \end{cases}$$

where the uppercase index I represents the directions x, y, or z, and the lowercase indices i and j indicate summation over the x, y, and z directions. Additionally, the assumptions in (2.4a) and (2.4b) are that the fluid is Newtonian and the flow is incompressible, meaning that ρ and μ are constants [7]. It is fair to assume constant density and viscosity for compressible fluids, like air, when the Mach number $M < 0.3$ [6].

Nevertheless, the closure problem is introduced by breaking down the velocity and obtaining the RANS equations. The terms $\rho\overline{u'_I u'_J}$ are unknown and are referred to as the *Reynolds stresses*. Thus, there are just four equations, (2.4a) and (2.4b), but ten unknowns, $\bar{u}_I$, $\bar{P}$, and $\rho\overline{u'_I u'_J}$. To conclude the equation system, the Reynolds stresses must therefore either be represented as functions or six new equations must be added. A *turbulence model* is the term used to describe a closure technique for the equation system in this study.

2.1.1.2 SST $k-\omega$ Model

The *Shear Stress Transport* (SST) $k-\omega$ model is a popular turbulence model that combines elements of the $k-\varepsilon$ and ordinary $k-\omega$ turbulence models. The $k-\varepsilon$ and ordinary $k-\omega$ models have one thing in common: they both use the assumption that the turbulence is *isotropic*. This implies, by definition, that

1. $\rho\overline{(u_I')^2} = \rho\overline{(u_J')^2}$, and
2. that $\rho\overline{u_I'u_J'} = 0$, $I \neq J$, due to the lack of correlation between changes in two distinct directions.

Therefore, to address the closure problem, just two new equations need to be introduced [7]. Therefore, the equations are introduced by the SST $k-\omega$ turbulence model.

$$\begin{cases} \dfrac{\partial k}{\partial t} + \dfrac{\partial}{\partial x_j}\left(\bar{u}_j k\right) = \dfrac{\partial}{\partial x_j}\left(\left(\nu + \dfrac{\nu_t}{\sigma_k}\right)\dfrac{\partial k}{\partial x_j}\right) + P^k - \beta^* k\omega & \text{(2.5a)} \\ \dfrac{\partial \omega}{\partial t} + \dfrac{\partial}{\partial x_j}\left(\bar{u}_j \omega\right) = \dfrac{\partial}{\partial x_j}\left(\left(\nu + \dfrac{\nu_t}{\sigma_\omega}\right)\dfrac{\partial \omega}{\partial x_j}\right) + \alpha\dfrac{P^k}{\nu_t} - \beta\omega^2 + 2(1-F_1)\sigma_{\omega_2}\dfrac{1}{\omega}\dfrac{\partial k}{x_i}\dfrac{\partial \omega}{\partial x_i}, & \text{(2.5b)} \end{cases}$$

In this case, $k = 0.5\left(\overline{(u')^2} + \overline{(v')^2} + \overline{(w')^2}\right)$. The turbulence kinetic energy is denoted by k, the turbulence kinetic energy production term is P^k, and the *specific* rate of dissipation of the turbulence kinetic energy k into internal thermal energy is ω. Typically, when modeling turbulence, P^k is represented as

$$P^k = -\overline{u_i'u_j'}\frac{\partial \bar{u}_i}{\partial x_j}. \tag{2.6}$$

However, it is typical practice in the SST $k-\omega$ model to attempt to limit P^k by a value akin to

$$P^k := \min\left(-\overline{u_i'u_j'}\frac{\partial \bar{u}_i}{\partial x_j},\, 10\beta^* k\omega\right). \tag{2.7}$$

Moreover, the fluid's kinematic viscosity is $\nu = \mu/\rho$, while the turbulence eddy viscosity is represented by ν_t.

$$\nu_t := \frac{a_1 k}{\max(a_1\omega, |\bar{s}|F_2)}. \tag{2.8}$$

In this case, $|\bar{s}| := \sqrt{2\bar{s}_{ij}\bar{s}_{ij}}$ is the tensor's mean strain rate magnitude.

$$\bar{s}_{ij} := \frac{1}{2}\left(\frac{\partial \bar{u}_i}{\partial x_j} + \frac{\partial \bar{u}_j}{\partial x_i}\right), \tag{2.9}$$

Also, the function F_2 is given as

$$F_2 := \tanh\left(\eta^2\right), \quad \eta := \max\left(\frac{2\sqrt{k}}{\beta^*\omega d},\, \frac{500\nu}{d^2\omega}\right), \tag{2.10}$$

where d is the wall node's distance from the nearest one. In a similar manner, F_1 is defined as

$$F_1 := \tanh\left(\xi^4\right), \quad \xi := \min\left(\frac{4\sigma_{\omega_{k-\varepsilon}} k}{CD_\omega d^2} \max\left(\frac{\sqrt{k}}{\beta^* \omega d}, \frac{500\nu}{d^2\omega}\right)\right), \tag{2.11}$$
$$CD_\omega := \max\left(2\sigma_{\omega_{k-\varepsilon}} \frac{1}{\omega} \frac{\partial k}{\partial x_i} \frac{\partial \omega}{\partial x_i}, 10^{-10}\right).$$

Additionally, F_1 is utilized to define α and β as

$$\begin{cases} \alpha := F_1 \alpha_{k-\omega} + (1 - F_1)\alpha_{k-\varepsilon} & \text{(2.12a)} \\ \beta := F_1 \beta_{k-\omega} + (1 - F_1)\beta_{k-\varepsilon}. & \text{(2.12b)} \end{cases}$$

Lastly, β^*, σ_k, and σ_ω are the empirical constants along with, $\alpha_{k-\omega}$, $\alpha_{k-\varepsilon}$, $\beta_{k-\omega}$, $\beta_{k-\varepsilon}$, σ_{ω_2}, a_1, and $\sigma_{\omega_{k-\varepsilon}}$ [7]. Keep in mind that the functions and constant values may change based on the CFD code being used and the problem being solved. Nonetheless, when utilizing the SST $k-\omega$ model, one frequently works with functions akin to those previously mentioned. In particular, the F_1 and F_2 work as switch functions, allowing the deployment of several models in particular fluid regions where each model performs well. Their range is from 0 to 1.
The primary function of the F_1 function is to transition between modified versions of the normal $k - \omega$ turbulence model and the $k - \varepsilon$ version. In general, the $k - \varepsilon$ model performs well in the bulk flow and outer boundary layer, but it overpredicts the shear stress in locations with unfavourable pressure gradients and struggles to capture the near wall effects. In addition, the typical $k - \omega$ model has the drawback of being reliant on the bulk flow value of ω, despite being able to simulate adverse pressure gradient zones more accurately. As a result, in the bulk flow and outer boundary layer area, where $F_1 \approx 0$, (2.5a) and (2.5b) behave more like the $k - \varepsilon$ model. Furthermore, (2.5a) and (2.5b) function more like the $k - \omega$ model [7] in the inner boundary layer area, where $F_1 \approx 1$.
However, the usual $k - \omega$ turbulence model is insufficient to prevent over-predictions in the adverse pressure gradient regions. For this reason, the turbulent eddy viscosity ν_t in (2.8) is modeled. Thus, in (2.8), the F_2 function and the max-function cooperate to restrict the shear stress. In conclusion, models that more accurately represent the physics of the boundary layer region are used when $F_2 \approx 1$, and models that more accurately represent the physics of bulk flow are used when $F_2 \approx 0$ [7].

2.2 Acoustics

2.2.1 Helmholtz Resonator

Helmholtz resonance, also known as wind throb is an effect named after the German physicist Hermann von Helmholtz. It relates to the air resonance phenomena that occur within a cavity. The neck constriction continues to serve as the acoustic mass component, and the enclosed air volume within the resonator acts like a spring, providing acoustic compliance. When air is driven into and out of a cavity, the air

inside vibrates at a particular natural frequency, resulting in this kind of resonance. Thus, this system is also called the "mass-spring" system.
Both the mass and compliance are derived from the acoustic components of the Helmholtz resonator. One of the simplest examples of a Helmholtz resonator is an open bottle shown in Figure 2.1[16]. The neck of the bottle acts as the acoustic mass as the blue area suggests, while the enclosed airspace functions as the acoustic stiffness. The resonance frequency f_0 is determined by:

$$f_0 = \frac{1}{2\pi}\sqrt{\frac{K}{M}} \tag{2.13}$$

With stiffness, also the reverse of compliance, $K = \frac{\rho c^2 S^2}{V}$ and mass $M = \rho l_{eff} S$. Where c is the speed of sound, S is the neck area and V is the volume of the cavity. Because the air at the open ends of the neck also vibrates, contributing to the mass effect. The effective length l_{eff} equals the length of the neck l_n plus the end correct of the neck[16].

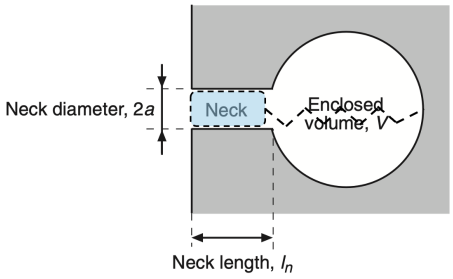

Figure 2.1: Schema of a Helmholtz resonantor

2.2.2 Micro-Perforated Panel (MPP)

One of the most well-known models, the micro-perforated panel (MPP) based on the Helmholtz resonator, is discussed in this study. The holes on the panel together form an acoustic mass, and the cavities that follow the panel form an acoustic compliance. According to Maa[21], the type of double layer can absorb sound in a broad band, due to the absorption in both layers.
The perforated panel model for the Helmholtz resonator is defined with the equivalent mass M, the resistance r from viscosity, and the equivalent compliance C as follows[21] [37].

$$M = \frac{t}{pc}\left(1 + \frac{1}{\sqrt{9 + \frac{x^2}{2}}} + 0.85\left(\frac{d}{t}\right)\right), \tag{2.14}$$

$$r = \frac{32ut}{pcd^2}\left(\sqrt{1 + \frac{x^2}{32}} + \frac{xt\sqrt{2}}{8d}\right), \tag{2.15}$$

$$C = -\cot\frac{D}{c} \tag{2.16}$$

Where t is defined as the thickness of the panel, p is defined as the open area percentage, c is the speed of sound, μ is the viscosity of air, D is the depth of the cavity, d is the diameter of the holes, and ω is the angular frequency of the sound wave. x is a frequency constant with $x = \frac{d}{2}\sqrt{\omega/\mu}$ and f is sound frequency.

2.2.3 Space-Coiling Structure

Another way to absorb sound while improving airflow permeability is to apply a binaural structure. A labyrinth-based space combined with a ventilation channel has been widely studied. A Fano-like phenomenon can be observed with this kind of structure due to the interference of two wave incidents from two paths. Fano resonance most times refers to the interference of a local resonance and a background continuum. It is first observed by Uno Fano in the optics field. In such a way, the acoustic wave can be trapped or absorbed in the coiling space and also cancelled by the interference. In this section, the acoustic properties of the subchannels in such a space-coiling structure are discussed. The calculation of the interference between such structure and the ventilation is introduced in Chapter 5.
The propagation characteristics of the sound of such a structure can thus follow the propagation of the plane wave in a tube. Modified after Krichhoff, Zwikker and Kosten's approach, Michael developed a way to calculate the complex density, compressibility function, propagation constants, and characteristic impedance. Given the structure has several channels and each of them might have different geometries, methods introduced later will provide a way to combine channels.

For a rectangular tube, the complex density ρ and complex bulk modulus K follow:

$$\rho_f(\omega) = \rho_0 \frac{(a/2)^2(b/2)^2}{4G_\rho^2(\omega)\sum_{m\in\mathbb{N}}\sum_{n\in\mathbb{N}}[\alpha_m^2\beta_n^2(\alpha_m^2 + \beta_n^2 + G_\rho^2(\omega))]^{-1}} \tag{2.17}$$

$$K_f(\omega) = K_0 \frac{1}{\gamma - \frac{4(\gamma-1)G_k^2(\omega)}{(a/2)^2(b/2)^2})\sum_{m\in\mathbb{N}}\sum_{n\in\mathbb{N}}[\alpha_m^2\beta_n^2(\alpha_m^2 + \beta_n^2 + G_K^2(\omega))]^{-1}} \tag{2.18}$$

With,

$$G_\rho = \sqrt{\frac{1j\cdot\omega\cdot\rho_0}{\eta}} \tag{2.19}$$

$$G_K = \sqrt{\frac{1j\cdot\omega\cdot\mathrm{Pr}\cdot\rho_0}{\eta}} \tag{2.20}$$

Where a and b are the dimensions of the rectangular duct, $\alpha = (2m + 1)\pi$ and $\beta = (2n+1)\pi$, the viscosity of the air $\eta = 1.8134\times10^{-5}$, air pressure $P_0 = 1.013\times10^5$, specific heat at constant volume $C_v = 0.712$ kJ/(kg.K), ratio of specific heat $\gamma = 1.4$, $C_p = C_v \cdot \gamma$, thermal conductivity $k_{\text{heat}} = 0.026$, density of the air $\rho_0 = 1.21$ kg/m^3, adiabatic bulk modulus $K_0 = \gamma \cdot P_0$, $\omega = 2\pi f$, speed of sound $c_0 = 343$ m/s, $k_0 = \frac{2\pi f}{c_0}$, Prandtl number is $\text{Pr} = \frac{C_p \cdot \eta}{k_{\text{heat}}}$.

Acoustic impedance Z and equivalent wave number k of each channel can thus be calculated as follows:

$$Z = \frac{\sqrt{K_f \cdot \rho_f}}{a \cdot b} \tag{2.21}$$

$$k = \frac{\omega}{\sqrt{K_f/\rho_f}} \tag{2.22}$$

2.2.4 Absorption Coefficient

The acoustic sound absorption coefficient α is a measure of a material's ability to absorb sound energy, rather than reflecting it. It is a dimensionless value normally ranging from 0 to 1, where 0 indicates perfect reflection (no absorption), and 1 indicates perfect absorption (all sound energy is absorbed). In the case of Fano-like interference, a negative absorption coefficient can also be observed. It is mathematically defined as the ratio of absorbed sound energy ($E_{absorbed}$) to the incident sound energy ($E_{incident}$):

$$\alpha = \frac{E_{absorbed}}{E_{incident}} = 1 - |R|^2 \tag{2.23}$$

The reflection coefficient (R) quantifies how much sound pressure is reflected and is related to the acoustic impedances of the two media at the boundary (e.g., air and the material). The reflection coefficient (R) relates to the difference in acoustic impedances (Z_1 for material 1 and Z_2 for the material 2) as follows:

$$R = \frac{Z_2 - Z_1}{Z_2 + Z_1} \tag{2.24}$$

2.2.5 Linearized Navier-Stokes Equation In Frequency Domain

In this section, the LNSE for modelling the flow-acoustic interaction is described. The LNSE presented here is used to predict the acoustic scattering in the computational domain, as described in Section 4.2, due to the presence of flow. Re-writing the Navier-Stokes mentioned in Section 2.1 in tensor notation:

The continuity equation:

$$\frac{\mathrm{D}\rho}{\mathrm{D}t} + \rho\frac{\partial u_i}{\partial x_i} = 0\,, \tag{2.25}$$

where the material derivative is $\mathrm{D}/\mathrm{D}t$, the density is ρ, and the three components of the velocity $\boldsymbol{u}$ are u_i ($i = 1,2,3$).

The momentum equation:

$$\rho\frac{\mathrm{D}u_i}{\mathrm{D}t} = -\frac{\partial p}{\partial x_i} + \frac{\partial \tau_{ij}}{\partial x_j} + \rho f_i \,, \tag{2.26}$$

where f_i is the volume force acting in the i^{th} direction, p is the pressure, and μ is the dynamic viscosity. The definition of the viscous stress tensor is

$$\tau_{ij} = \mu\left(\frac{\partial u_i}{\partial x_j} + \frac{\partial u_j}{\partial x_i} - \frac{2}{3}\frac{\partial u_k}{\partial x_k}\delta_{ij}\right) , \tag{2.27}$$

where the Kronecker delta function is denoted by δ_{ij}.

The energy equation:

$$\rho\frac{\mathrm{D}}{\mathrm{D}t}\left(e + \frac{u_i u_i}{2}\right) = \rho\dot{q} + \frac{\partial}{\partial x_i}\left(\kappa_{th}\frac{\partial T}{\partial x_i}\right) - \frac{\partial (p u_i)}{\partial x_i} + \frac{\partial (u_i \tau_{ij})}{\partial x_j} + \rho f_i u_i \,, \tag{2.28}$$

where $\dot{q}$ is the rate of volumetric heat addition per unit mass, e is the internal energy, T is the temperature, and κ_{th} is the thermal conductivity. Depending on which variables are of primary relevance, the energy equation shown in 2.28 can be stated in terms of enthalpy h, entropy s, temperature T, or pressure p. Nonetheless, the energy equation is typically expressed as follows in terms of temperature T:

$$c_p\rho\frac{\mathrm{D}T}{\mathrm{D}t} - \frac{\mathrm{D}p}{\mathrm{D}t} = \rho\dot{q} + \frac{\partial}{\partial x_i}\left(\kappa_{\mathrm{th}}\frac{\partial T}{\partial x_i}\right) + \phi(\mu,u_i) + \rho f_i u_i \,, \tag{2.29}$$

where the heat capacity at constant pressure is denoted by c_p. The viscous dissipation, ϕ, is defined as

$$\phi(\mu,u_i) = \mu\left[\left(\frac{\partial u_i}{\partial x_j}\frac{\partial u_i}{\partial x_j} + \frac{\partial u_j}{\partial x_i}\frac{\partial u_i}{\partial x_j}\right) - \frac{2}{3}\left(\frac{\partial u_i}{\partial x_i}\right)^2\right] , \tag{2.30}$$

In this study, one primarily treats the fluid as a perfect gas, that is, one addresses the equation of state, viz.

$$p = \rho R T \,. \tag{2.31}$$

where R is the specific gas constant.

The governing equations for a perfect ideal gas are shown from 2.32a to 2.32c, which are derived from the governing equations previously presented. One consider the fluid to be in a state of near-equilibrium or local thermodynamic equilibrium. As a result, the term associated with the bulk viscosity, which represents the rotational and translational modes, is disregarded [27]. The ensuing presumptions are made: (1) No external source of heat is present; (2) The body force is disregarded. This results in the relationships listed below.

$$\frac{\mathrm{D}\rho}{\mathrm{D}t} = -\rho\frac{\partial u_i}{\partial x_i}\,, \tag{2.32a}$$

$$\rho\frac{\mathrm{D}u_i}{\mathrm{D}t} = -\frac{\partial p}{\partial x_i} + \frac{\partial \tau_{ij}}{\partial x_j}\,, \tag{2.32b}$$

$$c_p\rho\frac{\mathrm{D}T}{\mathrm{D}t} - \frac{\mathrm{D}p}{\mathrm{D}t} = \frac{\partial}{\partial x_i}\left(k_{\mathrm{th}}\frac{\partial T}{\partial x_i}\right) + \phi(\mu,u_i)\,. \tag{2.32c}$$

The prime variables, $\rho = \bar{\rho}+\hat{\rho}$, $\boldsymbol{u} = \bar{\boldsymbol{u}}+\hat{\boldsymbol{u}}$, $p = \bar{p}+\hat{p}$, and $T = \bar{T}+\hat{T}$, are decomposed into a mean (denoted by an over-bar $\bar{()}$) and a fluctuating part (denoted by a hat $\hat{()}$). It is possible to achieve linearization around the steady state by ignoring the high-order factors and assuming that the fluctuating quantities are modest. The perturbed quantities can then be prescribed in a harmonic form to produce the frequency-domain LNSE, for instance, $\rho'(x,t) = \hat{\rho}(x)\mathrm{e}^{\mathrm{i}\omega t}$, where ω is the angular frequency. The frequency domain presentation of the LNSE, which is obtained from the complete compressible Navier-Stokes equations, comprises the energy equation, momentum equations, and continuity equation.

$$i\omega\hat{\rho} + \frac{\partial}{\partial x_i}(\bar{\rho}\hat{u}_i + \hat{\rho}\bar{u}_i) = 0\,, \tag{2.33}$$

$$\mathrm{i}\omega\bar{\rho}\hat{u}_i + \frac{\partial(\bar{\rho}\hat{u}_i\bar{u}_j)}{\partial x_j} + (\bar{\rho}\hat{u}_j + \hat{\rho}\bar{u}_j)\frac{\partial\bar{u}_i}{\partial x_j} = -\frac{\partial\hat{p}}{\partial x_i} + \mu\frac{\partial}{\partial x_j}\left(\frac{\partial\hat{u}_i}{\partial x_j} + \frac{\partial\hat{u}_j}{\partial x_i} - \frac{2}{3}\frac{\partial\hat{u}_k}{\partial x_k}\delta_{ij}\right)\,, \tag{2.34}$$

$$\mathrm{c}_p\left(i\omega\bar{\rho}\hat{T} + \bar{\rho}\hat{u}_i\frac{\partial\bar{T}}{\partial x_i} + \bar{\rho}\bar{u}_i\frac{\partial\hat{T}}{\partial x_i} + \hat{\rho}\bar{u}_i\frac{\partial\bar{T}}{\partial x_i}\right) - \mathrm{i}\omega\hat{p} - \hat{u}_i\frac{\partial\bar{p}}{\partial x_i} - \bar{u}_i\frac{\partial\hat{p}}{\partial x_i} = \frac{\partial}{\partial x_i}\left(\kappa_{\mathrm{th}}\frac{\partial\hat{T}}{\partial x_i}\right) + \phi(\mu,\hat{u}_i)\,. \tag{2.35}$$

where $\phi(\mu,\hat{u}_i) = \hat{\tau}_{ij}\partial\bar{u}_i/\partial x_j + \bar{\tau}_{ij}\partial\hat{u}_i/\partial x_j$.

The mean flow simulations and the acoustic computations are two separate phases of the numerical work based on the LNSE in the frequency domain. Typically, compressible steady-state Reynolds-averaged Navier-Stokes (RANS) equations are used to simulate the mean flow field first. The LNSE (2.33, 2.34, and 2.35) around the steady mean flow is then solved to determine the acoustic field. Accurately predicting the system's acoustic behavior requires obtaining the mean flow field at a suitable precision. For instance, it is necessary to carefully determine the separation points and the shear layer thickness in the mean flow.
Solvers

2.2.6 Multifrontal Massively Parallel Sparse Direct Solver (MUMPS)

The massive systems of linear equations arising from the finite element discretization of the governing equations resulted in the Multifrontal Massively Parallel Sparse

Direct Solver (MUMPS) being deployed. MUMPS is a direct solver known within this domain where complex large-scale computations are concerned as being able to handle backslash operations especially effective with spine matrices. Key features:

- Sparse Matrix Handling: As opposed to general problems where the coefficient matrices may be dense, MUMPS is rather versatile in problems involving sparsity in the coefficient matrices of the system being solved. This is characteristic of the finite element techniques where even though the magnitude of the matrices created is high, they are mostly sparse due to the localized nature of the element interactions.
- Direct Kalman Filter: Simply put, MUMPS is a direct solver in the sense that an exact solution is obtained, unlike in other iterative solvers where the problem is solved in a manner that only makes a near solution to the original problem. For problems with supple matrices like in the case of stiff algorithms, MUMPS proves crucial as it addresses aspects of high stiffness.
- Parallelization: MUMPS is natural to the use of parallel computing. Indeed, it follows a multifrontal approach since the problem can be subdivided in its front into smaller parts,... which solves the task independently and can be performed in parallel on a number of processors. This dramatically saves the time needed to carry out calculations, especially when it comes to big enhanced computational modeling. MUMPS parallel functionalities were most beneficial in this work since large matrix systems were generated due to fine mesh discretization and sophisticated multi-physics interactions.
- Scalability: Due to its scalability, MUMPS is often the software of choice when it comes to solving many problems on high-performance computers. It addresses the challenges associated with saturating the memory resource by being able to solve problems of millions of degrees of freedom.

MUMPS comes as one of the direct solvers, and as a result, it can be utilized as a solver of linear systems within the COMSOL Multiphysics package. Due to the effective utilization of MUMPS in controlling large sparse systems which arise from the finite element mesh, it was opted for this study. Using MUMPS was complimented with timely and reproducible outcomes, even on stiff systems and fine configurations in the model [23]. One of the advantages of MUMPS is that it is possible to choose it depending on the solver configuration for the relevant applications, but the software has put MUMPS automatically for another physics parameter. The direct method of solution using MUMPS was very advantageous in these non-linear and/or stiff problems in that it opens a way for one to solve very hard-to-converge problems with complicated geometry and boundary conditions [24] [1].

2.2.7 Generalized Minimal Residual (GMRES)

The Generalized Minimal Residual (GMRES) iterative solver was employed to handle the large, sparse, and non-symmetric systems of linear equations generated by the finite element discretization. GMRES is well-suited for such systems, particularly when the matrix is non-symmetric, which commonly arises in simulations involving

fluid dynamics, electromagnetics, and other complex multi-physics problems. Key features:

- Iterative Solver: GMRES is an iterative solver, meaning it approaches the solution by progressively refining approximations rather than computing an exact solution in one step, as direct solvers do. This characteristic makes GMRES highly efficient for solving large systems where direct methods may be computationally expensive or require excessive memory.
- Krylov Subspace Method: As a member of the Krylov subspace family of methods, GMRES iteratively constructs an approximation to the solution in a subspace defined by the residual vectors of the system. This process enables the solver to handle non-symmetric and potentially indefinite systems effectively.
- Non-symmetric Systems: GMRES is particularly well-suited for non-symmetric matrices, which commonly occur in problems such as fluid flow, convection-diffusion, and electromagnetics. Unlike methods like Conjugate Gradient (CG) that are restricted to symmetric positive-definite systems, GMRES handles a broader range of matrices without additional reformulation.
- Convergence Behavior: While GMRES often converges quickly for well-conditioned systems, its convergence rate can slow down for ill-conditioned problems. In such cases, the use of preconditioners can accelerate the convergence by improving the condition number of the matrix.

Within COMSOL Multiphysics, GMRES is often selected for its ability to handle large-scale, non-symmetric problems, particularly in multi-physics simulations where coupling between different fields leads to complex matrix structures. In this study, GMRES was chosen due to its capacity to efficiently solve the large systems produced by the fine mesh discretization and the non-linearity of the model [23]. GMRES was especially useful in simulations where the non-symmetric nature of the system precluded the use of simpler iterative methods. By iteratively refining the solution within a Krylov subspace, GMRES allowed the solver to handle non-linearities without requiring excessive memory resources or computational time. [29] [30]

Generalized Minimal Residual (GMRES) was used in combination with two different solvers/preconditioners: PARDISO and the Domain Decomposition (DD) Schwarz Preconditioner. These configurations were employed to handle large, non-symmetric linear systems generated by multi-physics simulations. Both approaches provided robust solutions for complex systems, but their characteristics made them suitable for different types of problems.

2.2.7.1 GMRES with PARDISO

PARDISO (Parallel Direct Solver) is a high-performance, multi-threaded sparse direct solver often used in conjunction with GMRES to handle large-scale sparse systems. This hybrid approach allows for efficient solutions of non-symmetric linear systems, particularly in models where the size of the problem precludes the use of purely direct solvers due to memory constraints.

- PARDISO as Preconditioner: In this configuration, GMRES is combined with

PARDISO, where PARDISO serves as a preconditioner to improve the convergence of GMRES. The preconditioning process reduces the condition number of the matrix, leading to faster convergence and a more efficient solution for the system. PARDISO's parallel capabilities make it particularly well-suited for problems where high computational efficiency is required, and its ability to handle unsymmetric matrices makes it a natural fit for non-symmetric problems encountered in fluid flow and multi-physics models.

- Parallelization and Memory Management: PARDISO efficiently utilizes memory through dynamic memory allocation and multi-threaded execution, making it ideal for large-scale problems. By pairing it with GMRES, the computational load can be distributed across multiple processors, thereby speeding up the overall solution process [31] [32].

In this study, GMRES with PARDISO was used to solve large systems where direct solving methods alone would have been inefficient due to memory constraints. The combination provided a robust and scalable solution, balancing memory use with high performance.

2.2.7.2 GMRES with Domain Decomposition (DD) Schwarz Preconditioner

The DD Schwarz Preconditioner is another effective method for accelerating the convergence of iterative solvers like GMRES. Domain decomposition techniques, particularly Schwarz methods, are designed to break down the global problem into smaller subproblems, each of which can be solved independently. This makes them highly suitable for parallel computing and large-scale systems with complex geometries or multi-physics interactions.

- Schwarz Method: In the Additive Schwarz Method, the domain is decomposed into overlapping or non-overlapping subdomains, and each subdomain problem is solved individually. The results are then combined to form an approximate solution for the global problem. This division reduces the size and complexity of the linear system that GMRES needs to solve.
- DD Schwarz as a Preconditioner: When used as a preconditioner, the DD Schwarz method improves the spectral properties of the linear system, enhancing the convergence rate of GMRES. The Schwarz method is particularly effective for solving problems with irregular domain geometries and heterogeneous materials, which are common in multi-physics simulations. By leveraging parallelism, the Schwarz preconditioner ensures that subdomain solutions can be computed independently, making it well-suited for distributed memory systems and large-scale parallel computing.
- Parallel Scalability: The domain decomposition approach provides significant scalability advantages, especially in massively parallel environments. Each subdomain solution can be computed concurrently, allowing for efficient utilization of computational resources [33] [35].

In this study, GMRES with DD Schwarz Preconditioning was used for highly nonlinear, multi-domain problems where a standard preconditioning technique might not have been sufficient. The ability of the Schwarz method to divide the domain into smaller, more manageable problems resulted in improved convergence rates and

reduced computation times.

2.3 Finite Element Method (FEM)

The Finite Element Method (FEM) is a powerful numerical technique for solving complex engineering and mathematical problems. It is widely used for structural analysis, heat transfer, fluid dynamics, electromagnetic field analysis, and many other areas. FEM breaks down a complex problem into smaller, manageable subproblems, known as finite elements, which are connected at discrete points called nodes. Each element can have different properties, making FEM highly versatile and effective for analyzing systems with varying materials, geometries, and boundary conditions.
This section provides a comprehensive explanation of the FEM theory and its application in computational simulations, particularly in structural analysis and thermal management.

2.3.1 Basic Concept of FEM

At its core, FEM approximates a continuous domain into a set of discrete elements, transforming complex equations (usually partial differential equations, PDEs) into a system of algebraic equations. This approach enables the approximation of real-world physical phenomena over complex geometries and irregular shapes by subdividing them into simpler shapes, typically triangular or quadrilateral elements in 2D, and tetrahedral or hexahedral elements in 3D.
The key steps in FEM include:

- **Discretization of the Domain:** The continuous physical domain is divided into a finite number of smaller regions or elements.
- **Selection of Approximation Functions:** Within each element, approximation functions (often polynomials) are used to represent the solution. These functions are typically expressed in terms of the nodal values of the elements.
- **Assembly of Global System:** The individual element equations are assembled into a global system of equations that models the entire problem.
- **Imposition of Boundary Conditions:** Physical boundary conditions, such as fixed supports, applied loads, or temperature constraints, are incorporated into the system of equations.
- **Solution of the System:** The global system of equations is solved using numerical techniques (e.g., Gaussian elimination or iterative solvers) to obtain the approximate solution over the entire domain.

2.3.2 Discretization of the Domain

The first step in the FEM process is the discretization of the physical domain. In this step, the continuous domain Ω of the problem is subdivided into smaller subdomains or finite elements. The collection of these elements forms the mesh, which approximates the geometry of the problem.

Each element is interconnected by points called nodes, where the solution is calculated. Depending on the problem, elements can be in various shapes:

- **1D:** line segments
- **2D:** triangles, quadrilaterals
- **3D:** tetrahedrons, hexahedrons, etc.

The goal of discretization is to approximate the original domain with a finite set of simpler geometries, allowing for the reduction of complex differential equations to a system of algebraic equations.

2.3.3 Shape Functions and Approximation

Once the domain is discretized, FEM employs shape functions (also called interpolation functions) to approximate the solution within each element. For each element e, the solution $u(x)$ at any point inside the element is expressed as a weighted sum of nodal values of the element:

$$u(x) \approx \sum_{i=1}^{n} N_i(x) u_i$$

Where, $N_i(x)$ are the shape functions associated with the nodes of the element, u_i are the nodal values (e.g., displacements, temperatures) at node i, n are the number of nodes in the element. Shape functions vary depending on the type of element used (e.g., linear, quadratic). For a 1D element, the simplest linear shape functions for two nodes are:

$$N_1(x) = \frac{x_2 - x}{x_2 - x_1}, N_2(x) = \frac{x - x_1}{x_2 - x_1}$$

These functions ensure that the value of the field variable $u(x)$ is exactly represented at the nodes while being interpolated in between.

2.3.4 Derivation of the Element Equations

To derive the governing equations for each element, the weak form of the governing differential equation must be obtained. This process typically involves the Galerkin method, which multiplies the governing equation by a test function (often chosen to be the shape function itself) and integrates over the domain.
For example, consider the 1D Poisson equation for heat conduction:

$$-\frac{d}{dx}\left(k\frac{du}{dx}\right) = f$$

where, k is the thermal conductivity, f is the heat source term and $u(x)$ is the temperature distribution.
Multiplying by a test function $v(x)$ and integrating over the domain gives the weak form:

$$\int_\Omega v(x)\left(-\frac{d}{dx}\left(k\frac{du}{dx}\right)\right)dx = \int_\Omega v(x) f dx.$$

Applying integration by parts to the left-hand side to reduce the order of the derivative:

$$\int_\Omega \frac{dv}{dx} k \frac{du}{dx} dx - \left[vk \frac{du}{dx} \right]_{\partial\Omega} = \int_\Omega v f dx.$$

The boundary term $\left[vk \frac{du}{dx} \right]_{\partial\Omega}$ accounts for Neumann boundary conditions, while Dirichlet boundary conditions are applied directly to the function values at the boundaries. These boundary conditions will be discussed in Section 2.3.6.

2.3.5 Element Stiffness Matrix and Assembly of Global Equations

Once the weak form is established, the problem is reduced to an algebraic form, typically written as:

$$K^e u^e = f^e$$

where, K^e is the element stiffness matrix, representing the system's response to applied forces, u^e is the vector of unknowns (e.g., nodal displacements or temperatures) for element e and f^e is the vector of external forces acting on the element. The stiffness matrix K^e for each element is computed using the shape functions and their derivatives.
For example, in the case of 1D heat conduction, the stiffness matrix for element e is:

$$K^e = \int_{\Omega^e} k \frac{dN_i}{dx} \frac{dN_j}{dx} dx$$

The global stiffness matrix K s assembled by combining the element stiffness matrices from all elements in the mesh. This assembly process involves placing each K^e n the correct position in the global matrix based on the element's connectivity to the nodes.
Once assembled, the system of equations takes the form:

$$Ku = f$$

where, K is the global stiffness matrix, u is the global vector of unknowns and f is the global force vector.

2.3.6 Boundary Condition

To solve the system of equations, appropriate boundary conditions must be applied. There are two primary types of boundary conditions in FEM:

- **Dirichlet boundary conditions:** Dirichlet boundary conditions specify the value of the field variable at the boundary of the domain. This type of condition is often encountered in structural analysis where displacements are fixed (e.g., a clamped beam with zero displacement at one end), or in heat transfer problems where the temperature is fixed along a surface.

  $$u(x) = u_{prescribed} \text{ on } \Gamma_D$$

  where $u(x)$ represents the solution (e.g., displacement, temperature), and Γ_D is the part of the boundary where the Dirichlet condition is applied.

- **Neumann boundary conditions:** Neumann boundary conditions specify the flux or gradient of the field variable across the boundary. In structural mechanics, this corresponds to an applied force or stress at a boundary. For thermal problems, it may represent a heat flux or thermal gradient at the boundary.

$$\frac{\partial u}{\partial n} = q_{prescribed} \text{ on } \Gamma_N$$

  where $\frac{\partial u}{\partial n}$ is the derivative of the solution along the boundary normal vector, and Γ_N is the boundary segment where Neumann conditions are applied.

Incorporating boundary conditions into the system may involve modifying the global stiffness matrix and force vector, or directly substituting the known values into the system.

2.3.7 Solution of the System

After assembling the global stiffness matrix and applying boundary conditions, the final system of equations is solved for the unknowns at the nodes. The solution methods vary depending on the size and complexity of the matrix. For small systems, direct methods like Gaussian elimination are commonly used. For large systems, iterative solvers such as the Conjugate Gradient Method or GMRES (Generalized Minimal Residual) are employed.

2.4 Optimization

2.4.1 Particle Swarm Optimization(PSO)

Particle swarm optimization (PSO) is a computational method used to optimize a wide range of problems by mimicking the social behaviour of birds flocking or fish schooling. The flow chart in Figure 2.2 shows how it works[9].

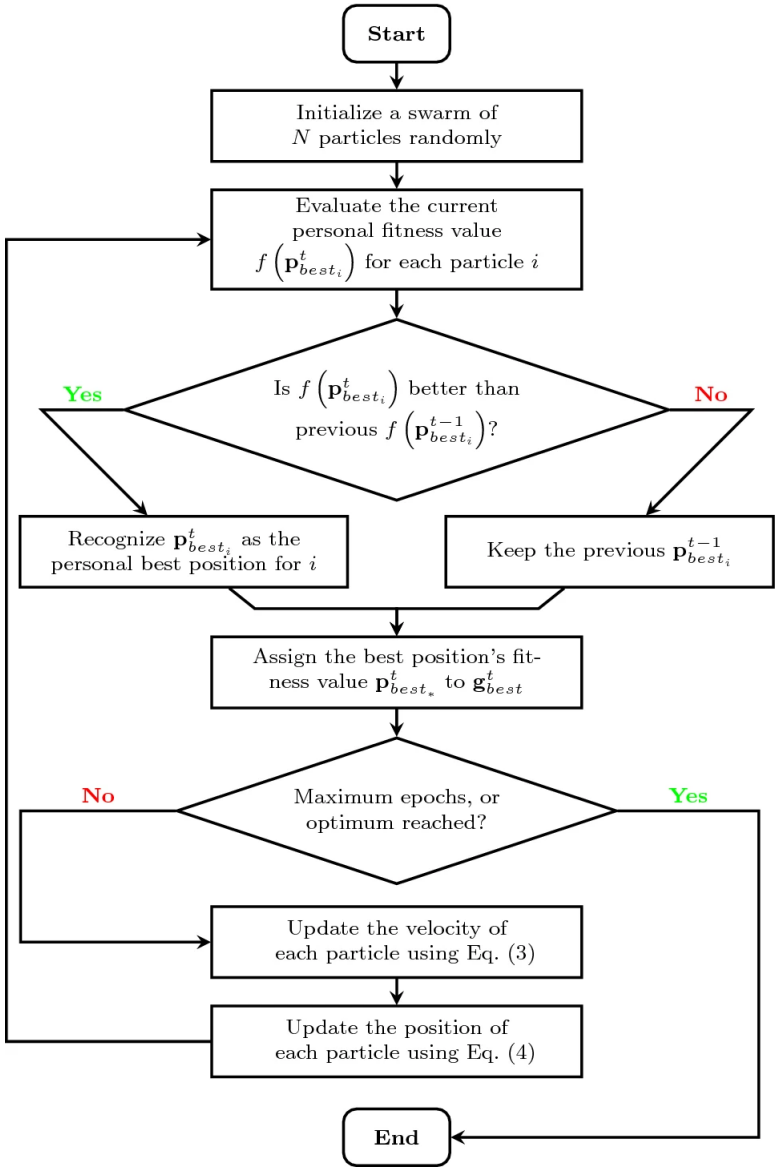

Figure 2.2: PSO flow chart[9]

In PSO, a group of potential solutions, called particles, moves through the solution space to find the optimal solution. Each particle represents a possible solution and has a position and velocity. The particles move around the solution space, guided by their own best-known position and the best-known positions of their neighbours. The movement of each particle is influenced by two factors: its own experience and the collective experience of the swarm.
Initially, particles are randomly placed in the solution space. Each particle's fitness is evaluated based on the objective function, which measures how good the solution is. As particles explore the solution space, they update their velocities and positions based on the best positions they have found so far and the best positions found by the entire swarm.
The update rules for velocity and position are mathematical formulas that take into account the particle's current velocity, its distance from its own best-known posi-

tion, and its distance from the swarm's best-known position. These rules ensure that particles are attracted to the best solutions found so far while still exploring new areas of the solution space.
The process is iterative, with particles continually adjusting their velocities and positions to improve their fitness. Over time, the swarm converges towards the optimal solution, balancing exploration and exploitation to avoid local optima and find the best possible solution.

3
Background

To better understand the target sound source, a study of the cooling fan and the surrounding space is undertaken through reading papers and visits to the Volvo truck lab.

3.1 Sound Source Characterization

The sound source needed to be studied is a cooling fan from a heavy-duty truck to lower the engine or battery temperature of contemporary electronic trucks. A fan with seven blades and a radius of 0.3 meters[20] has been used as the reference source, as seen in Figure 3.1.

Figure 3.1: Cooling fan shape[20]

The cooling fan tonal noise spectrum was measured at 60% duty cycle in free space. One could see that, significant tones exist in the noise. Noise peaks are closely related to blade passing frequency (BPF). BPF is defined as: Number of blades times rotational speed per second(RPS). Given the resolution of fan per minute(RPM) measured by sensors is 2322Hz, BPF in this case is 271Hz. The SPLs of the fan as a function of the order are shown in Figure 3.2. The order on the x-axis represents the multiple RPS in a unit of frequency. The 7th-order peak, which is the highest peak, is BPF. On the other hand, the broadband spectra study of the fan noise is shown in Figure 3.3. One can see that a frequency band from 300–5000 Hz is interesting

to reduce. However, it's hard to realize such a large band reduction and frequency above 2000 Hz can be easily absorbed by noise shields and porous material. With the principle from Mendel's book[16], a proper panel with a depth of less than a quarter of the wavelength, in this case, 4.3 cm can do a good job for frequencies above 2000 Hz.

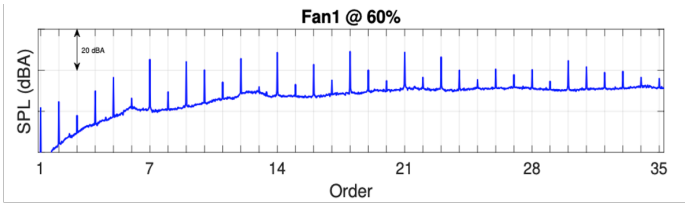

Figure 3.2: Tonal noise spectra of the fan[20]

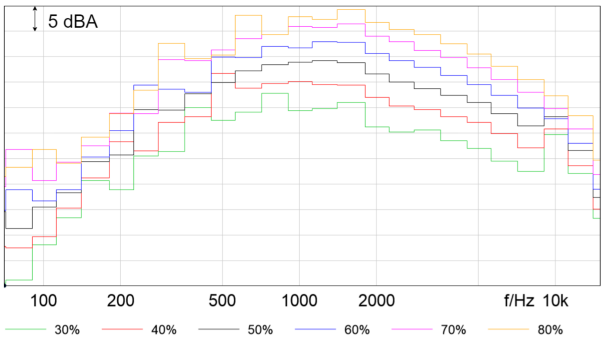

Figure 3.3: Broadband spectra of the fan under different duty circles[20]

Also, the flow velocity downstream is about 85% of the air velocity v at the fan tip. v is also called peripheral velocity, which can be calculated as:

$$v = \frac{RPM * D}{60} \tag{3.1}$$

With D as the diameter of the fan. In this particular situation, the flow velocity is around 20 m/s. To simulate the real situation, a Mach number of 0.05/0.06 and 0.1 is used in the further flow-acoustic coupled discussion.

3.2 Sound Wave Propagation Path

Such a cooling fan is located underneath the cab of a truck. It sits within the engine compartment and is mounted near the front of the engine or battery cluster. The fan is also located behind the radiator, which is mounted at the front of the truck with the grille. The fan draws air through the radiator to help cool the engine coolant circulating through it.
The sound source is generally half enclosed by a truck firewall together with some insulation mats. This design can originally reduce noise from the cooling fan and tyre noise, especially high-frequency noise. Surfaces under the firewall include hard metal

surfaces like engine blocks, transmission housings, and other structural components. This would cause reflections of high-pitched noise. The chassis and undercarriage are underneath the sound source. Such confined geometry may also lead to reflections and interferences at certain frequencies. To make the cooling fan functional, the flow must not be blocked in such an area.
In conclusion, the metamaterial group this thesis raised should be embedded in the firewall panel so that the change of the zone condition can be minimized. In this case, most flow will go in the vertical direction of the group while acoustic pressure in the form of air oscillation can be reduced. Meanwhile, according to the noise spectra, one should either try to reduce the noise peak at the fan's BPF and its harmonics(integral multiples of the fundamental frequency) or focus on broadband noise absorption on the frequency 300-2000 Hz.

4
Methods

Acoustic metamaterials are typically presented in the form of periodic structures. However, due to the complexity involved in designing the entire structure being above the scope of the thesis, a single cell of the metamaterial was designed and validated here. In this chapter, one presents a general methodology to design acoustic metamaterial cells, which can be used as a solution for several acoustic issues. The full approach will be introduced, and then some detailed methods will be explained. While some techniques might not have been employed in the metamaterial analysis at first, they can be surprisingly helpful in cell design.
In Section 4.2 there is a brief overview of the approach taken to set up the simulations that are the focus of this work. It outlines the concepts of the simulation domain, boundary conditions, and meshing strategies effective for both CFD and acoustic simulations. The aim of the CFD simulations is the computation of the airflow, and the aim of the acoustic simulations is the simulation of sound, in this case, owing to the cooling fan of the truck. The use of many types of meshing methods and boundary conditions is important as this enables better representation of the airflow and noise, as well as eases the modeling of the simulations.

4.1 Metamaterial Design Method

The design process begins with conceptualization, where the desired acoustic properties are identified, such as sound absorption, transmission loss, or bandgap creation. During this phase, the target application (e.g., noise control, soundproofing, or audio enhancement) is also determined. Multiple structures are proposed, followed by brainstorming to gather and select various ideas.
The next step involves specifying the geometric parameters of the structure. These parameters include the size, shape, arrangement, and material composition of the unit cells that will form the metamaterial. This requires describing the structure mathematically.
To facilitate the design process, a computational approach is employed, often using Matlab. This stage includes several sub-steps: parametrization, parametric design, and final optimization. Firstly, to link the parameters with the target coefficient, the first step is to model the acoustic transfer within the geometry, known as parametrization. Two methods can be used: the equivalent electrical circuit model(EEC) and the transfer matrix method(TMM). The former is more popular when both electronic and mechanical components are involved, while the latter is

more suitable for multiple separated acoustic layers combined. Normally, the two can be used in almost all cases. But as a rule of thumb, when the acoustic impedance is known and the layers are combined in sequence, TMM is more suitable and convenient. EEC, however, can calculate the acoustic impedance in a complex content. EEC can also be represented by TMM using specific equations. This will be explained shortly in the following sections.

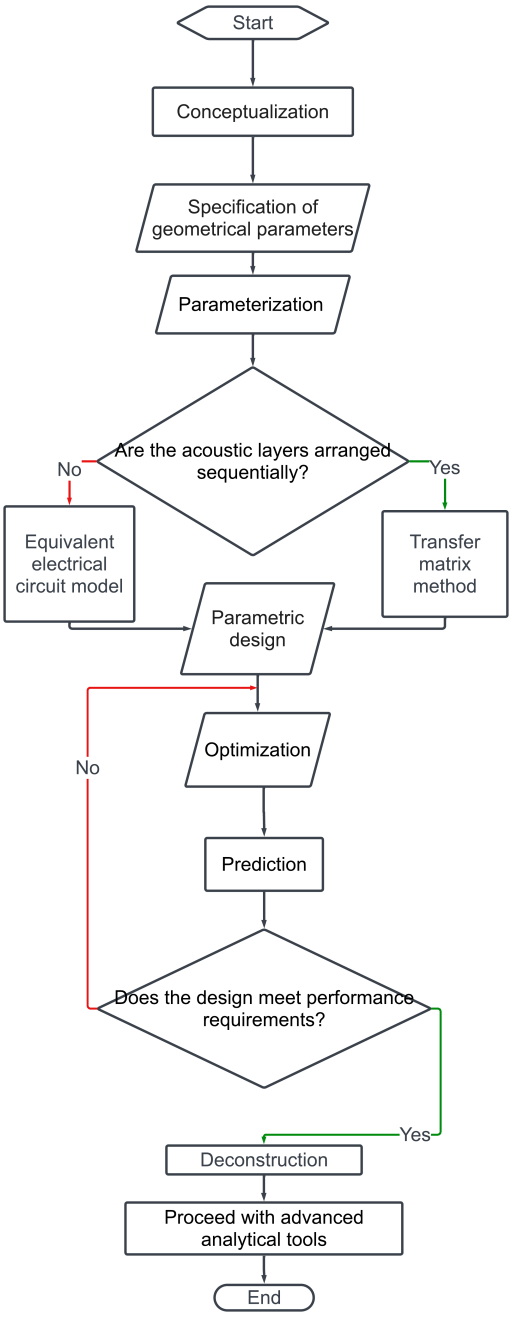

Figure 4.1: Acoustic metamaterial design methodology flowchart

Next is the parametric design, which involves sensitivity analysis to determine which parameters most affect the target outcomes. By doing so, three to five key param-

eters are selected for further computation in the optimization function. Analytical methods are applied to derive initial formulations and equations governing the behaviour of the metamaterial. Specific mathematical formulations model the relationship between the design parameters and the desired acoustic properties.
With the parametric model in place, optimization techniques are used to fine-tune the design parameters for the target frequency band. Several methods can be used. One interesting theory is a graph-theory approach applied to an EEC[8]. In this paper, PSO is employed. This step may involve iterative simulations and adjustments to achieve the best possible acoustic performance according to the specified objectives.
After completing these steps, the performance of the structure can be predicted and further refined as needed. A 3D model may be created using the final designed structure's dimensions and shape. It can be used with advanced simulation and validation programs like *COMSOL*, *Star-CCM+*, and others. Furthermore, this stage will provide the opportunity to integrate acoustic in other multi-physical fields.

4.1.1 Parametrization

4.1.1.1 EEC

EEC in this context is a way to represent acoustic systems using electrical components, which is widely used to combine electrical, mechanical, and acoustical elements into one circuit. This is also called the Electro-Mechano-Acoustical Circuits model in some textbooks[3]. Transducers are introduced here to convert from acoustics pressure to mechanical force and finally to electronic power. This method helps to understand and analyze acoustic behaviour in complex situations by systematic analysis of electrical circuits.
To represent acoustic components as circuit elements, it is important to first establish the mechanical components that correspond to their electrical counterparts. Since mechanical force is simply acoustic pressure multiplied by a constant factor (area), the acoustic equivalent circuit can adopt the same component impedance as the mechanical components. In a mechanical system, when a force F is applied as an input, a resulting velocity u can be observed in the system, analogous to how voltage and current relate in electrical systems. In the system, mechanical resistance gives a constant impedance of R_M, resembling an electrical resistance. According to Newton's second law, mechanical mass M_M in a system works as $F = M * \frac{\partial u}{\partial t}$, which leads to $F = Mj\omega u$ [1]. The impedance of mass is now $\frac{F}{u} = j\omega M_M$, analogous to the inductance. The same magic applies to mechanical compliance C_M, which is defined as displacement divided by force. As $F = \frac{1}{C_M}\int_0^t u dt$, makes $F = \frac{1}{C_M}\frac{u}{j\omega}$. The impedance of mass is now $\frac{F}{u} = \frac{1}{j\omega C_M}$, analogous to the capacitance.
The circuit symbols, their corresponding electrical element and the equivalent mechanical analogy are described in Table 4.1.

[1] $u = e^{j\omega t}, \frac{\partial u}{\partial t} = j\omega u$

Symbol		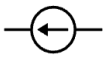		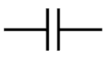	
Electrical Impedance analogy	e_o	i_o	R_E	$\frac{1}{j\omega C_E}$	$j\omega L_E$
	Voltage source	Current source	Electrical resistance	Capacitance	Inductance
Mechanical Impedance analogy	F_o	u_o	R_M	$\frac{1}{j\omega C_M}$	$j\omega M_M$
	Force source	Velocity source	Mechanical resistance	Mechanical compliance	Mass

Table 4.1: Circuit elements for electrical system and mechanical system

To understand this better, imagine one has a Helmholtz resonator presented in Figure 2.1. The air moving inside the resonator can be seen like an electric current in a wire. The mass of the air M in the neck resists changes in movement, just like an inductor resists changes in current. The air with stiffness of C meanwhile inside this cavity acts like a spring and can store and release energy, just like a capacitor can store and release electrical energy. Finally, the wall of this structure provides some viscosity R, which converts sound energy into heat, reducing the sound, just like a resistor converts electrical energy into heat, reducing the current.
Using EEC, complex acoustic systems can be simplified and analyzed using circuit and Electrical circuit basics shown in Figure 4.2.

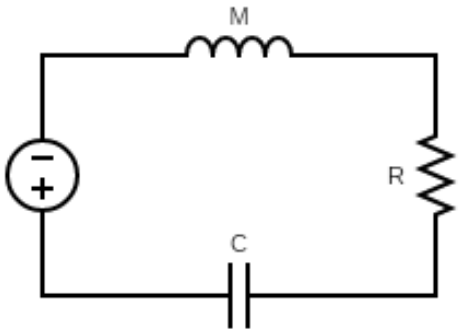

Figure 4.2: Equivalent electrical circuit of Helmholtz resonator

4.1.1.2 TMM

TMM describes the acoustic layer in the matrix. Multiplying matrixes enables the combination of different acoustical layers in one system. Image a homogeneous and isotropic 1D material extending from x=0 to x=l. The acoustic pressure p and

particle velocity v at position x=0 can be described based on pressure p and particle velocity at position x=l and the acoustic impedance of the material Z.

$$\begin{bmatrix} p \\ v \end{bmatrix}_{x=0} = T * \begin{bmatrix} p \\ v \end{bmatrix}_{x=l} = \begin{bmatrix} cos(kl) & jZsin(kl) \\ jsin(kl)/Z & cos(kl) \end{bmatrix} \begin{bmatrix} p \\ v \end{bmatrix}_{x=l} \tag{4.1}$$

Where the wave number $k = \omega/c$. c is the sound speed, which is decided by density ρ and bulk modulus K with $c = \sqrt{K/\rho}$. The acoustic impedance is defined as $Z = \sqrt{\rho K}$ and $j = \sqrt{-1}$ is the imaginary unity.

With the knowledge of this, one can then combine several sublayers by

$$T_{tot} = T_1 * T_2 * T_3 \tag{4.2}$$

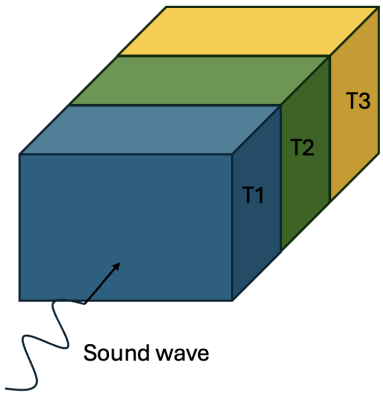

Figure 4.3: Schema of several layers

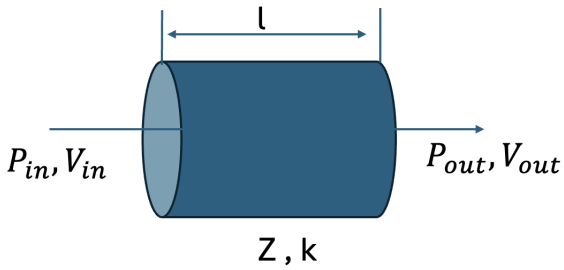

(a) An arbitrary acoustic tube

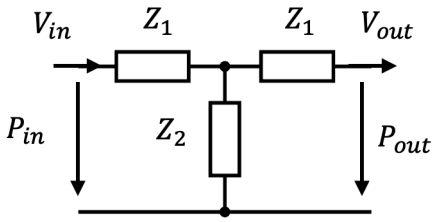

(b) An assumption circuit

Figure 4.4: An arbitrary acoustic tube and the equivalent circuit. It has a length of L and, an impedance of Z. The input sound pressure and velocity are denoted as p_{in}, v_{in}. The output sound pressure and velocity are denoted as p_{out}, p_{out}.

One thing to notice is that the two methods introduced above do not only exist independently. They can be transformed into each other in certain situations. For instance, in the case of a duct, one can assume acoustical impedance as Z_1,Z_2. The

position described in the equivalent circuit is assumed as Figure 4.4b. According to two-port equations[4], the following relations hold,

$$1 + \frac{Z_1}{Z_2} = cos(kl) \tag{4.3}$$

$$\frac{1}{Z_2} = j\frac{1}{Z}sin(kl) \tag{4.4}$$

Then leads to,

$$Z_1 = jZtan\frac{kl}{2} \tag{4.5}$$

$$Z_2 = -jZ\frac{1}{sin(kl)} \tag{4.6}$$

For all small wavelengths that $l << \lambda$, by considering the impedance of the tube is affected by the area S, the following approximations apply,

$$Z_1 = jZ\frac{kl}{2} = \frac{1}{2}j = \frac{1}{2}j\omega l\frac{\rho}{S} \tag{4.7}$$

$$Z_2 = -jZ\frac{1}{kl} = \frac{1}{j\omega KSl} \tag{4.8}$$

By setting M=ρ/S and C=KSl an equivalent electrical model with two inductors and one capacitor can be formed as the Figure 4.5 shows,

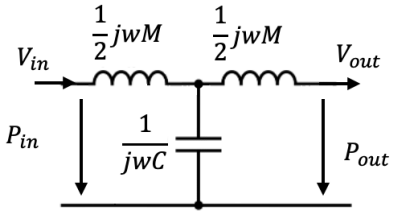

Figure 4.5: Equivalent circuit of the tube

4.1.2 Parametric Design

One used manual sensitivity analysis to do the parametric design in this thesis. A relatively small number of parameters and a clear specification of parameters make manual sweep a simple and quick method to apply. Generally speaking, this method is to manually vary one parameter while keeping others constant. A rough way to quantify the sensitivity of a parameter is as follows. One sets all the parameters in a default value to define a baseline. Secondly, one selects a parameter and introduces small variations to test. One keeps all other parameters constant and manually adjusts the value of the parameter n times under consideration. Each adjustment is applied using the same gradient. One should vary above and below the baseline value to capture the full sensitivity range. Plot the result in one figure to see the change.

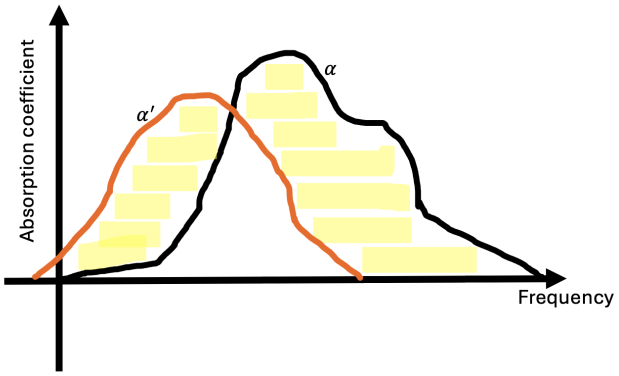

Figure 4.6: Schema of sensitivity calculation

Observation is crucial while quantification of the sensitivity gives a more subjective way to the analysis. A sensitivity argument measures how much the absorption coefficient changes in response to a percentage change in the parameter, providing insight into which parameters are most influential. It is defined as the average change in the absorption coefficient (integrated over the frequency range) divided by the percentage change in the parameter. A Schema of such is demonstrated in Figure 4.6, where the yellow-shaded area highlights the difference between the baseline (represented by the black line) and the altered parameter (represented by the orange line).

$$\text{Averaged changed area} = \frac{\sum_{i=1}^{i=n} \int_{f_{min}}^{f_{max}} |\alpha_i^{'} - \alpha_i| df}{n} \tag{4.9}$$

$$\text{Incremental degree} = \frac{\text{Gradient}}{\text{Baseline}} \tag{4.10}$$

The last step is to repeat for other parameters and rank the sensitivity.

This is a crude approach, though, with limited options for a single-cell design. In a huge industrial setting, a more accurate and respectable model needs to be discussed.

4.1.3 Optimization

The optimal target fitness function in this project is defined as follows:

$$\text{fitness} = \int_{f_{min}}^{f_{max}} \alpha(\text{Senstive parameters}) df \tag{4.11}$$

The goal is to maximize the absorption coefficient α over the specified frequency range. In this context, the MATLAB function *particleswarm*[2] is used to find a vector x that minimizes a given objective function. To apply this to the fitness function, the target value for *particleswarm* is set as:

[2]Particle swarm optimization from Global Optimization Toolbox.
https://se.mathworks.com/help/gads/particleswarm.html

$$1 - \text{fitness} \tag{4.12}$$

This ensures that the algorithm can effectively maximise the original fitness function.

4.2 CFD Simulation

The initial and crucial step, in the simulation procedure involves creating the model. Because geometry provides a detailed representation of the domain of interest, it serves as the foundation on which the entire simulation is built. To ensure the importance and reliability of the simulation outcomes, this geometric model must accurately depict the dimensions, shape and relevant attributes of the object or system being analyzed.

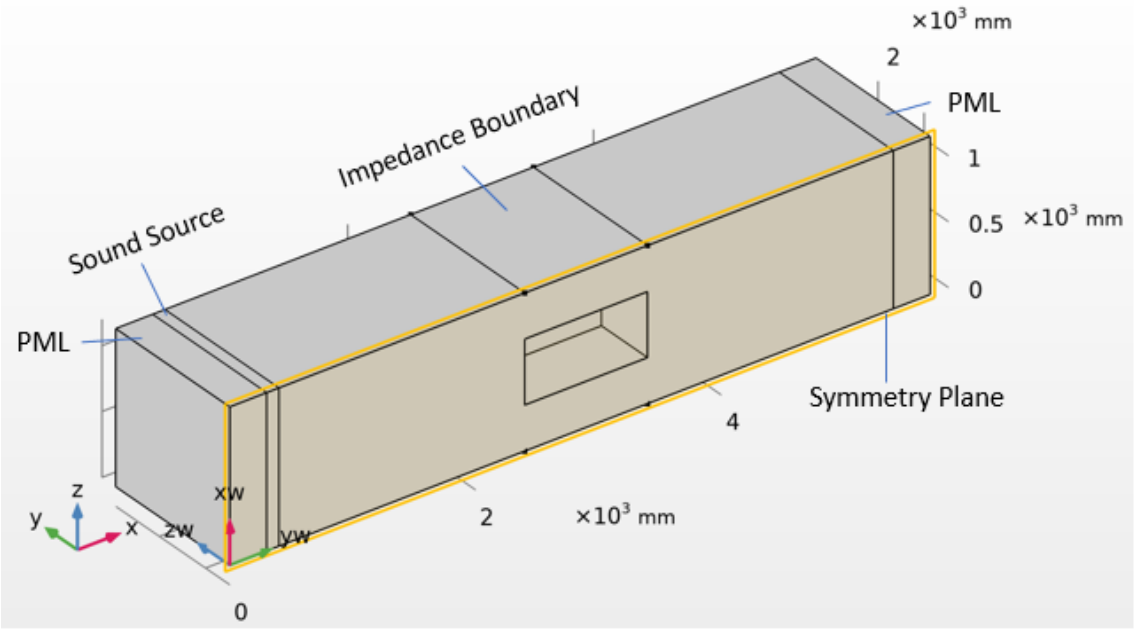

Figure 4.7: Geometry of the simplified under-cab region

Simplified geometry of the under-cab region and associated computational domains are displayed in Figure 4.7. A computational method for simulating the absorption of acoustic waves at a simulation domain's boundaries is called Perfectly Matched Layers (PML) and it is situated at either end of the domain. Reflections from the simulation domain edges are avoided using this technique which could affect how accurate the simulation results are. Every PML has a width of 300 mm. The sound source domain is placed right after the first PML and it replicates the cooling fan in the under-cab region with a plane wave simplification, propagating in the x direction. The main under-cab region is 5000 mm long to let the flow develop. Also, there is a component box located at the centre of the main domain to represent all the components in the under-cab region. The dimensions of this box are 1000x300x500 mm, while the dimension of the entire geometry is 5700x1200x2474 mm. Since the

geometry is symmetric about the xz-plane, a symmetry condition is introduced at the mid-plane to reduce computational effort.

4.2.1 Meshing - CFD

Once the geometry is defined, the next step is meshing, which involves dividing the geometric model into smaller, finite elements. This discretization process transforms the continuous geometry into a finite element model, enabling the numerical methods to approximate the solutions to the governing equations over these elements. The quality and granularity of the mesh significantly influence the accuracy and efficiency of the simulation, making it a pivotal step in the computational analysis workflow. In order to properly resolve the boundary layer, prism cells were used. To do this y^+ had to be less than one for the first cell. The cell height was calculated using the guidelines from ITTC [14] as

$$y = \frac{y^+ L_{PP}}{Re\sqrt{C_f/2}} \tag{4.13}$$

Where L_{PP} is the length of the entire domain. C_f was obtained from

$$C_f = \frac{0.075}{(\log_{10}(Re-2))^2}. \tag{4.14}$$

The PML and source regions are meshed using quadrahedral cells, as seen in Figure 4.8 with maximum and minimum cell size 15.8 mm and 0.244 mm, respectively and a growth rate of 1.05. The rest of the domain is meshed using tetrahedral cells with the same cell configuration as mentioned earlier. This was done after conducting a mesh-independent study in order to reduce computational cost. Boundary layer cells are used on walls with 10 layers and a total thickness of 0.590 75 mm, which was calculated using (4.13) with a maximum Reynolds number, $Re_{Ma=0.1} = 2.7\text{x}10^6$. The final meshed domain for the CFD study can be seen in Figure 4.8 and Figure 4.9.

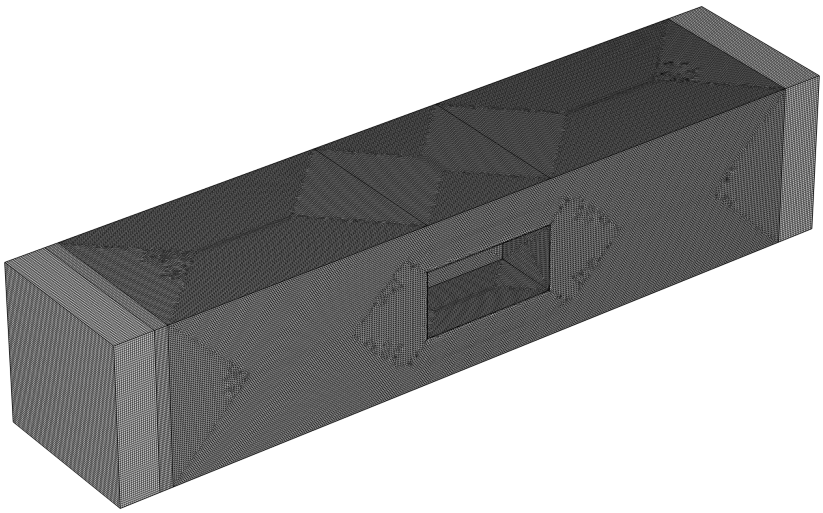

Figure 4.8: Mesh for the CFD domain

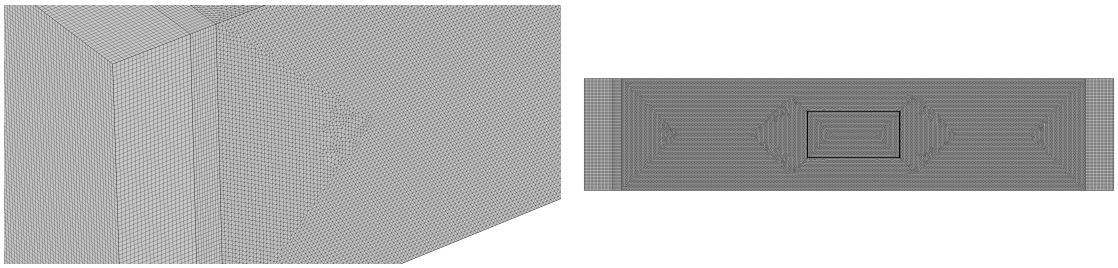

(a) Mesh transition **(b)** Mesh front view

Figure 4.9: Detailed CFD mesh plots

4.2.2 Boundary Condition - CFD

For both the cases in this study, the inlet condition is set to a velocity inlet with a fully developed flow condition and the velocity magnitude varying between 34.3 m/s and 17.15 m/s corresponding to mach 0.1 and 0.05, respectively. On the other hand, pressure condition with static pressure, $p_0 = 0\,\text{Pa}$ is set as an outlet boundary condition. The flow propagates along the $x-$direction. The symmetry plane as seen in Figure 4.7 is set as symmetry boundary condition and the rest of the surfaces including the inner box are set as walls. The CFD simulation is carried out in a steady state and is set to use the SST $k-\omega$ turbulence model, as discussed in Chapter 2.

4.3 Mapping and Acoustic Setup

After obtaining the solution for CFD simulation, the flow variables are mapped to the acoustic mesh using background flow coupling, while mapping the pressure, velocity and turbulent viscosity. This is done using the direct MUMPS solver in COMSOL multiphysics, as discussed in an earlier Section 2.2.6.

4.3.1 Meshing - Acoustics

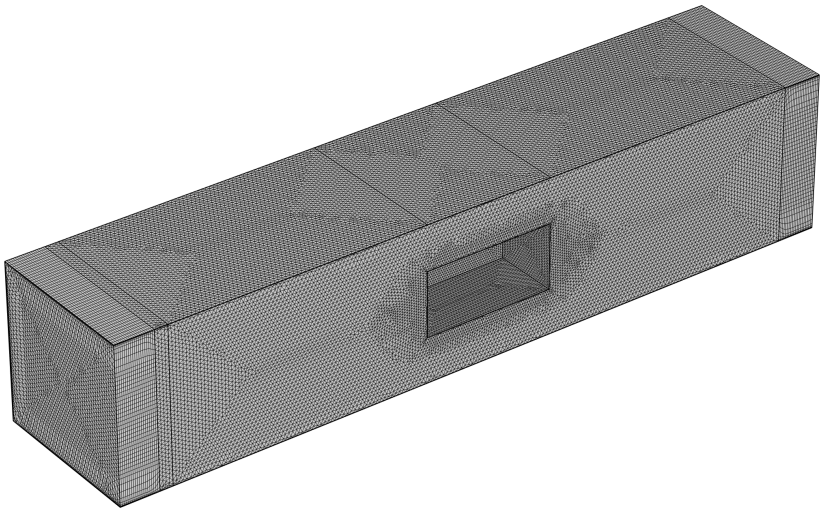

Figure 4.10: Mesh for the acoustic domain

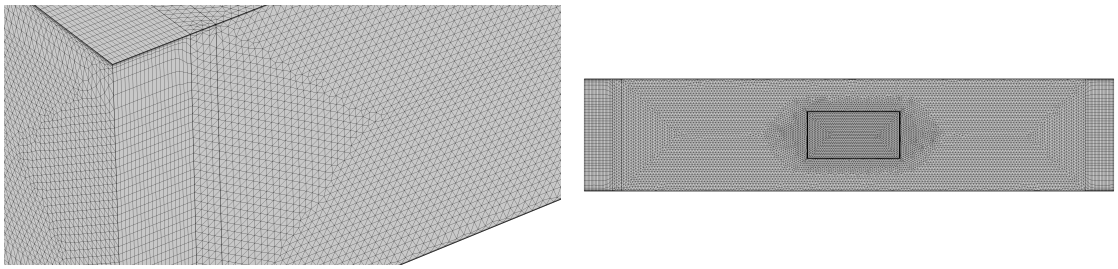

(a) Mesh transition **(b)** Mesh front view

Figure 4.11: Detailed acoustic mesh plots

To correctly map the fluid flow variables to the acoustic domain, an acoustic mesh setup is built. Unlike the CFD mesh, the acoustic mesh is relatively coarser since a very fine mesh would dampen the acoustic wave. However, if the mesh is too coarse, the wave will not propagate accurately downstream. As a general rule of thumb, the largest cell size for an acoustic mesh is usually 4-5 times smaller than the wavelength of the sound wave. The wavelength (λ) of the sound wave is calculated using:

$$\lambda = \frac{v}{f}$$

where, v is the velocity of sound in air at 20 °C in m/s and f is the wave frequency in Hz.
In this project, the simulations are run for frequencies ranging from 500 Hz to 1500 Hz. The largest cell size is calculated using the smallest wavelength, which is obtained for frequency 1500 Hz. Based on these calculations, the maximum cell size is set to 30 mm and the minimum cell size to 1.14 mm with a maximum element

growth rate of 1.3. Similar to the CFD mesh, the PML regions are meshed using quadrahedral cells while the rest of the domain is meshed with tetrahedral cells. 3 boundary layer cells are also added with a stretching factor of 1.2 to smoothly transition into the domain mesh cells. The meshed domain for acoustic study can be observed in Figure 4.10 and Figure 4.11.

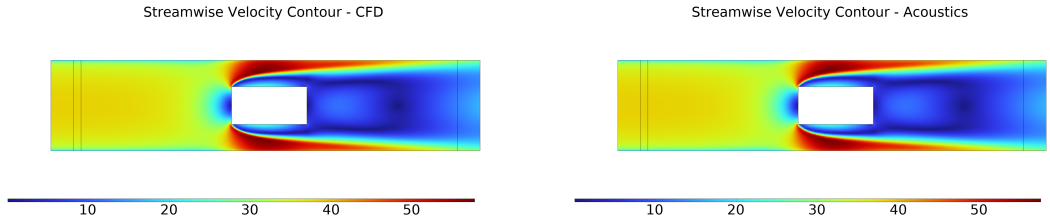

(a) Stream-wise Velocity contour from CFD simulation

(b) Stream-wise Velocity contour from background flow coupling

Figure 4.12: Mapping - Stream-wise velocity contour comparison

Figure 4.12 presents a comparison between the stream-wise velocity contours from the CFD simulation and those mapped to the acoustic mesh. It's crucial for both plots to be identical, as this confirms that the flow variables have been accurately transferred to the acoustic mesh, ensuring the reliability of the aero-acoustic simulations.

4.3.2 Acoustic Simulation

Once the mapping is successfully completed, the acoustic simulations can be initiated. For these simulations, certain regions need to be defined, as shown in Figure 4.7. As mentioned earlier, the PML (Perfectly Matched Layer) regions are positioned at both ends of the domain. Additionally, there is a sound source region with a width of 100 mm, whose main function is to generate a plane wave in the x-direction. The variables needed to define this plane wave are given in Table 4.2 and the description of the variables are mentioned in Table 4.3.

Name	Expression	Unit
K_0	$lnsf.\omega/(lnsf.c0 + U_{in})$	rad/m
p_b	$1e^{(-ik_0x)}$	Pa
u_b	$-1/(lnsf.i\omega * lnsf.\rho_0) * d(p_b,x)$	m/s
v_b	0	m/s
w_b	0	m/s
T_b	$lnsf.\alpha_p * lnsf.T_0/(lnsf.\rho_0 * lnsf.C_p) * p_b$	K

Table 4.2: Plane wave parameters

Name	Description
K_0	Convected wave number
p_b	Background acoustic pressure
u_b	Background acoustic x-velocity
v_b	Background acoustic y-velocity
w_b	Background acoustic z-velocity
T_b	Background acoustic temperature

Table 4.3: Description of plane wave variables

4.3.3 Boundary Condition - Acoustics

It is sufficient to provide the acoustic boundary conditions alone, as all other flow variables have previously been mapped. To make sure the plan wave is propagating in the x-direction, the background acoustic field condition is assigned to the source region using parameters derived from Table 4.2. The remainder of the domain is set as walls, and the symmetry plane from Figure 4.7 is used as the symmetry boundary condition. It should be noted that the impedance boundary, as seen in Figure 4.7, is only present when the simulation is conducted using an acoustic metamaterial. This boundary is also established as a wall boundary condition if the baseline simulation—that is, the simulation conducted without the use of metamaterial—is conducted.

It is challenging to import the actual metamaterial geometry into the computational domain mainly due to its small size and numerous holes with small diameter which would lead to increased computational time and meshing accuracy. To avoid such complications, an equivalent impedance is calculated for the metamaterial for each corresponding frequency and is imported into COMSOL to mimic the existence of a metamaterial in the impedance boundary. This ensures a close approximate behaviour of the metamaterial in the domain and its effect for each frequency value could also be observed. Linearized Navier-Stokes equation in a frequency domain model is used to run these acoustic simulations, as discussed in Chapter 2.

5
Results And Discussion

After several rounds of discussion and brainstorming, one came up with four feasible concepts for the metamaterials. The first one is the so-called double-layer micro-perforated panel (DLMPP)[19], which is a series connection of two MPPs followed by two cavities. It is tested to have broadband absorption, and its body can be placed inside the wall without disturbing the flow. The second one is a space-coiling structure based on Fano-like interference[25]. It has an inlet opening and an outlet opening so flow can go through it. The third one is the Segmented membrane sound absorber (SeMSA) which is studied to have a low-frequency broadband absorption in some IT fan applications[15]. However, considering the fragility of membranes and the high-pressure level caused by trucks' cooling fans, one should not put this plan into further study. The last one is a hybrid absorber of a shunt loudspeaker and perforated plates (HSLPP)[5]. It is a novel structure including both conventional perforated plates with a shout loudspeaker. The sound energy can be transferred into electronic current and thus be reduced. But the extra heat and other potential hazards stopped one from going deep.

This chapter describes the design development of a DLMPP cell and a space-coiling cell. Two simulations were then conducted using COMSOL, both employing the CFD-acoustics coupled method to investigate noise conditions with and without airflow. The space-coiling cell simulation incorporated an exhaust pipe positioned above it. The DLMPP cell was validated by applying its acoustic impedance in an under-cab environment.

5.1 Geometry

5.1.1 DLMPP

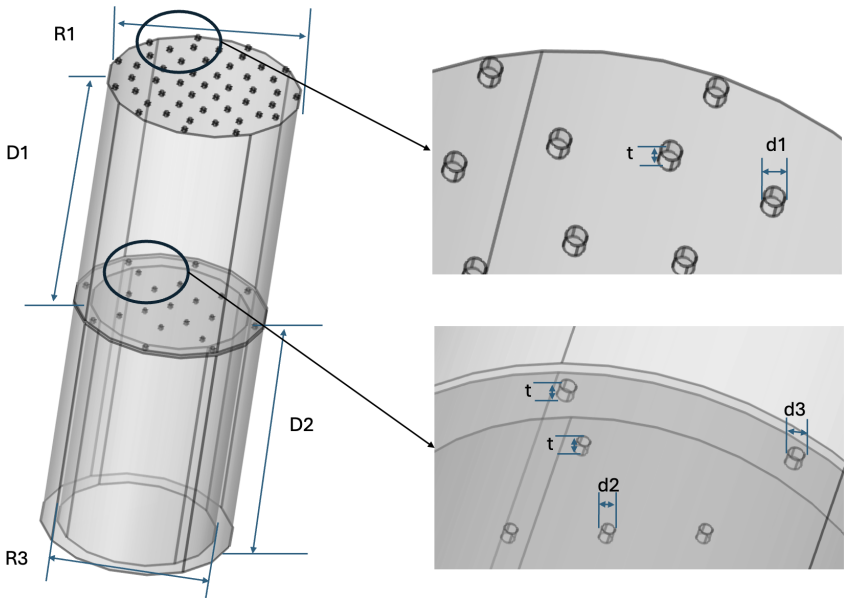

Figure 5.1: Geometry of DLMPP

This structure illustrated in Figure 5.1 is a sophisticated cylindrical system with two perforated layers, each having different hole diameters and open area percentages. Uniform perforations characterize the first layer, while the second layer is divided into a central region and a side annular region, each with unique perforation properties. This is done to make the absorption band even wider. The geometry parameters are defined as follows:

- R1: Radius of the upper section of the structure (associated with the first layer)
- R3: Radius of the centre area of the lower section of the second layer
- d1: Diameter of the holes in the first layer
- d2 and d3: Diameters of the holes in the two regions of the second layer (central and side cavities)
- D1: Depth of the cavity between the first and second layers
- D2: Depth of the cavity in the lower section following the second layer
- t: The thickness of the perforated layers. As the holes pass through the material of each layer, this is also the depth of the holes
- p1: The first layer has an open area percentage, representing the ratio of the perforated area to the total area in the first layer
- p2: An open area percentage of the centre region of the second layer
- p3: An open area percentage of the side circular region of the second layer

5.1.2 Space-Coiling Cell

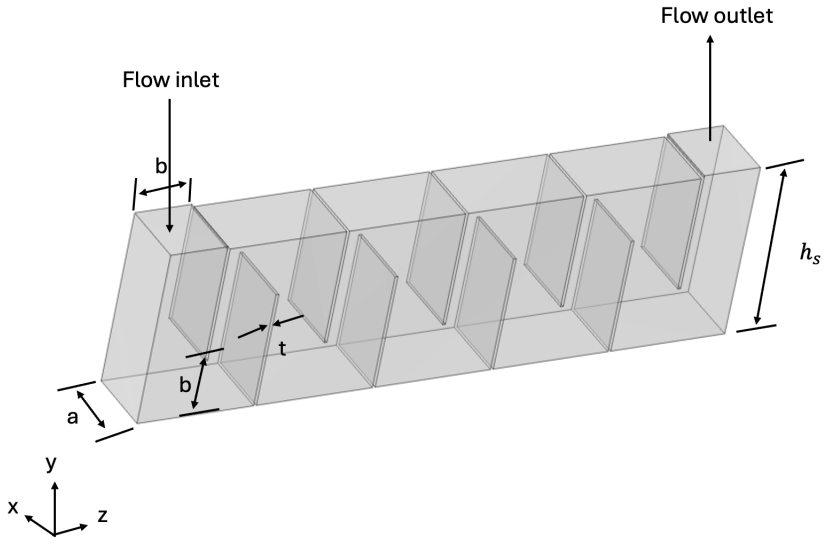

Figure 5.2: Geometry of space-coiling cell

The Space-coiling cell is a hollow structure consisting of an internal coiling or winding space that includes several parallel channels, as shown in Figure 5.2. Each channel is separated by a panel, ensuring the air or fluid flows through discrete pathways. Again, like DLMPP, the structure is designed to be embedded into a wall or a panel. It has two openings that serve as inlet and outlet according to the wind direction. These openings are aligned perpendicular to the wind or airflow direction. The geometry parameters are defined as follows:

- h_s: The vertical dimension of the entire structure
- a: The width of the entire structure (perpendicular to the flow direction)
- b: Each channel has an opening width and depth. It can either be the same for all channels or vary from one channel to another. In the case of varied channel openings, the widths can be represented as b_1,b_2,...,b_i (indicating unequal opening widths for different channels). Also, if b is smaller than half of h_S, then each channel path for flow can not be functional, instead the flow will just squeeze into a straight channel. So, a principle here is that b should at least be larger than half of the height h_s
- t: Thickness of all the panels

5.2 Theoretical Calculation

5.2.1 DLMPP

As mentioned in Chapter 2, MPP is based on air mass, air compliance and resistance. Now is high time to assemble the panels and cavities. Assuming the sound pressure p is from the normal direction of the DLMPP and $v1 - v4$ are the velocity at different

points. One can then form an EEC in Figure 5.4. A technique called the "Dot" method[17] is of use.

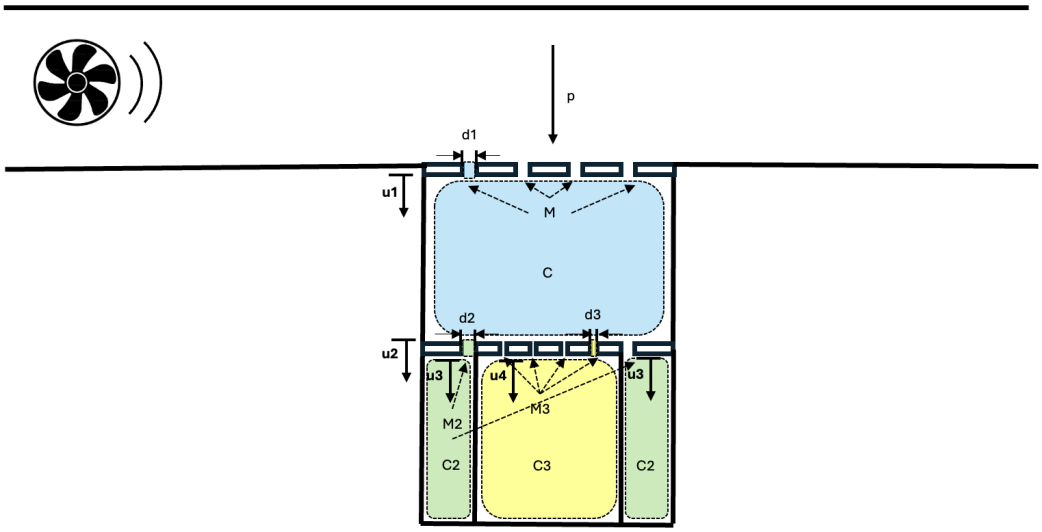

Figure 5.3: Schema of DLMPP. Assign mass M, M_2, M_3, compliance C, C_2, C_3 and resistance r, r_2, r_3 to the three "mass-spring" systems accordingly.

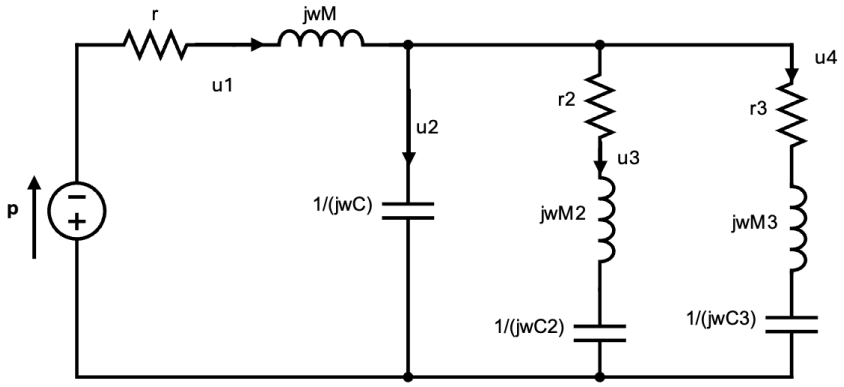

Figure 5.4: EEC of a DLMPP

By applying basis circuit principles for serials and parallel connections, the total impedance of the system, Z, can be calculated as:

$$Z = r + jwM + \frac{1}{jwC + (\frac{a_2}{r_2+jwM_2+jwC_2} + \frac{a_3}{r3+jwM_3+jwC_3})/(a_2+a_3)} \,. \tag{5.1}$$

With $a3$ as the area of the second layer's centre region and $a2$ as the area of the second layer's side circular region.

Consequently, the absorption coefficient reads:

$$\alpha = \frac{4 \cdot \mathrm{Re}(Z)}{(1 + \mathrm{Re}(Z))^2 + \mathrm{Im}(Z)^2} \,. \tag{5.2}$$

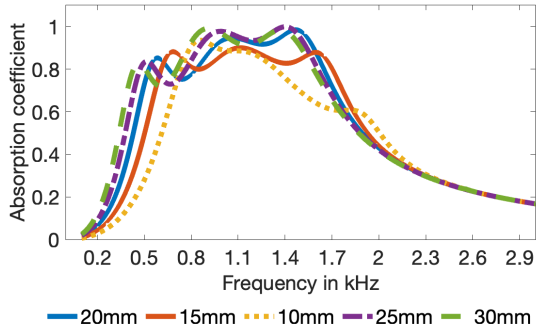

(a) D2

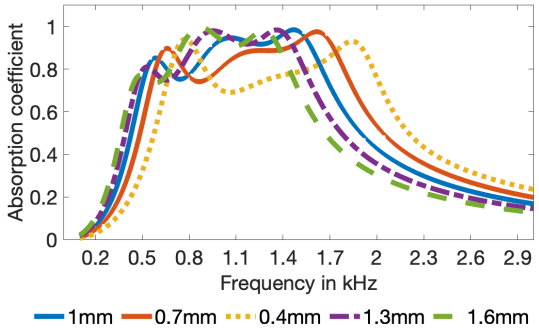

(b) t

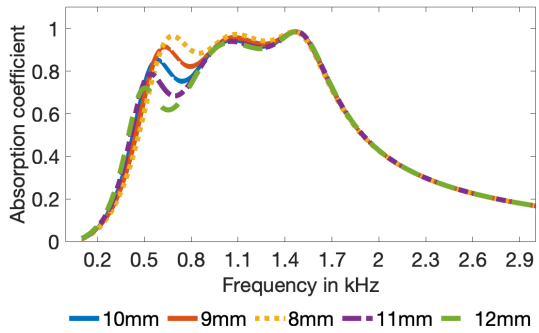

(c) R1

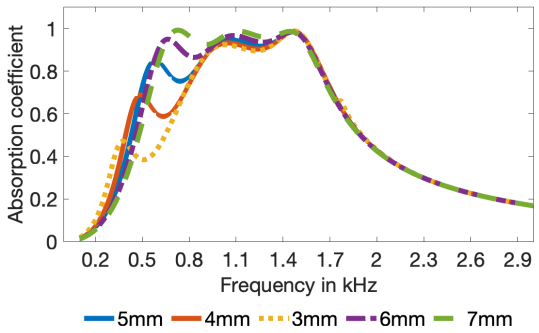

(d) R3

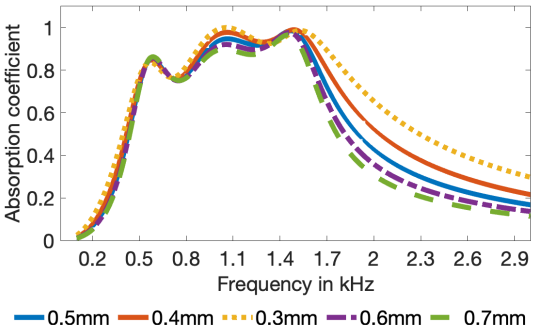

(e) d1

Figure 5.5: Parameter sweep with a baseline of: d1=0.5mm; d2=0.5mm; d3=0.5mm; R1=10mm; R3=5mm; t=1mm; p1=3%; p2=1%; p3=1%; D1=30mm; D2=20mm;

The next step is to find a set of optimized parameters. As the absorption band can

be relatively wide and such structures are normally valid at low and mid frequency, one's target is to reduce a broadband noise between 300 Hz to 2000 Hz, as discussed before in Chapter 3. Considering that 11 geometry parameters are involved in the design, one first conducts a parametric design by keeping other parameters constant and varying one parameter to a certain degree. Five parameters are shown in Figure 5.5 to give an idea of how the sweep works. All parameter sweeps can be found in Appendix B.
The result sensitivities are then presented in the following Table 5.1.

Parameter	**d1**	**D1**	**d2**	**D2**	**d3**	**p1**
Sensitivity	0.1280	0.3602	0.0962	0.4453	0.1656	0.4506
Baseline	0.5mm	30mm	0.5mm	20mm	0.5mm	0.03
Gradient	0.1mm	5mm	0.1mm	5mm	0.1mm	0.005

Parameter	**p2**	**p3**	**R1**	**R3**	**t**
Sensitivity	0.2145	0.2218	0.5033	0.4477	0.4193
Baseline	0.01	0.01	10mm	5mm	1mm
Gradient	0.005	0.005	1mm	1mm	0.3mm

Table 5.1: Sensitivity of all the parameters

Table 5.1 indicates that the most sensitive parameters here are thickness t, plate radius R1, R3, hole percentage p1, and cavity depth D2. Among those, R1 and R3 are interrelated because both of them describe the radius of the panel, and the ratio between both may largely influence the absorption frequency range. Finally, R3 together with t, D2, and p1 are chosen for the optimization. Of course, a more detailed analysis of this decision can be addressed in future studies.

By setting the target frequency band of 100 Hz to 3000 Hz[1], the optimized fitness value can be up to 0.6033 with the optimized parameters given in Table 5.2:

d1	**d2**	**d3**	**R1**	**R3**	**t**	**p1**	**p2**	**p3**	**D1**	**D2**
0.5mm	0.4mm	0.4mm	10	8.2mm	1mm	0.03	0.01	0.01	30mm	30mm

Table 5.2: Optimized parameters

The final absorption spectra are presented in Figure 5.6, illustrating the absorption performance of each individual layer as well as their combined effect. It is clear to see that the first layer holds a peak of 1200 Hz and the second has two around 600 Hz and 1200 Hz. As expected, each layer exhibits distinct absorption peaks due to each "mass-spring" system governing a critical frequency, resulting in resonance at specific frequencies. In contrast, the combined structure does not exhibit a prominent resonance peak. Instead, it delivers a remarkable absorption performance over

[1]Aim on a wider frequency range to get a better result. One can change that according to specific needs

a broad frequency range, spanning approximately 1300 Hz wide from 500 Hz to 1800 Hz.

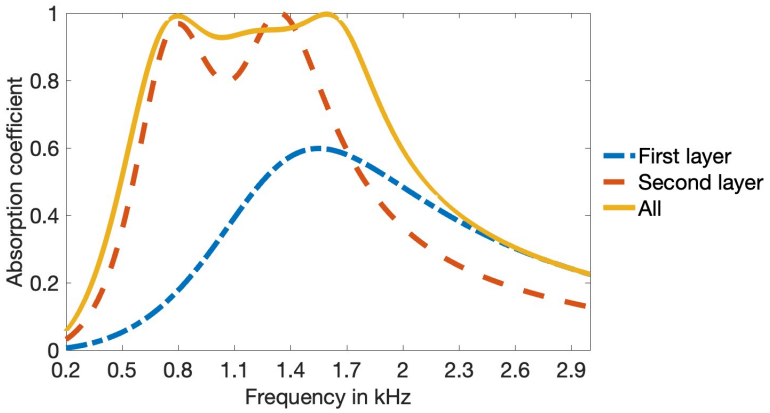

Figure 5.6: Absorption coefficient of the design DLMPP

5.2.2 Space-Coiling Cell

The acoustic pressure analysis is shown as the schematic diagram in Figure 5.7. The sound coming from the fan can be divided into the space-coiling as well as the ventilation channel. With the previous knowledge of Fano-like structure, acoustic impedance Z and equivalent wave number k in each channel are well known. Now one needs to investigate how wave interference is doing here.
In the schema, P_{fan} represents the acoustic pressure generated by the fan, P_{vin} refers to acoustic pressure at the entrance of the ventilation system, P_{sin} indicates the acoustic pressure at the start of the space-coiling structure. Similarly, P_{vout} means acoustic pressure at the end position of the ventilation, P_{sout} means acoustic pressure at the space-coiling structure outlet and P_{final} represents the pressure downstream. The symbols + and − denote the direction of the acoustic pressure, with + indicating downstream flow and − representing upstream flow. There is no need to discuss P_{final-} here as one assumes no boundary is downstream of the exhaust pipe.

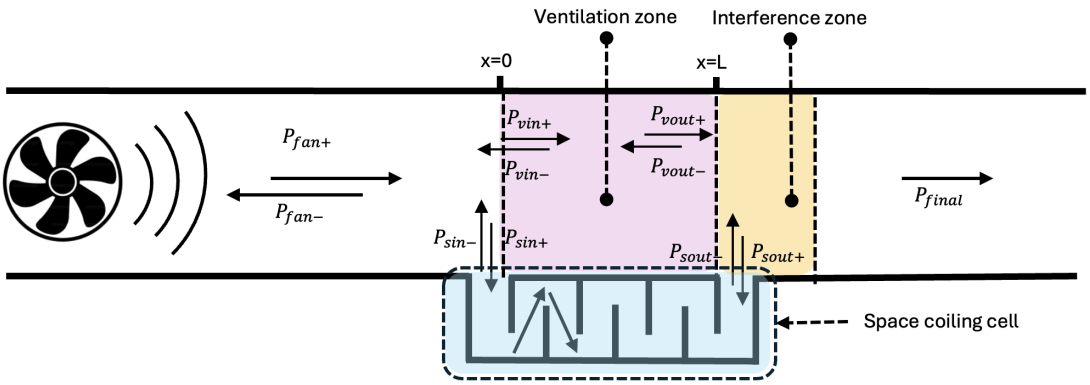

Figure 5.7: Schema of a space-coiling cell in an exhaust pipe

Within the space-coiling structure, the length and width of each subchannel can vary. An even opening coiling is an equivalent flat straight-channel model and an uneven one is like a stepped-channel model shown in Figure 5.8 [10]. Both situations are referred to as equal opening space-coiling cells and unequal opening space-coiling cells in the following description. Both studies have been conducted in this thesis. The impedance, equivalent wave number and effective length of the i^{th} subchannel inside the structure are denoted as Z_i, k_i and l_i. The former two values can be related to the length and width by equation 2.21. Effective length should be calculated as $l_i = \sqrt{(h_s - b_i)^2 + (b_i + t)^2}$. L is the length of the space-coiling cell.

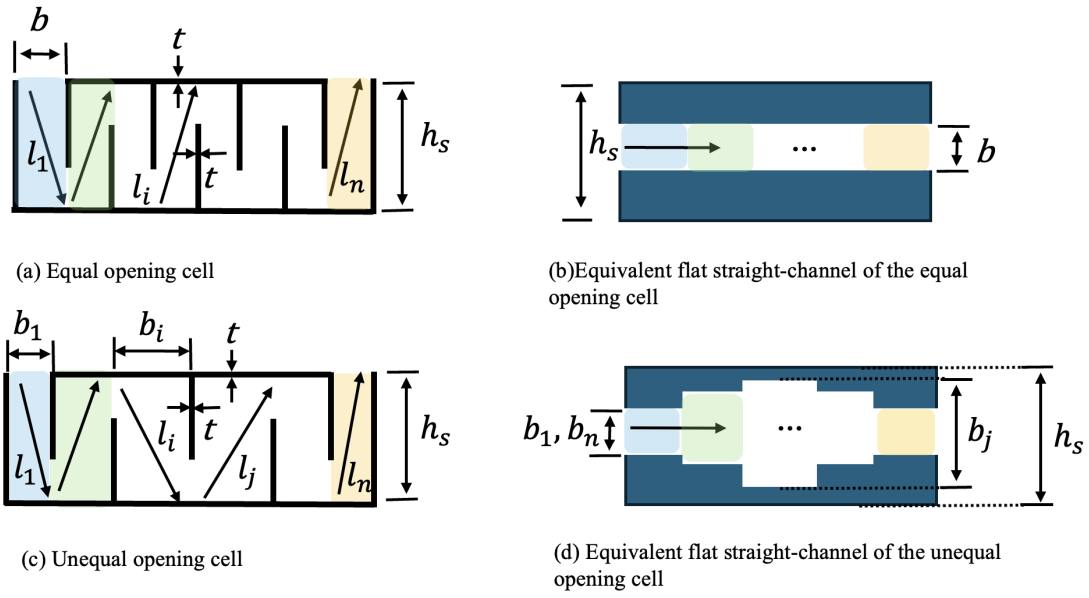

(a) Equal opening cell

(b)Equivalent flat straight-channel of the equal opening cell

(c) Unequal opening cell

(d) Equivalent flat straight-channel of the unequal opening cell

Figure 5.8: Schema of channel

Now, back to the sound field study of Figure 5.7. At position x=0, with air impedance $Z_{air} = \rho c$, the pressure and the velocity is described by:

$$P_{fan+} + P_{fan-} = P_{vin+} + P_{vin-} = P_{sin+} + P_{sin-} \tag{5.3}$$

$$\frac{S * P_{fan}}{Z_{air}} = \frac{P_{sin}}{Z_1} = \frac{S_v * P_{vin}}{Z_{air}} \tag{5.4}$$

S stands for the cross-section area of the exhaust pipe plus the opening area of the outlet, and S_v stands for the cross-section area of the ventilation channel.
At position x=L:

$$P_{vout+} + P_{vout-} = P_{sout+} + P_{sout-} = P_{final} \tag{5.5}$$

$$\frac{P_{sout}}{Z_n} = \frac{S_v * P_{vout}}{Z_{air}} = \frac{S * P_{final}}{Z_{air}} \tag{5.6}$$

Also, as the ventilation channel is a flat air channel, the propagation leads to $P_{vout+} = P_{vin+} * e^{-jk_{air}L}$ and $P_{vout-} = P_{vin-} * e^{jk_{air}L}$with wave number in air $k_{air} = 2\pi f/c$. The propagation of the space-coiling structure reads:

$$\begin{bmatrix} P_{sin} \\ v_{sin} \end{bmatrix} = \prod_{i=1}^{n} \begin{bmatrix} cos(k_i l_i) & jZ_i sin(k_i l_i) \\ jsin(k_i l_i)/Z_i & cos(k_i l_i) \end{bmatrix} \begin{bmatrix} P_{sout} \\ v_{sout} \end{bmatrix} = \begin{bmatrix} T_{11} & T_{12} \\ T_{21} & T_{22} \end{bmatrix} \begin{bmatrix} P_{sout} \\ v_{sout} \end{bmatrix} \tag{5.7}$$

With $\frac{P_{sin}}{v_{sin}} = Z_1$ and $\frac{P_{sout}}{v_{sout}} = Z_n$, Cause:

$$P_{sin} = (T_{11} + \frac{T_{12}}{Z_n}) P_{sout} \tag{5.8}$$

$$P_{sin} = Z_1 T_{21} P_{sout} + Z_1 T_{22} \frac{P_{sout}}{Z_n} \tag{5.9}$$

Taking equations 5.3, 5.4, 5.5, 5.6, 5.8 and 5.9 into account, one could form such matrix: .

$$\begin{bmatrix} 0 & 1 & 1 & \frac{T_{12}}{Z_n} - T_{11} & -\frac{T_{12}}{Z_n} - T_{11} & 0 & 0 & 0 \\ 0 & 1 & -1 & Z_1\left(T_{21} - \frac{T_{22}}{Z_n}\right) & Z_1\left(T_{21} + \frac{T_{22}}{Z_n}\right) & 0 & 0 & 0 \\ -1 & 1 & 1 & 0 & 0 & 0 & 0 & 0 \\ -1 & 0 & 0 & 0 & 0 & 1 & 1 & 0 \\ 1 & -\frac{Z_{air}}{Z_1 S} & \frac{Z_{air}}{Z_1 S} & 0 & 0 & -\frac{S_v}{S} & \frac{S_v}{S} & 0 \\ 0 & 0 & 0 & 1 & 1 & -e^{ik_{air}L} & -e^{-ik_{air}L} & 0 \\ 0 & 0 & 0 & 0 & 0 & e^{ik_{air}L} & e^{-ik_{air}L} & -1 \\ 0 & 0 & 0 & -\frac{1}{Z_n} & \frac{1}{Z_n} & -\frac{S_v}{Z_{air}} e^{ik_{air}L} & \frac{S_v}{Z_{air}} e^{-ik_{air}L} & -\frac{S}{Z_{air}} \end{bmatrix} \begin{bmatrix} P_{fan-} \\ P_{sin-} \\ P_{sin+} \\ P_{sout-} \\ P_{sout+} \\ P_{vin-} \\ P_{vin+} \\ P_{final} \end{bmatrix}$$
$$= \begin{bmatrix} 0 \\ 0 \\ P_{fan+} \\ P_{fan+} \\ P_{fan+} \\ 0 \\ 0 \\ 0 \end{bmatrix} \tag{5.10}$$

By setting the input pressure P_{fan+} as a constant number, one gets the pressure relatively to P_{fan+} at each position by equation 5.10. The absorption coefficient of the whole structure can be calculated as :

$$\alpha = 1 - |R|^2 = 1 - |\frac{P_{final}}{P_{fan+}}|^2 \tag{5.11}$$

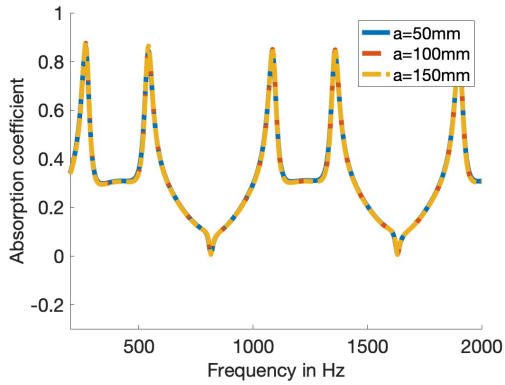

(a) a

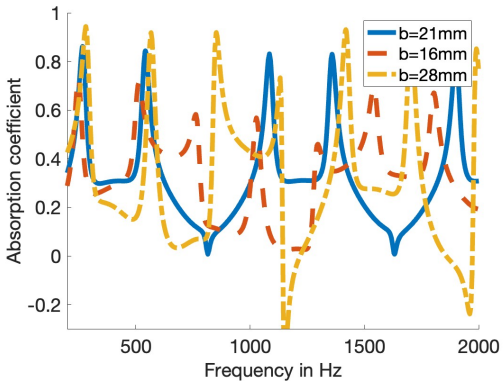

(b) b

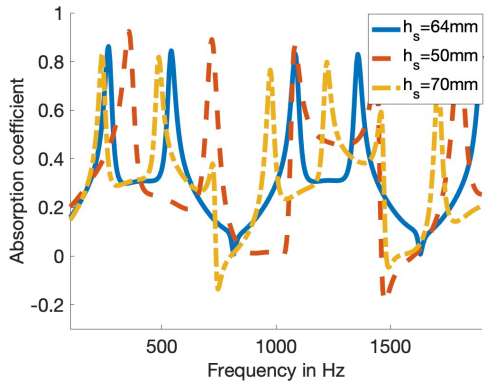

(c) h_s

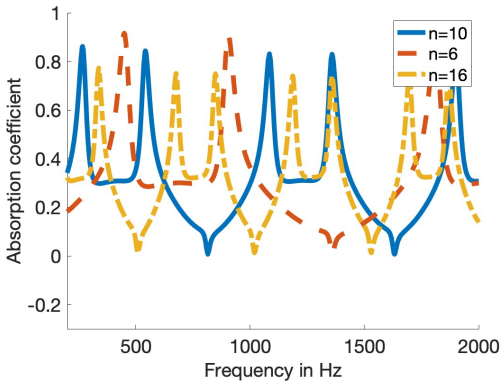

(d) n

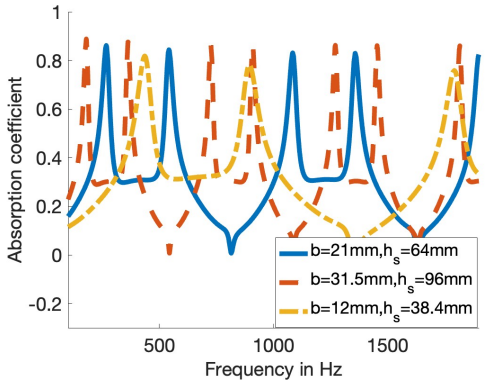

(e) keep $\frac{b}{h_s}$ the same

Figure 5.9: Parameter sweep with a baseline of: $a = 50mm$, $b = 21mm$, $h_s = 64mm$ and n=10

As the number of geometry parameters is relatively small, there is no need to conduct a parametric design to choose the most sensitive factor. At the same time, due to the limitations of the optimization algorithm, it's hard to find a solution for such a complex equation group. One decided to manually sweep the parameter to find the best overlap solution for the BPF and its harmonics. A quick parameter study is shown in Figure 5.9. Observations here are: Absorption at several harmonic frequencies can be negative. Better absorption at a specific frequency can result in

a	b	h_s	n
50mm	21mm	64mm	10

Table 5.3: Space-coiling cell parameters

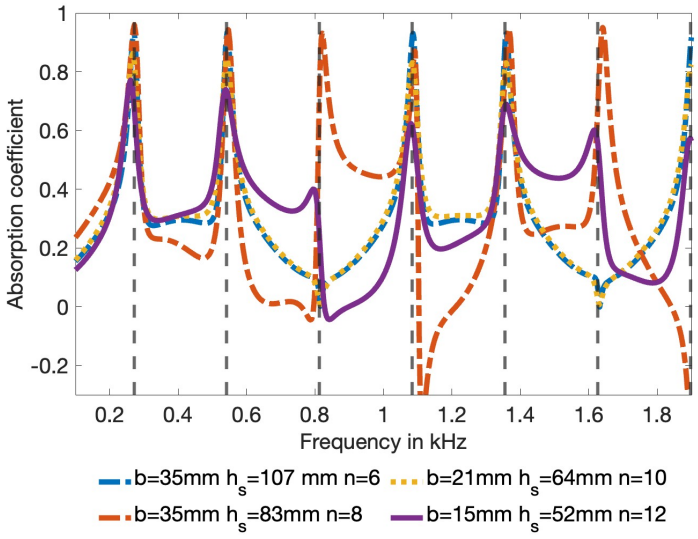

Figure 5.10: Absorption coefficient of the space-coiling cell

more prominent peaks. This leads to an increase in the amplitude of positive peaks, as well as a rise in the magnitude of negative peaks at other frequencies This means one must be careful dealing with those structures as at some frequency the structure can boost the noise. Parameter a has no effect on absorption at all. With the increment of h_s, the fundamental frequency shifted to a higher value. And b is in the opposite way. The fundamental frequency decreases as the channel number channel number n increases. This can lead to more peaks emerging in a certain frequency band. Keeping the ratio of $\frac{b}{h_s}$ the same, the fundamental frequency decreases with b and h_s.
Finally, four parameter sets of the equal-opening space-coiling cells targeted on the fan BPF are then shown in Figure 5.10. A suitable combination can be selected based on strict space constraints. The absorption peak is relatively narrow, spanning only around 50 Hz. It may be tightly sufficient for addressing the specific tonal characteristics of fan noise. A configuration with values in Table 5.3 was selected to conduct further simulation:

In a practical situation, the duty circle may change largely. This leads to a requirement for the robustness and high tolerance of the metamaterial. To broaden the absorption peak, a study of unequal openings was conducted. Following a method[39], a changed ratioCR value is set as a governing principle for the ratio of channel widths. Image a space-coiling cell with $2n$ channels. The width of the i^{th} channel, b_i $(1 < i < n)$, is dictated by the width of the entrance channel b_1 and the common

ratio factor CR, expressed as: $b_m = b_1 * CR^{1-i}$. For channels where $n < i < 2n$, the width b_m is expressed as $b_m = b_1 * CR^{i-2n}$. However, due to the geometric variation, this setting makes it difficult to establish a pattern where a fundamental frequency and its harmonics align as what one can perceive in Figure 5.11. As a result, the tonal noise generated by the fan cannot be effectively overlapped and reduced. There is no convincing evidence that creating wideband noise reduction is possible with an effective absorption behaviour. This has no advantage of an equal opening case. Without a doubt, further study can be done to investigate this phenomenon; the simulation in this thesis will only consider the equal opening case.

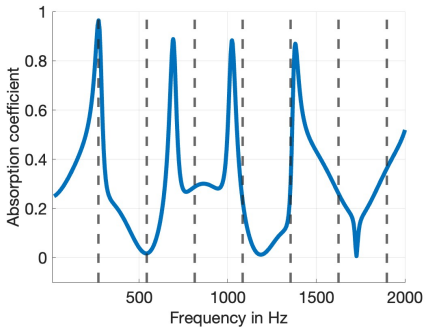

(a) a=50mm; b=15mm; h=40mm; n=6; CR=1.2

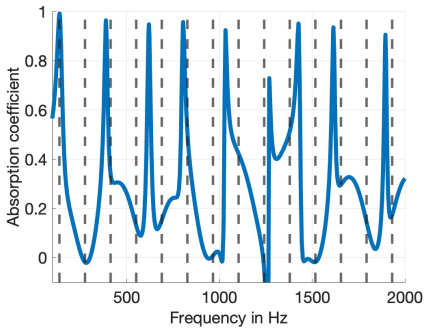

(b) a=50mm; b=30mm h=70mm; n=4; CR=1.5

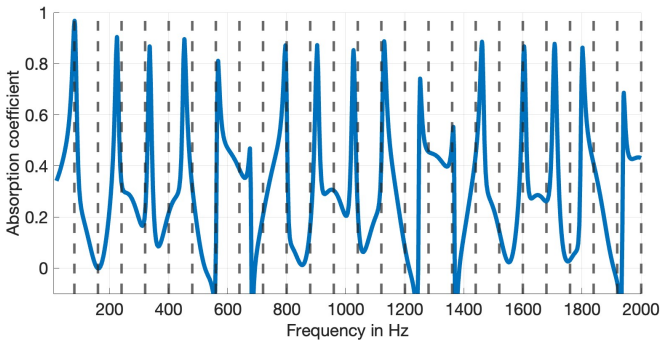

(c) a=50mm; b=30mm; h=40mm; n=8; CR=1.2

Figure 5.11: Absorption coefficient of unequal-opening space-coiling cell. Grey lines indicate the harmonics of the first peak.

5.3 Single Cell Simulation

To evaluate the performance of the metamaterial cell under flow conditions, simulations were conducted using an exhaust pipe model in *COMSOL 6.2.0.633*. As previously discussed, a cooling fan with a 60% duty cycle can generate a flow speed of approximately 20 m/s. Therefore, input Mach numbers of 0.06 and 0.1 were considered for the simulation. The computation was carried out on the Tetralith cluster[2] to ensure efficient processing and accurate results.

[2]Tetralith is NSC's(National Supercomputer Centre) largest HPC cluster. It replaced NSC's previous HPC cluster Triolith in 2018. Tetralith was funded by SNIC and used for research by

The exhaust pipe model, with a total length of 1.3 meters, a width and a depth of 0.06 meters, is designed for both flow and acoustic simulations. It is divided into multiple sections, including two PMLs at the inlet and outlet, each 0.1 meters long. These PMLs ensure smooth transitions for both the flow and acoustic fields, preventing reflections and boundary artefacts. The flow within the tunnel is set as fully developed, with Mach numbers of 0.06 and 0.1. This causes a turbulent flow with a Reynolds number of around 80k and 130k[3].

An acoustic background field is applied in the second block, allowing for the interaction of flow and acoustics. The sound source is set as a plane wave with an amplitude of 1 Pa. The central section, measuring 0.4 meters, houses a metamaterial cell and is finely meshed to capture detailed interactions between the flow and acoustics. The careful division of the tunnel, combined with the mesh refinement in critical areas, ensures accurate simulation results for both the flow and acoustic fields.

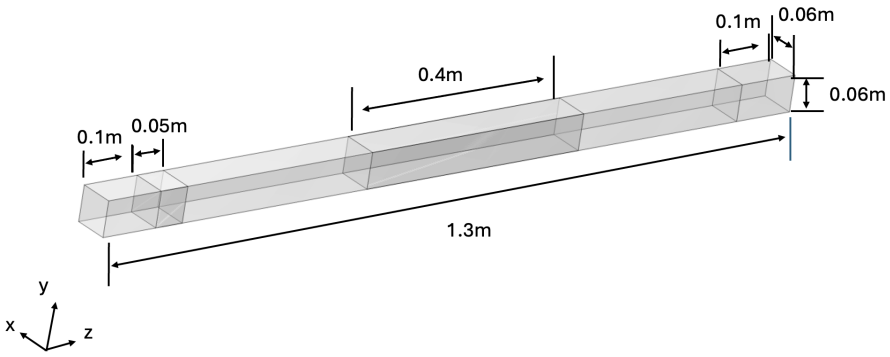

Figure 5.12: Exhaust pipe

5.3.1 Mesh

First of all, because both metamaterials are symmetric, a symmetry model was built in COMSOL to reduce computational cost. In general, the mesh was created using a combination of quad, tetrahedral, and swept meshes. Different parts of the domain were meshed using appropriate methods to ensure high accuracy and efficiency. Quad elements were applied to specific boundaries (inlet, outlet, and some parts of the walls), while swept meshing was used for simpler geometries, such as the exhaust pipe. Tetrahedral meshing techniques were employed to handle more complex geometries within the domains. The corner refinement technique was applied to the walls of the resonator to ensure that sharp corners were adequately resolved. The customized size control allowed flexibility in setting different element sizes based on the geometric complexity of various boundaries and domains. An

Swedish research groups. https://www.nsc.liu.se/systems/tetralith/

[3]Reynolds number = $\frac{\rho u L}{\mu}$, with air density ρ, air velocity u, the width of exhaust pipe L and air viscosity μ

eight-layer boundary mesh was applied to both cells to capture the flow close to the wall.
For the acoustics mesh, onto which the CFD solution was mapped, the mesh was relatively coarse. At the walls, the acoustic boundary layer was not resolved due to the use of slip conditions. One or two boundary layer mesh elements were sufficient to resolve the background flow profile near the wall. Using a Free Tetrahedral mesh in critical domains, along with additional refinement at the resonator's opening, allowed for high accuracy in both large-scale wave propagation and near-boundary effects. The use of Swept meshes and carefully controlled element sizes contributed to an efficient and accurate mesh that balanced computational resources with the need for detailed acoustic resolution.
For the space-coiling structure, there were 1.02 million mesh elements used in the CFD study and 0.21 million elements used in the acoustic study. Notably, the first layer of the boundary mesh was set to 1/10 of the local domain element height to achieve a suitable y+ value for calculations.

(a) CFD mesh **(b)** Acoustic mesh

Figure 5.13: Mesh of the space-coiling cell

(a) CFD mesh **(b)** Acoustic mesh

Figure 5.14: Mesh of the exhaust pipe and space-coiling cell

5.3.2 Space-Coiling Cell

5.3.2.1 CFD

As one can observe the turbulence velocity from Figure 5.15, despite these complex interactions, the overall flow velocity in the exhaust pipe appears steady. The flow velocity in the exhaust pipe even increases by about 0.5 m/s with the presence of the space-coiling cell. Meanwhile, the flow speed in the space-coiling cell is relatively

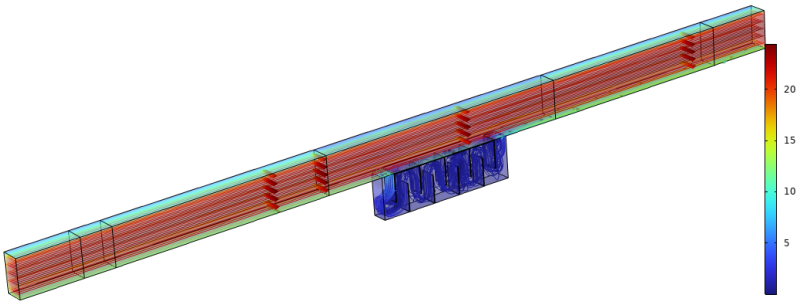

(a) Turbulence velocity Ma=0.06

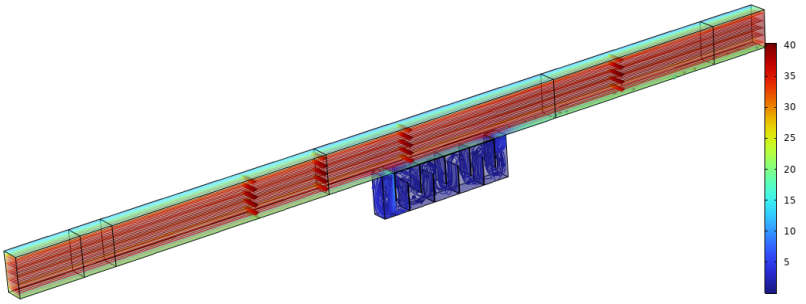

(b) Turbulence velocity Ma=0.1

Figure 5.15: Turbulence velocity

low down to less than 5m/s. This highlights the metamaterial's effective design, which seems to maintain a consistent velocity profile.

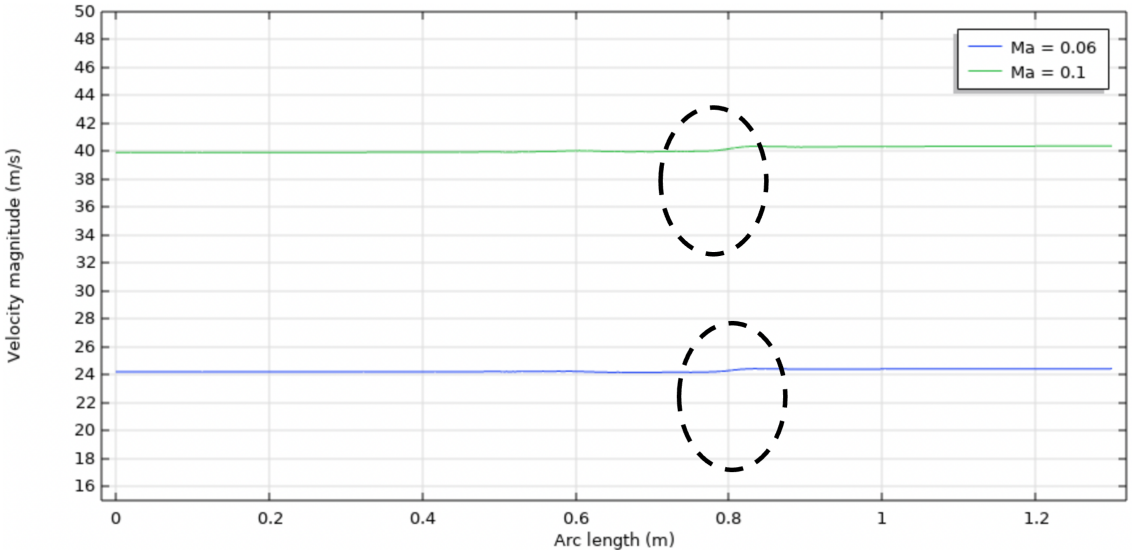

Figure 5.16: Flow velocity along Z axis

The flow streamlines in the space-coiling cell, depicted in Figure 5.17, illustrate swirling and recirculation patterns, indicative of the complex flow dynamics within the metamaterial cells. The fluid behaviour is altered by the presence of the metama-

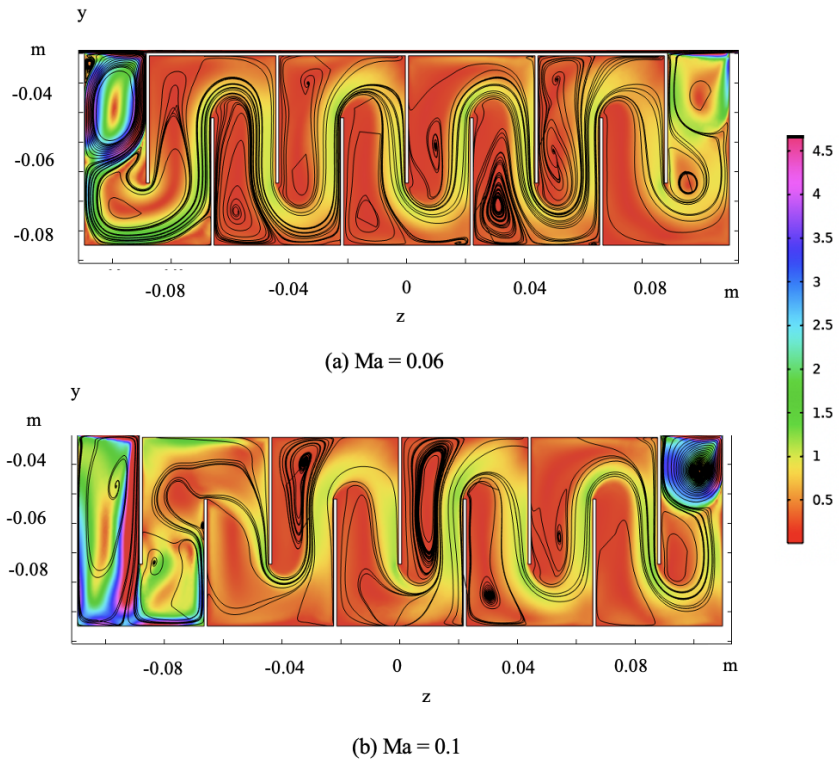

Figure 5.17: Turbulence velocity in m/s and flow stream inside the space-coiling cell

terial structure which is characterized by sharp turns and interactions with internal panels in this area. The swirling arrows represent vortices, where the fluid circulates in small loops, creating recirculation zones at the cavities above the inlet and outlet opening. It is also worth mentioning that the aspect ratio of those cavities is 0.32, which should lead to three vortices of similar size and shape arranged vertically inside the cavity[11]. Only one is observed here due to the opening at the lower part. Recirculations should be treated carefully as they may create additional noise. As the flow enters the metamaterial cells, it experiences dramatic changes in direction and speed, resulting in a highly dynamic flow field.

5.3.2.2 Sound Absorption

The comparison of the absorption coefficient between the flow simulation, no-flow simulation, and theoretical calculation over the frequency range of 200-700 Hz is shown in Figure 5.18. By comparing the no-flow case with the theoretical results, it is evident that the general profiles align well. Although there is a slight shift in the peak of the simulation case—from 270 Hz in the theoretical model to around 330 Hz in the simulation—it still demonstrates a promising absorption coefficient of 0.5 at the target frequency. Similarly, for the next harmonic peak, the simulation shows an absorption coefficient of 0.8 at the expected harmonic frequency.

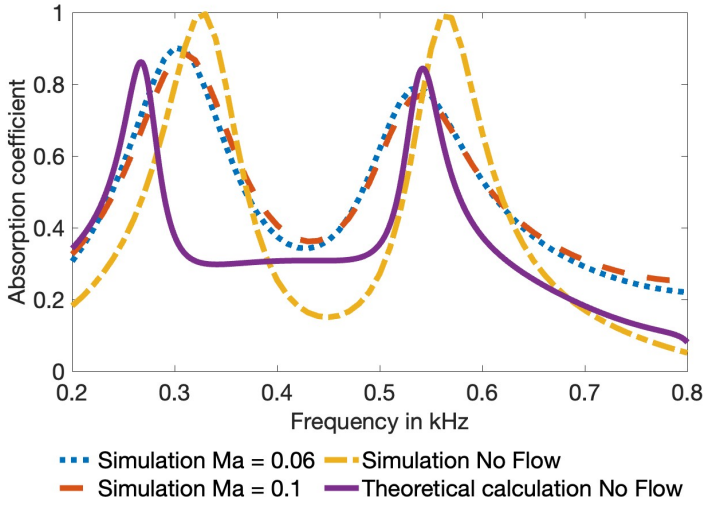

Figure 5.18: Comparison absorption coefficient between flow simulation, no flow simulation and theoretical calculation

Furthermore, the two flow simulation cases (Ma = 0.06 and Ma = 0.1) exhibit excellent agreement with each other, indicating that the variation in flow speed does not significantly affect sound absorption. This consistency in peak profiles provides strong evidence that the metamaterial design can effectively manage tonal noise in scenarios like cooling fan noise, making it a promising solution for such applications.

Another interesting phenomenon to highlight is that, in theoretical calculations, Fano-like interferences often result in negative absorption at a certain frequency. However, in the simulations without flow, these negative effects disappear, as shown in Figure 5.19. In cases involving flow, absorption increases further. This is likely due to reflections in the 3D space. This provides more insights into the practicality of this structure.

The sound pressure levels at 271 Hz and 542 Hz are presented in Figures 1 and 2. The flow does not significantly affect the sound pressure level. However, the presence of airflow elongates the distance between the nodes and antinodes, which corresponds to a change in the wavelength. This explains why the fundamental absorption frequencies under flow conditions are always lower than those observed in the absence of flow. A wave-like pattern observed in the figures suggests the presence of standing waves in the exhaust pipe due to reflections. This occurs because the length of the tunnel exceeds half the wavelength for both frequencies, causing interference between the incident and reflected waves travelling in opposite directions. Additionally, it is worth mentioning that within the metamaterial structure itself, a similar node-antinode pattern can be observed, indicating the presence of standing waves inside the metamaterial as well. This further confirms that the space-coiling structure can be treated as an equivalent straight channel.

At the lower frequency of 271 Hz, there is a noticeable reduction in sound pressure

after the first node. A significant noise reduction is also evident at the higher frequency of 542 Hz. The sound level decreases immediately after the metamaterial cell's outlet due to destructive interference, which also disrupts the standing wave interference downstream. As a result, the standing wave pattern vanishes, leaving an approximate 10 dB noise reduction in the downstream region in all the cases shown in Figure 5.20 and Figure 5.21. Upon closer observation, it can be seen that, under all flow conditions, the nodes and antinodes shift slightly downstream compared to the case without flow. This suggests that the same wavelength corresponds to a lower frequency in these conditions, which likely explains the shift of the absorption peaks to lower frequencies, as shown in Figure 5.18.

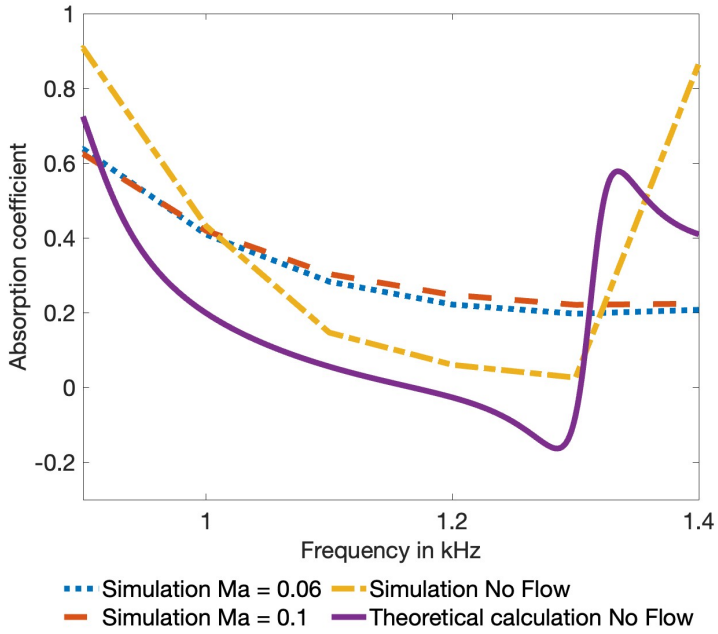

Figure 5.19: Comparison absorption coefficient between flow simulation, no flow simulation and theoretical calculation. With settings of: a=50mm, b=15mm, h_s=40mm

Finally, by taking slices at the outlet position on the XY and XZ planes, the SPL grid patterns reveal the potential interference between the sound waves travelling inside the exhaust pipe and the spatial coiling structure. This is shown in Figure 5.22.

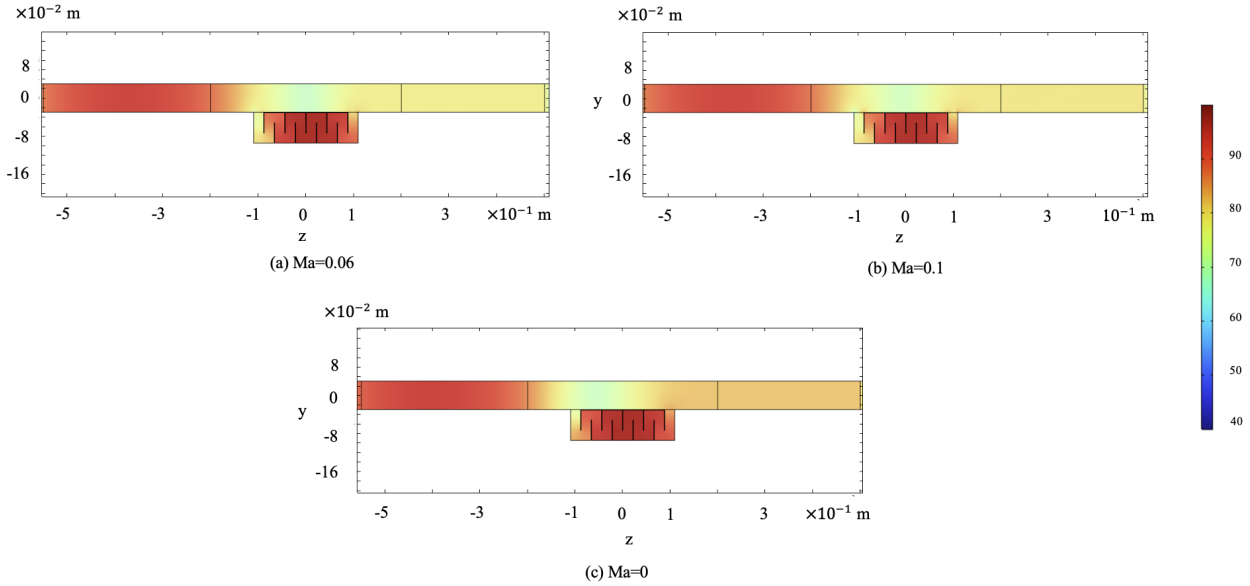

Figure 5.20: SPL in dB, f = 271 Hz

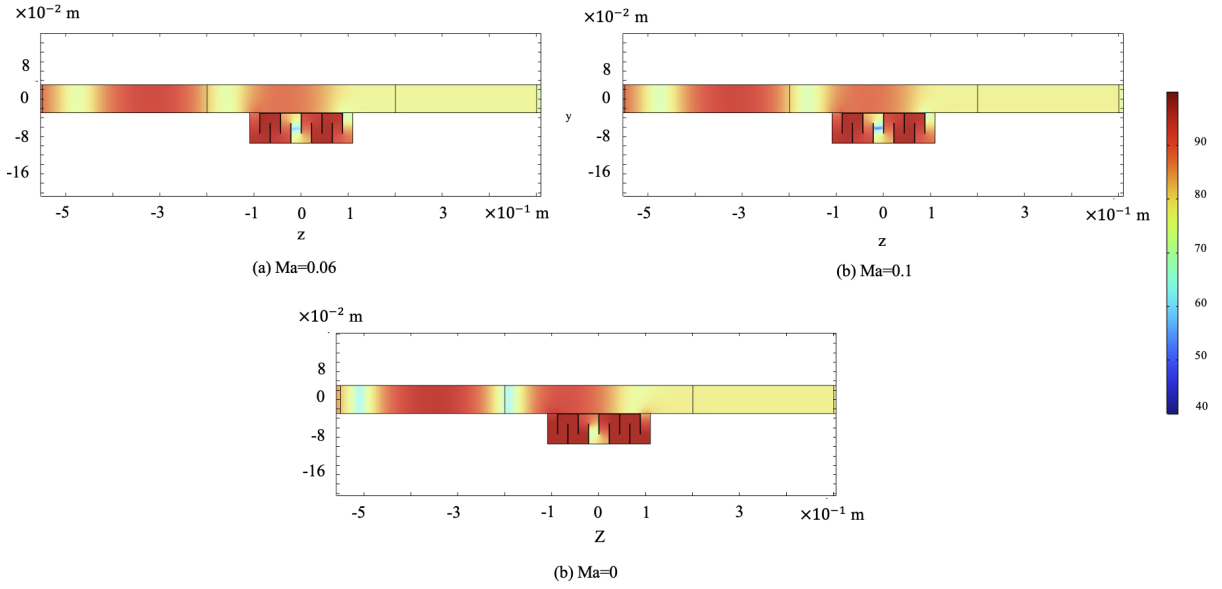

Figure 5.21: SPL in dB, f = 542 Hz

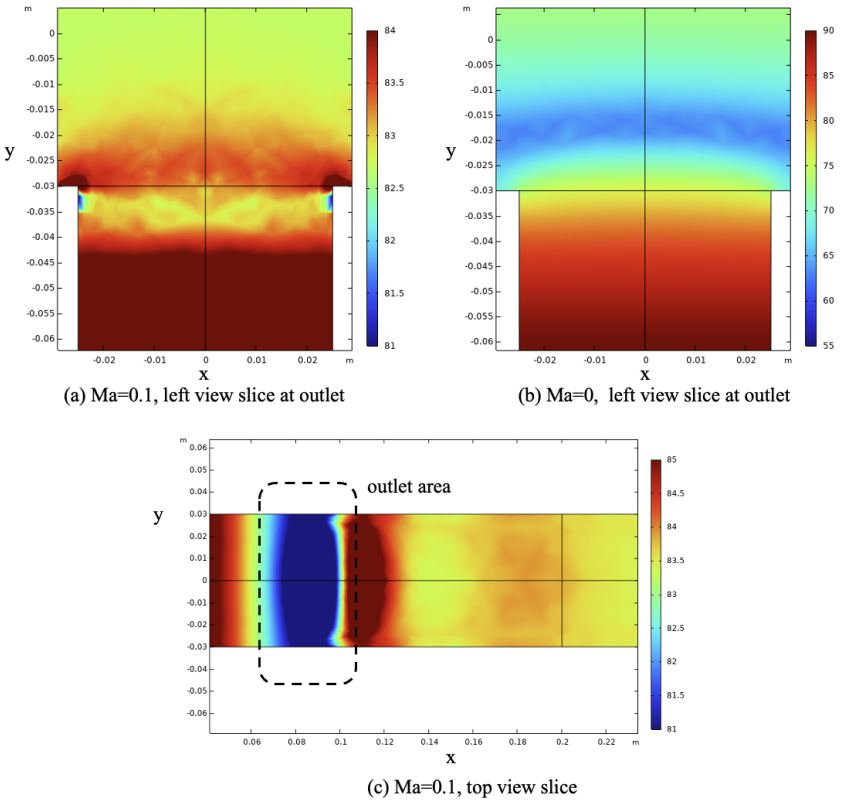

Figure 5.22: SPL outlet slice in dB, f=330 Hz

5.4 Flow Analysis in under-cab Environment

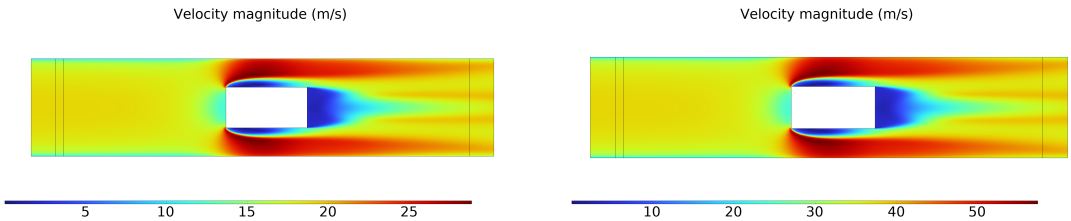

(a) Mach 0.05 **(b)** Mach 0.1

Figure 5.23: Flow contour along x-direction

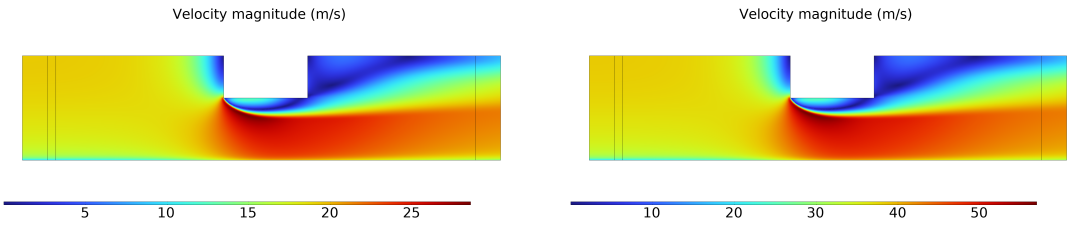

(a) Mach 0.05 **(b)** Mach 0.1

Figure 5.24: Flow contour along y-direction

In the Mach 0.1 velocity contour plot, as observed in Figure 5.23b and Figure 5.24b, the flow accelerates about the component box due to the reduced effective area of flow thereby creating an area of higher velocity after the obstacle. Again this complies with Bernoulli's principle where increased velocity is matched with a consequent reduction in pressure at the areas of flow acceleration. The largest velocities, colored red, are found mostly at the top and bottom boundaries of the simulation domain and directly downstream from the barrier. There is also evidence of flow separation, which creates a wake behind the obstacle with a significant velocity deficit. This wake can energize vortex shedding and possibly turbulence; both effects are now known to increase noise levels. The wake immediately behind the obstacle is typically blue - indicating a significant velocity drop, hence a low-pressure wake, which can be a source of noise if unsteady.

The upstream section has a uniform profile of velocity, experiencing no significant effects from the flow prior to the encounter with the box. The velocity was essentially uniform up to the inlet, and hence it was stable, laminar flow before interaction.

In Figure 5.23a and 5.24a, within the Mach 0.05 velocity profile, one observes an overall trend similar to that achieved in the case of Mach 0.1, but all the values of velocity in the whole field are apparently diminished according to intuition, and their reduced flow velocity. The maxima are once more in the peripheries of the box, but these values are lower than for the Mach 0.1 case with peaks of approximately 25 m/s. As expected the wake behind the obstacle is significant, and this reattains free-stream velocity at a slower rate than in the Mach 0.1 case. Flow separation remains but is now much less severe, perhaps indicating a decrease in the strength of vortex shedding and turbulence.

The upstream region once again shows a steady velocity profile, similar to the Mach 0.1 case but with slightly lower magnitudes. The difference between the two profiles primarily lies in the extent and severity of the wake region behind the obstruction. In the Mach 0.05 case, the wake is larger and more diffuse, which suggests that the lower flow velocity allows for a more gradual recovery to free-stream conditions. This lower speed flow might also lead to reduced aeroacoustic noise, as there is less energy in the system to generate turbulence and flow instabilities downstream.

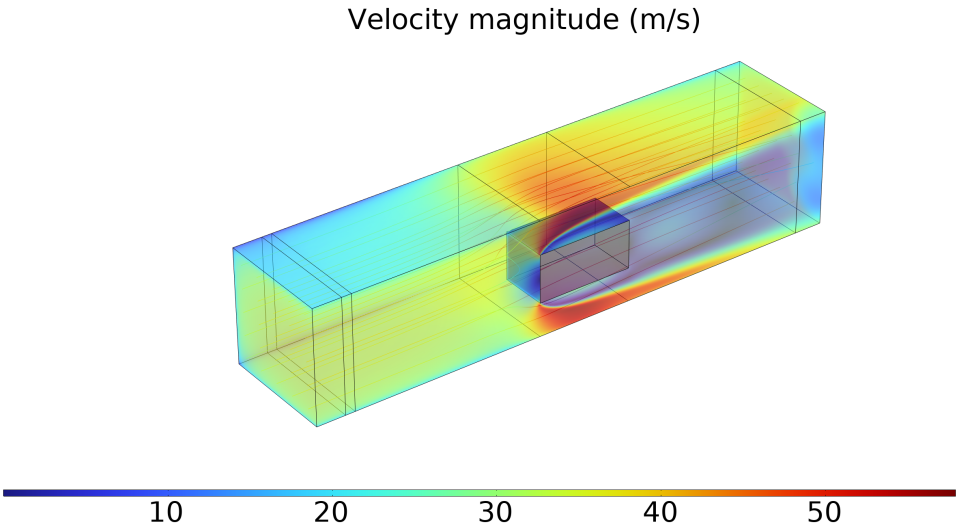

Figure 5.25: 3D flow contour for Ma = 0.1

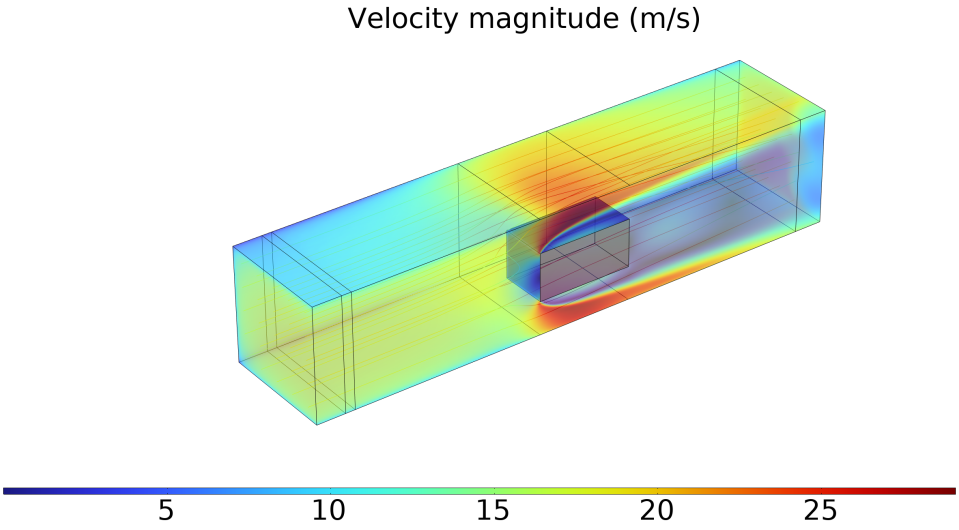

Figure 5.26: 3D flow contour for Ma = 0.05

5.5 Simulation Without Acoustic Metamaterials

In this section, the sound pressure levels (SPL) at the three chosen frequencies of 500 Hz, 1000 Hz, and 1500 Hz, with respect to the two airflow conditions, Mach 0.1 and Mach 0.05, are examined. The emphasis is on the propagation of sound in the x-axis and y-axis and the effect of changing the speed of airflow on the intensity and pattern of the noise. These simulations are performed without any acoustic metamaterials (AMMs), therefore, they help to see how sound is propagating at higher frequencies and with different airflow.

5.5.1 500 Hz

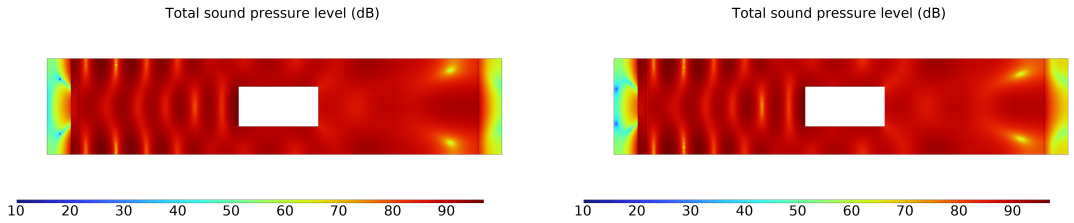

(a) Mach 0.05 **(b)** Mach 0.1

Figure 5.27: SPL contour along x-direction

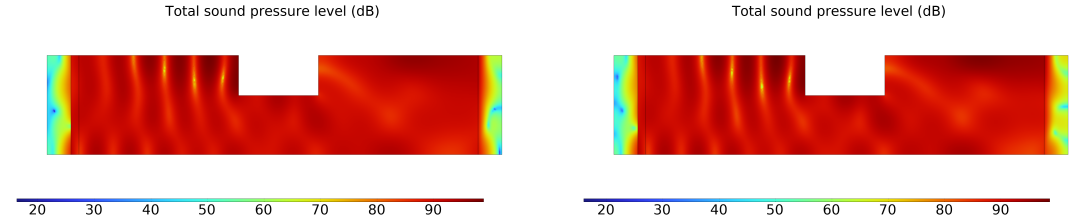

(a) Mach 0.05 **(b)** Mach 0.1

Figure 5.28: SPL contour along y-direction

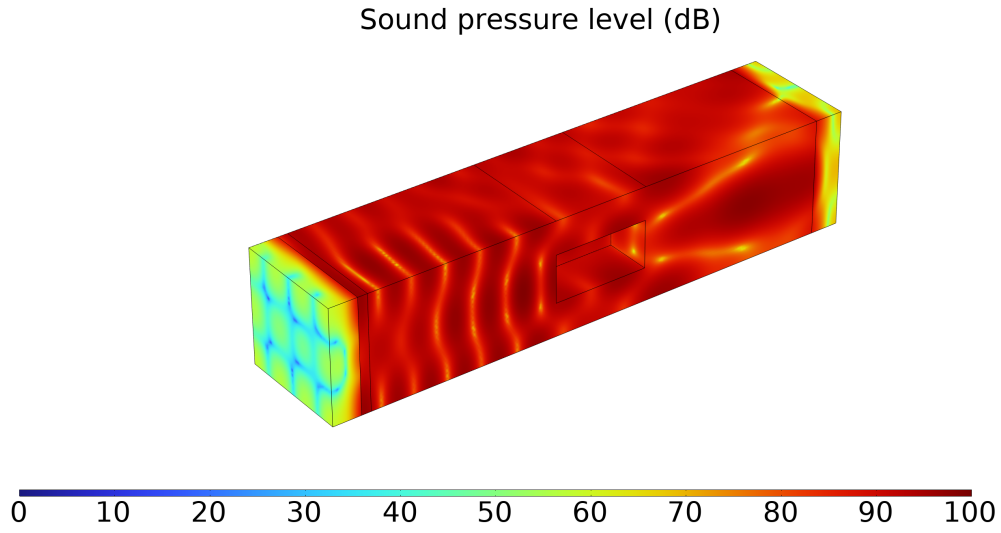

Figure 5.29: 3D SPL contour for Ma = 0.1 at 500 Hz

In the Mach 0.1 case (Figure 5.27b), sound pressure levels (SPL) stay consistently high, especially in the middle and downstream regions, with values between 80-90 dB. One can clearly see standing wave patterns, particularly around the component box. These patterns are caused by sound waves reflecting off boundaries, overlapping, and amplifying each other. While there are some lower SPL areas (around 20-30 dB) near the sound source, they don't extend very far. The higher airflow

speed pushes the sound energy downstream faster, so the sound doesn't naturally dissipate as much as it travels through the domain.
Looking at the y-axis case (Figure 5.28b), one again sees high SPL values (80-90 dB), especially in the central and downstream parts. The standing waves show up as vertical bands of high pressure across the domain. These patterns happen due to strong reflections between the ceiling, floor, and walls, along with the fast airflow pushing the sound downward. In the upstream region, there are small pockets of lower SPL (20-30 dB), but they're limited to the area near the source. Overall, the faster airflow increases sound energy, leading to more significant noise buildup, especially along the vertical axis.

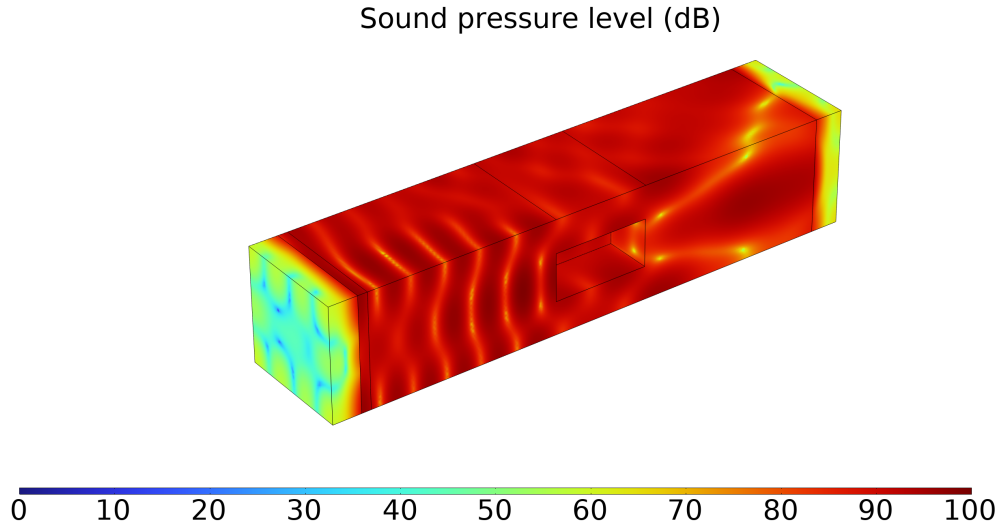

Figure 5.30: 3D SPL contour for Ma = 0.05 at 500 Hz

In the Mach 0.05 simulation (Figure 5.27a), the overall sound pressure distribution is similar, but the high-SPL zones are more spread out. Although the downstream region still shows SPL values between 80-90 dB, there are larger low-SPL areas near the sound source and upstream. The standing wave patterns aren't as intense as in the Mach 0.1 case, meaning the slower airflow results in weaker reflections and less interference. This allows for a bit more natural sound attenuation as the sound moves through the domain, although the noise levels downstream are still high.
The y-axis plot for Mach 0.05 (Figure 5.28a) shows similar patterns to Mach 0.1 but with less intense standing waves. The slower airflow leads to better sound dissipation, creating larger areas of low SPL, especially upstream. The vertical bands of high SPL are still present but more spaced out compared to Mach 0.1. This suggests that the slower flow allows sound energy to spread more evenly, reducing the intensity of standing waves and making the SPL distribution smoother.
It's worth noting that the SPL is consistently very low in the Perfectly Matched Layer (PML) region across all the simulation results. This happens because the PML boundary condition is designed to act like an open space, allowing sound waves to exit the simulation area without bouncing back into the main domain. Essentially, the PML serves as a buffer zone that absorbs sound waves, preventing them from interfering with the actual region one cares about. The low SPL in this

area is exactly what one expects, as the PML is specifically designed to absorb and dissipate wave energy, keeping the sound field in the main simulation free from unwanted reflections.

5.5.2 1000 Hz

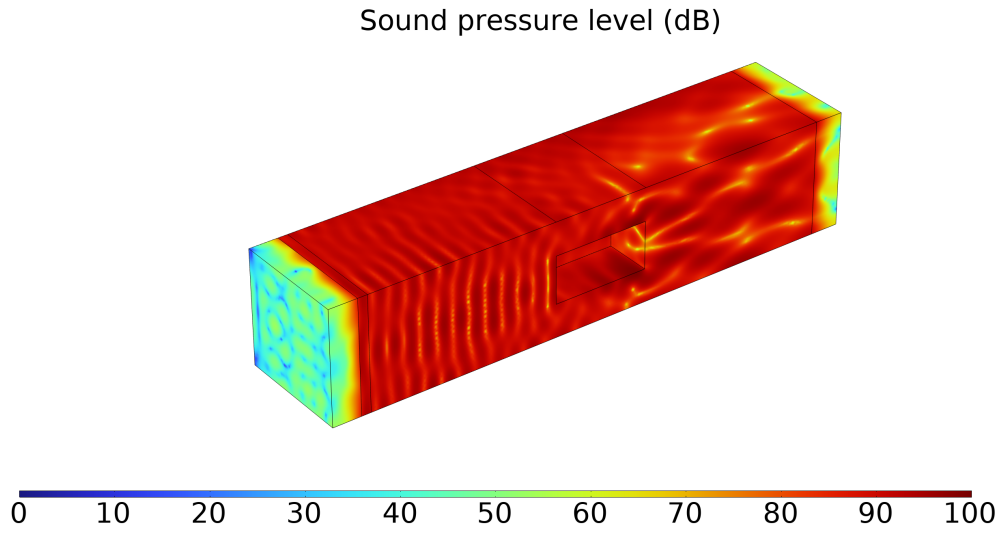

Figure 5.31: 3D SPL contour for Ma = 0.1 at 1000 Hz

In the Mach 0.1 scenario, SPL remains notably high across the domain, with levels between 80-90 dB dominating the central and downstream regions, as seen in Figure 5.33b. At 1000 Hz, the shorter wavelength (can be visually seen in Figure 5.40)results in more compact standing wave formations, particularly around the component box in the middle of the domain. These waves arise from constructive interference, where overlapping sound waves combine to increase pressure in certain spots. We can also observe a region of slightly lower SPL levels downstream, which could be attributed to the flow-acoustic interaction which becomes more prominent as the frequency increases. While some lower-SPL regions (20-30 dB) exist near the sound source, they are mostly confined to the upstream area. The fast airflow quickly pushes sound downstream, leaving little room for dissipation, causing noise to accumulate as sound waves reflect and interfere.

In the vertical plane, evident from Figure 5.34b, the contour continues to exhibit high SPL values, particularly downstream where levels also reach 80-90 dB. The tightly packed standing wave bands, running from floor to ceiling, are more frequent due to the shorter wavelength at 1000 Hz. This causes sound to reflect more often between surfaces, leading to increased interference. While low-SPL zones can be found near the source, they are limited, as the higher airflow prevents significant dissipation of sound energy. This ultimately results in greater noise concentration in the downstream and central areas.

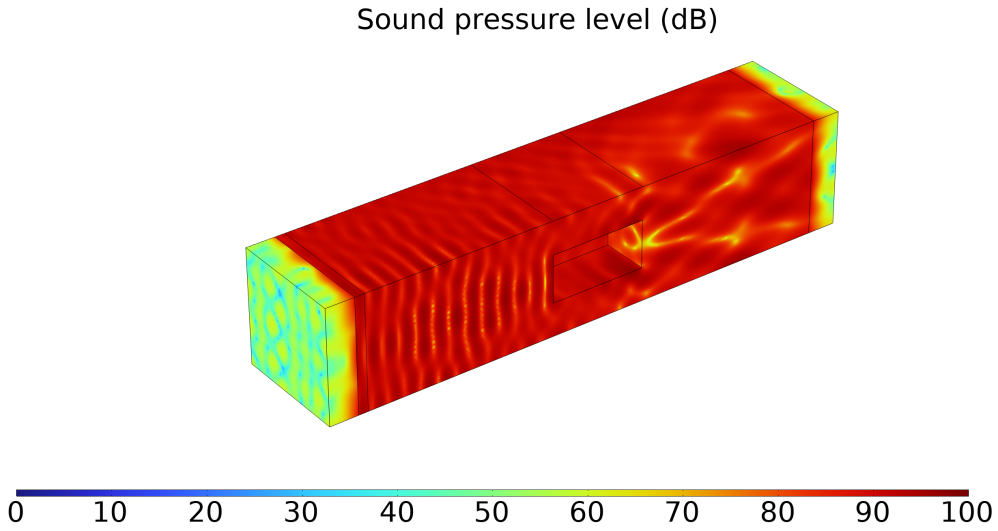

Figure 5.32: 3D SPL contour for Ma = 0.05 at 1000 Hz

On the other hand, the Mach 0.05 case reveals a slightly different picture, with a more balanced distribution of sound pressure, as observed from Figure 5.33a. Although SPL values downstream still range from 80-90 dB, the standing wave patterns are less densely packed, and the low-SPL zones near the sound source are larger. The slower airflow allows sound to dissipate more effectively, leading to weaker reflections and reduced interference. While high noise levels persist downstream due to ongoing reflections and interference, the sound energy spreads out more uniformly across the domain.

Along the vertical axis in the Mach 0.05 simulation, from Figure 5.34a, the SPL distribution is more even, with larger low-SPL areas upstream. The standing waves are still present but less compact compared to the Mach 0.1 case. The reduced airflow speed facilitates better sound energy dissipation, lowering the intensity of interference. Although the downstream region still experiences high SPL values, the interference patterns are more dispersed, resulting in a smoother distribution of sound pressure throughout the domain.

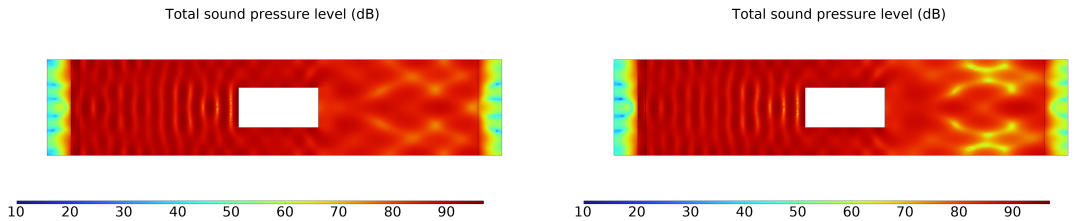

(a) Mach 0.05 **(b)** Mach 0.1

Figure 5.33: SPL contour along x-direction

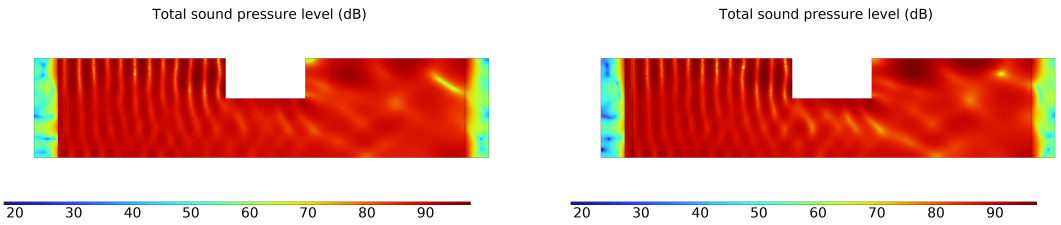

(a) Mach 0.05 **(b)** Mach 0.1

Figure 5.34: SPL contour along y-direction

5.5.3 1500 Hz

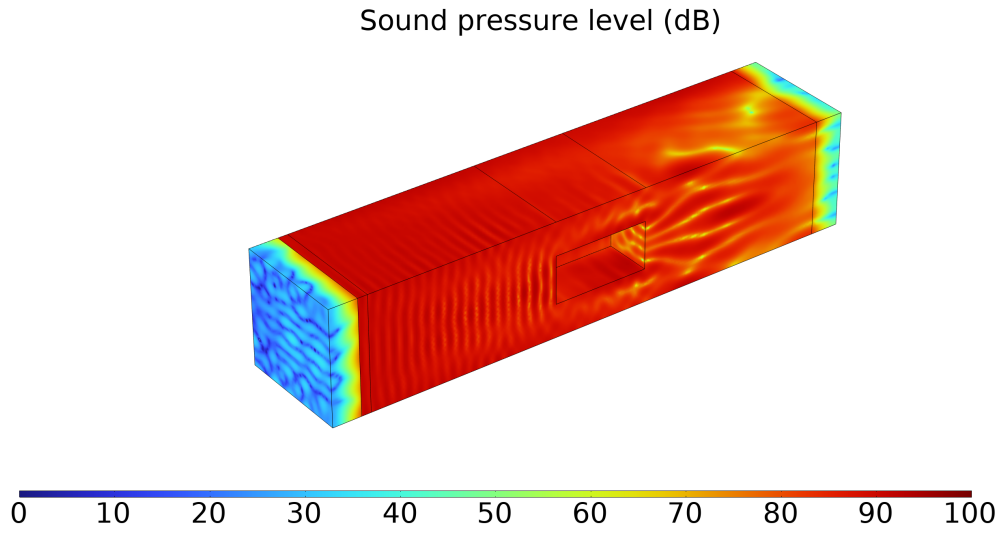

Figure 5.35: 3D SPL contour for Ma = 0.1 at 1500 Hz

In the Mach 0.1 scenario as seen in Figure 5.37b, the SPL values remain elevated throughout the domain, with slightly lower levels in the downstream areas. The relatively shortest wavelength at 1500 Hz, which can be observed in Figure 5.41, results in more densely packed standing wave patterns, especially around the centre and further downstream. These patterns are caused by constructive interference as sound waves reflect off the component box and boundaries, concentrating the pressure in specific regions. The lower SPL region downstream in this case could be due to the turbulent mixing, where the higher frequency wave interacts with the turbulent flow downstream. While some lower-SPL pockets (10-30 dB) exist near the sound source, they are relatively small due to the fast-moving airflow. This rapid downstream movement leaves little room for sound to dissipate naturally, causing significant noise amplification as waves accumulate in the far downstream regions.
In the vertical plane for Mach 0.1, as observed in Figure 5.38b, the SPL remains relatively high, particularly downstream where levels reach 80-90 dB. The standing wave patterns become more prominent in these areas as reflections from the boundaries intensify the noise. There are some lower-SPL zones (10-30 dB) upstream, but

they are limited, as the faster airflow continues to push sound energy toward the downstream region, increasing noise accumulation.

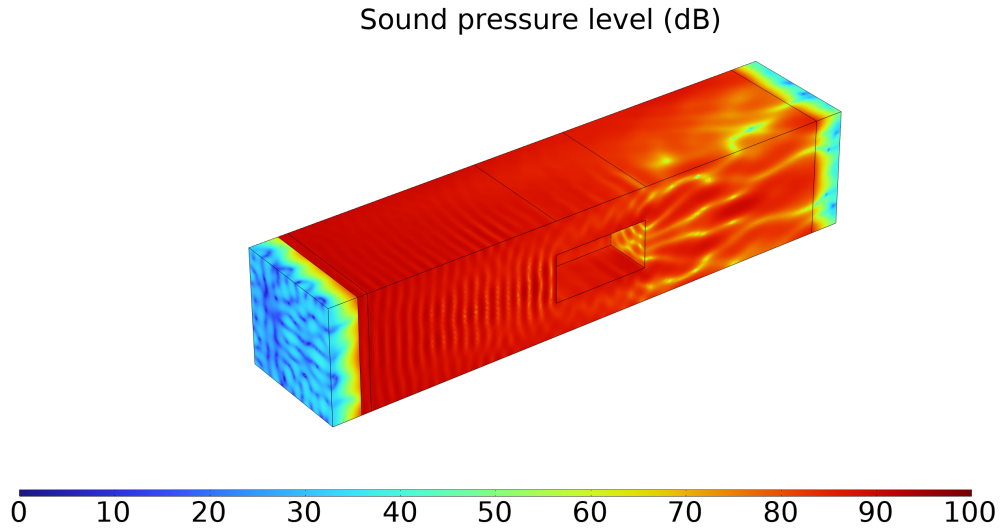

Figure 5.36: 3D SPL contour for Ma = 0.05 at 1500 Hz

In contrast, the Mach 0.05 simulation from Figure 5.37a presents a more evenly distributed SPL, with high-SPL regions (70-80 dB) still concentrated downstream, but with slightly less intensity than in the Mach 0.1 case. The standing wave patterns are not as tightly packed, and larger low-SPL areas are visible near the sound source and upstream. The slower airflow helps sound to dissipate more naturally, leading to less pronounced interference and a smoother propagation of sound waves throughout the domain.

Along the y-axis, the Mach 0.05 case, as seen in Figure 5.38a, similarly shows a more balanced SPL distribution, with larger low-SPL zones (20-40 dB) near the upstream boundary. While the high-SPL regions remain present downstream, the standing waves are more spaced out compared to Mach 0.1. The reduced airflow allows for better dissipation, softening the interference and resulting in a more gradual buildup of noise throughout the domain. High-SPL regions are less concentrated, and the overall sound pressure levels are more evenly spread.

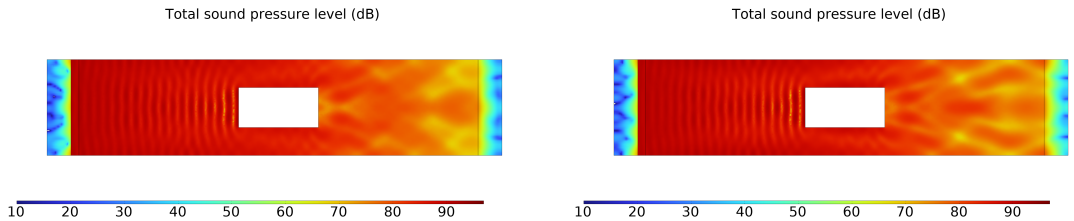

(a) Mach 0.05 **(b)** Mach 0.1

Figure 5.37: SPL contour along x-direction

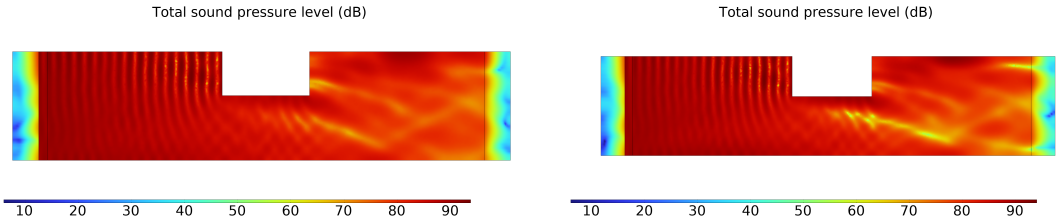

(a) Mach 0.05 **(b)** Mach 0.1

Figure 5.38: SPL contour along y-direction

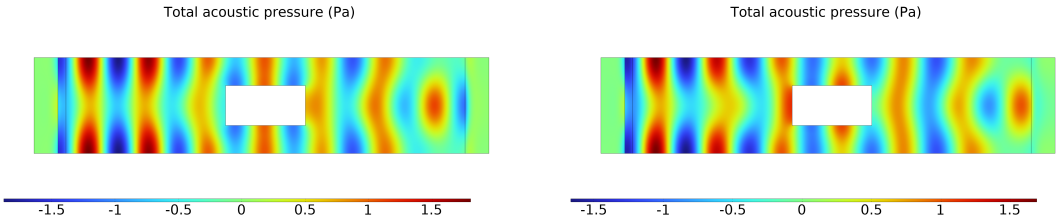

(a) Mach 0.05 **(b)** Mach 0.1

Figure 5.39: TAP contour along x-direction for $f = 500$ Hz

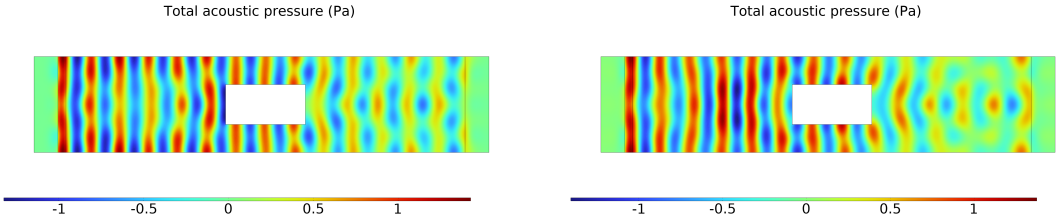

(a) Mach 0.05 **(b)** Mach 0.1

Figure 5.40: TAP contour along x-direction for $f = 1000$ Hz

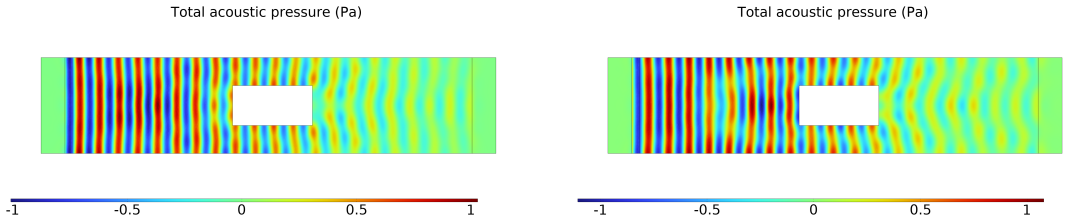

(a) Mach 0.05 **(b)** Mach 0.1

Figure 5.41: TAP contour along x-direction for $f = 1500$ Hz

5.6 Simulation With Acoustic Metamaterials

In this section, one takes a closer look at the sound pressure level (SPL) contour plots for frequencies of 500 Hz, 1000 Hz, and 1500 Hz, under both Mach 0.1 and

Mach 0.05 flow conditions. This time, acoustic metamaterials (AMM) have been added, creating an impedance boundary layer that changes how the sound waves behave. By examining the x-axis and y-axis results, one can see how well the AMM reduces noise and minimizes standing wave patterns in the under-cab area of a truck. These findings are compared with earlier simulations, where no metamaterials were used, to highlight the improvements in noise control and sound distribution with the AMM in place.

5.6.1 500 Hz

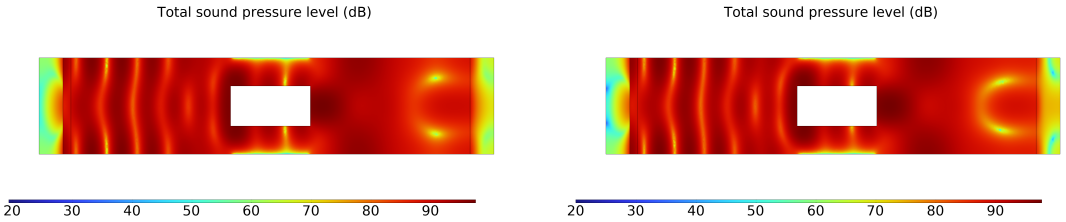

(a) Mach 0.05 **(b)** Mach 0.1

Figure 5.42: SPL contour along x-direction

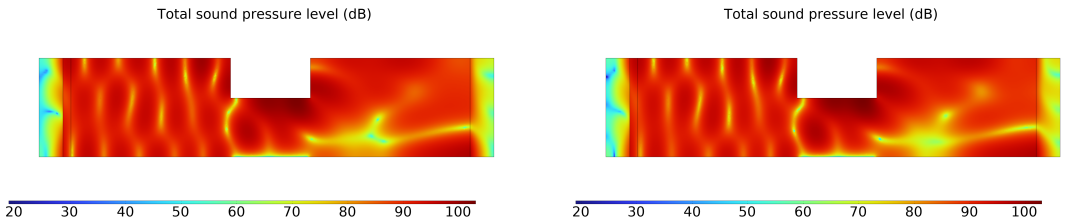

(a) Mach 0.05 **(b)** Mach 0.1

Figure 5.43: SPL contour along y-direction

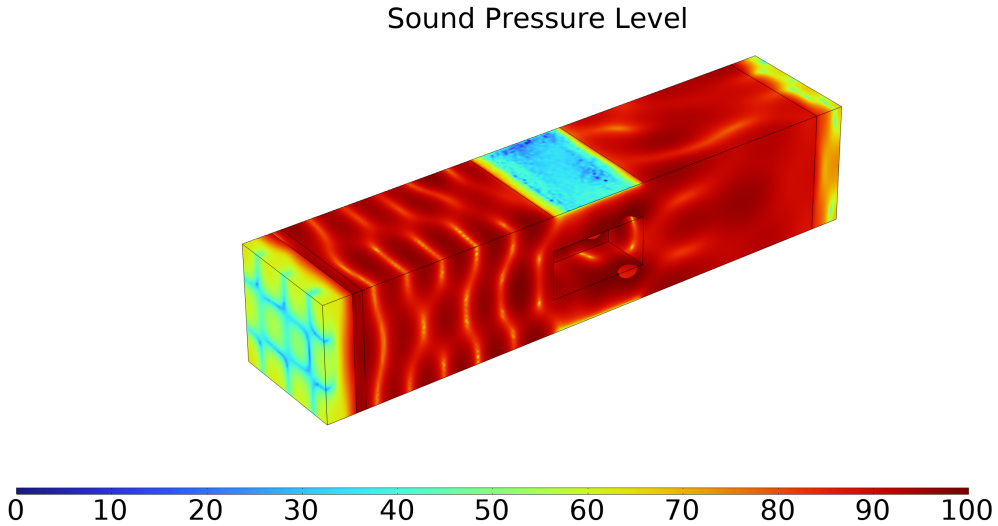

Figure 5.44: 3D SPL contour for Ma = 0.1 at 500 Hz, with metamaterial

In the Mach 0.1 case with the introduction of metamaterials (AMM), as seen in Figure 5.42b, there is a clear reduction in SPL compared to the simulations without AMM. The high-SPL zones are now largely contained near the upstream region where the sound source is located, and they no longer extend to the downstream area. SPL levels downstream have dropped to 70-85 dB, a significant improvement from the 80-90 dB seen previously. However, there still exists spots of relatively high SPL regions close to the box, ceiling and floor. This is due to the lack of wave reflections in those regions. The standing wave patterns, which were more evident without AMM, have been substantially minimized. The metamaterials' impedance boundary effectively absorbs much of the sound energy, reducing reflections that lead to constructive interference. This absorption can be seen at the impedance surface on the ceiling and the floor where the SPL is extremely low and this influences the SPL region downstream along with the flow. This dampening of interference results in a more gradual decrease in sound pressure across the domain, with more uniform SPL levels downstream, demonstrating the AMM's success in noise control and energy dissipation.
Along the y-axis in the Mach 0.1 case, as observed in Figure 5.43b, the effectiveness of the AMM is even more evident, especially in reducing SPL in high-noise areas near the downstream boundary. Previously, SPL values in this region reached up to 100 dB, but with the AMM, these have been reduced to 80-90 dB. The metamaterials dampen the formation of standing waves, making them less noticeable and resulting in a smoother sound pressure distribution. The effect of the impedance boundary can be seen more clearly in this view and its influence on the downstream is more evident. Sound energy in the downstream area is now spread more evenly. Additionally, the presence of low-SPL areas upstream, ranging between 20-50 dB, highlights the ability of the AMM to absorb sound energy, preventing noise buildup and limiting reflections.

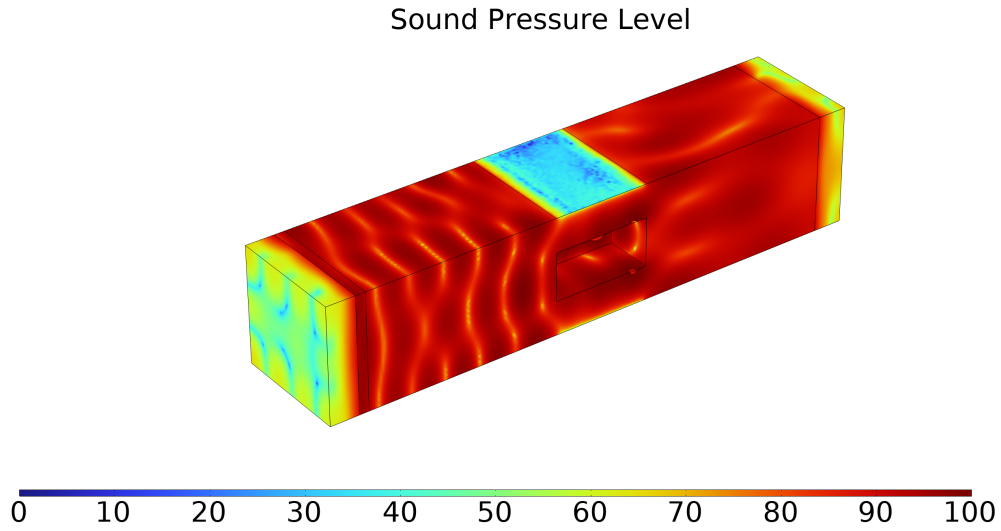

Figure 5.45: 3D SPL contour for Ma = 0.05 at 500 Hz, with metamaterial

In the Mach 0.05 case, the noise reduction is even more pronounced, which can be observed in Figure 5.42a. SPL values across the domain are more evenly distributed,

with fewer high-SPL regions compared to the Mach 0.1 case. Most of the domain shows SPL levels between 70-85 dB, with only small areas near the boundaries reaching more than 90 dB. The standing waves that were prominent in the simulation without AMM have been significantly dampened, resulting in a more uniform distribution of sound in the under-cab region. The combination of slower airflow at Mach 0.05 and the AMM's impedance boundary creates a stable and controlled propagation of sound, minimizing noise buildup in the downstream section.
In the Mach 0.05 case along the y-axis, Figure 5.43a shows a uniform and controlled SPL distribution. SPL levels range from 50-70 dB across the domain, with only a few small areas reaching up to 80 dB, a stark contrast to the previous results without AMM, where values spiked to 100 dB in certain regions. The pattern formed due to the absorption at the impedance layer is similar to the Mach 0.1 case. The metamaterials are highly effective in reducing noise, and the slower airflow allows for more natural sound dissipation. The reduction of standing waves and the lack of significant interference patterns indicate that the AMM is efficiently absorbing sound energy. The overall SPL distribution is much smoother, with minimal high-pressure areas, showcasing how well the AMM can mitigate noise in this environment.

5.6.1.1 Effectiveness of Acoustic Metamaterials at 500 Hz

The addition of acoustic metamaterials has a notable impact on how sound propagates and on overall noise levels in both Mach 0.1 and Mach 0.05 flow conditions. The metamaterials' impedance boundary is key, absorbing sound energy, reducing reflections, and limiting the formation of standing waves.

- Noise Reduction: In both Mach 0.1 and Mach 0.05, the metamaterials greatly reduce SPL levels across the domain. In Mach 0.1, the most significant reduction occurs downstream, where noise previously peaked at 90-100 dB. With the metamaterials in place, SPL levels drop to 60-80 dB, demonstrating a substantial improvement in noise control. In Mach 0.05, the reduction is even more effective, with SPL levels decreasing to 50-70 dB, showing that the combination of slower airflow and metamaterials leads to better noise reduction.
- Standing Wave Control: The metamaterials effectively reduce standing wave patterns, which were a prominent issue in the simulations without AMM. The impedance boundary absorbs sound that would otherwise reflect off the boundaries, minimizing constructive interference. This results in a more uniform SPL distribution with fewer high-SPL areas and more balanced noise levels throughout the domain. Downstream regions that previously saw significant noise buildup now show a more gradual decrease in sound pressure.

5.6.1.2 Comparison to Simulations Without Metamaterials

Comparing the 500 Hz simulations with and without AMM clearly shows how much of an impact metamaterials have on controlling noise. In the Mach 0.1 case without AMM, there was substantial noise buildup in the downstream region, with SPL levels reaching 90-100 dB and clear standing wave patterns. After adding the metamaterials, these levels dropped to 60-80 dB, and the standing waves were greatly reduced. By preventing sound wave reflections, the metamaterials create smoother

SPL profiles and reduce noise amplification downstream.
In the Mach 0.05 scenario, SPL values without AMM were lower than in Mach 0.1 but still showed localized high-SPL zones in the downstream area. After incorporating AMM, these high-SPL zones were reduced, and standing waves were almost eliminated. The slower airflow in Mach 0.05, combined with the effects of the metamaterials, produces a more controlled sound environment, with SPL values ranging from 50-70 dB and fewer areas of noise buildup. This shows that metamaterials are highly effective at reducing noise, especially in conditions with slower airflow like Mach 0.05.

5.6.2 1000 Hz

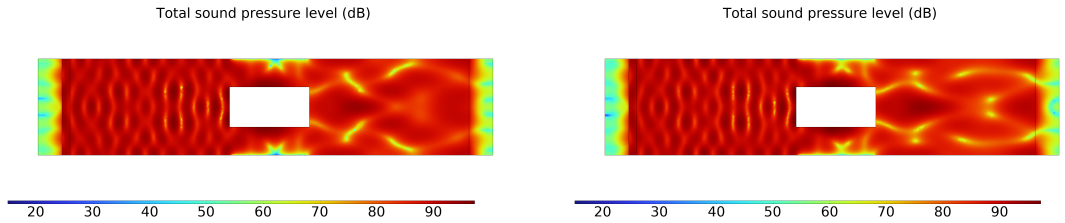

(a) Mach 0.05 **(b)** Mach 0.1

Figure 5.46: SPL contour along x-direction

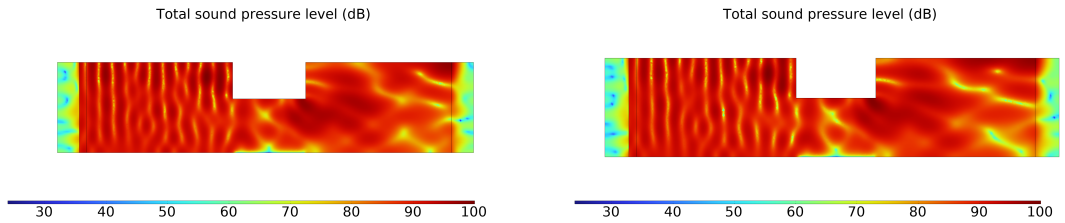

(a) Mach 0.05 **(b)** Mach 0.1

Figure 5.47: SPL contour along y-direction

In the Mach 0.1 scenario with acoustic metamaterials (AMM), as shown in Figure 5.46b, there is a significant drop in SPL compared to the setup without AMM. High-SPL areas are now mostly concentrated near the sound source in the upstream region, while SPL levels downstream have reduced to 60-80 dB, compared to the 80-90 dB seen previously. The standing wave patterns, which were much more prominent without AMM, have been greatly minimized, and a unique pattern is formed due to the metamaterials' impedance boundary, which absorbs a large portion of the sound energy, preventing reflections that would otherwise cause constructive interference and the flow-acoustic interaction. A slightly thicker zone of low SPL region is observed at the impedance boundary when compared to 500 Hz simulation, which is a result of an increase in frequency. This results in a smoother, more gradual decrease in SPL across the domain, leading to a more even sound pressure distribution downstream.

Along the y-axis in the Mach 0.1 case, from Figure 5.47b, the AMM continues to show its effectiveness in reducing SPL, particularly in the high-SPL zones near the downstream boundary and the zone of thicker low SPL region near the impedance boundary is more evident. Without the AMM, SPL levels reached up to 100 dB, but with the metamaterials in place, these values drop to 70-80 dB with there being still a concentration of high SPL zones near the wall edges. The AMM not only absorbs sound energy but also significantly reduces the formation of standing waves, resulting in a more uniform sound pressure distribution. The upstream region, with SPL values ranging from 20-50 dB, highlights how well the AMM absorbs sound energy, reducing noise buildup and limiting reflections from the duct boundaries. Flow turbulence in this scenario also plays a role—interacting with the sound waves and further contributing to SPL reduction downstream, as the turbulence breaks up and scatters the sound waves, making it harder for them to reinforce each other through reflections.

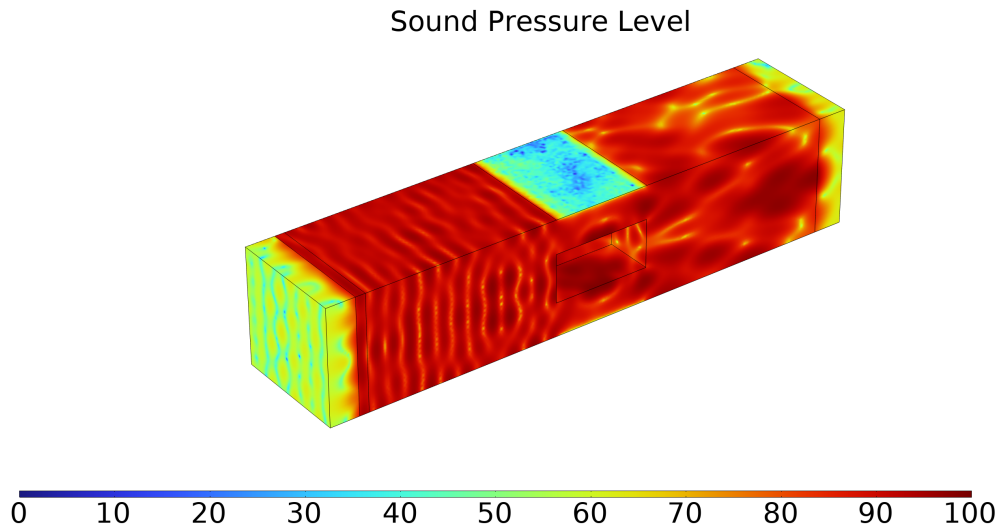

Figure 5.48: 3D SPL contour for Ma = 0.1 at 1000 Hz, with metamaterial

In the Mach 0.05 case, as observed from Figure 5.46a, the SPL reduction is also more pronounced. Most of the downstream now show SPL values in the 65-80 dB range, with only small areas near the sound source and at the downstream boundary reaching greater than 85 dB. The slower airflow combined with the metamaterials helps to effectively dampen standing waves, leading to more consistent sound propagation across the domain. The reduced airflow speed, along with the AMM's impedance boundary, helps prevent noise buildup, resulting in more stable and controlled sound wave behavior. The turbulence is less intense in this scenario, which allows the metamaterials to work even more effectively, smoothing out noise levels and ensuring a more uniform sound pressure distribution downstream.
When looking at the y-axis in the Mach 0.05 case, from Figure 5.47a the sound pressure distribution is similar to that of Mach 0.1. SPL values across the domain are lower in comparison, with only isolated high-SPL regions reaching greater than 90 dB. This is a marked improvement compared to the setup without AMM, where SPL values in some areas reached up to 100 dB downstream, consistently being in

the 90 dB range. The metamaterials prove highly effective in mitigating both sound waves and standing wave formation, creating a more balanced SPL distribution. At this lower Mach number, the AMM performs particularly well, absorbing sound energy and managing reflections, which results in a more uniform and controlled sound field throughout the domain.

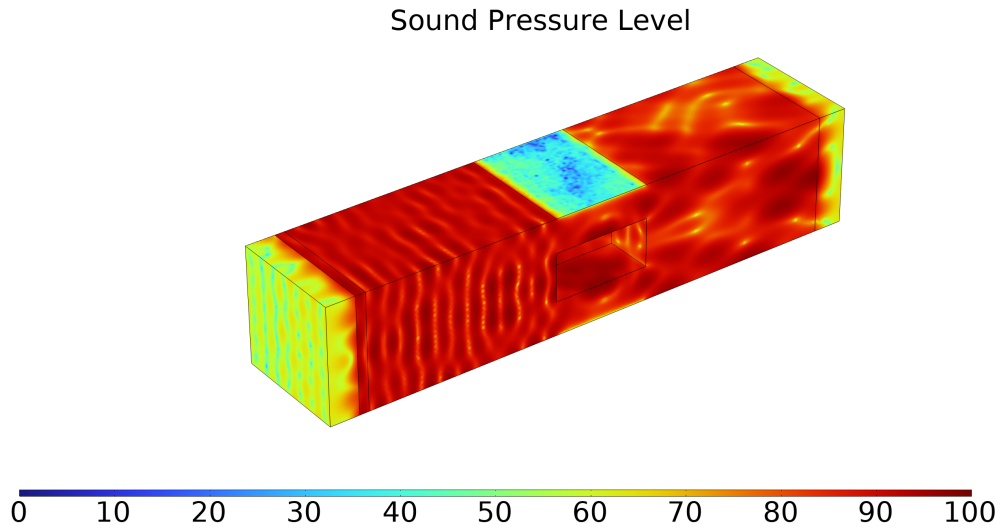

Figure 5.49: 3D SPL contour for Ma = 0.05 at 1000 Hz, with metamaterial

5.6.2.1 Effectiveness of Acoustic Metamaterials at 1000 Hz

The introduction of acoustic metamaterials (AMM) has a noticeable effect on how sound waves travel and on noise levels under both Mach 0.1 and Mach 0.05 flow conditions. The metamaterials create an impedance boundary that helps to absorb sound, cut down on reflections, and reduce the formation of standing waves.

- Noise Reduction: In Mach 0.1, the use of AMM leads to a marked reduction in SPL levels, especially in the downstream area where noise previously reached 90-100 dB. With the AMM, these values drop to 60-80 dB, reflecting improved noise control. In the Mach 0.05 case, the noise reduction is observed to be slightly substantial, with SPL levels across the domain falling to 60-80 dB. This indicates that slower airflow, when combined with AMM, allows for better noise attenuation and a more balanced SPL distribution.
- Standing Wave Control: The AMM also significantly reduces the standing wave patterns that were prominent in the cases without metamaterials. By absorbing the sound energy that would have otherwise been reflected and caused interference, the AMM ensures a smoother SPL distribution and fewer high-SPL regions. This results in more consistent noise levels across the domain.

5.6.2.2 Comparison to Simulations Without Metamaterials

In the Mach 0.1 case without AMM, the downstream region showed considerable noise buildup, with SPL values spiking to 90-100 dB and noticeable standing wave

formations. After adding AMM, these levels drop to 60-80 dB, and the standing waves are significantly reduced. The AMM absorbs much of the sound energy, preventing it from reflecting back and reducing the noise amplification downstream. This leads to smoother SPL profiles and more controlled sound wave behavior.
In the Mach 0.05 scenario, the SPL levels without AMM were lower than in Mach 0.1, although high-SPL zones still appeared in the downstream areas. With the introduction of AMM, these high-SPL regions are reduced further, and standing waves are nearly eliminated. The combination of slower airflow and AMM results in more stable sound propagation, with SPL values falling between 55-80 dB. The metamaterials prove especially effective in these lower velocity conditions, allowing for a more uniform sound pressure distribution throughout the domain.

5.6.3 1500 Hz

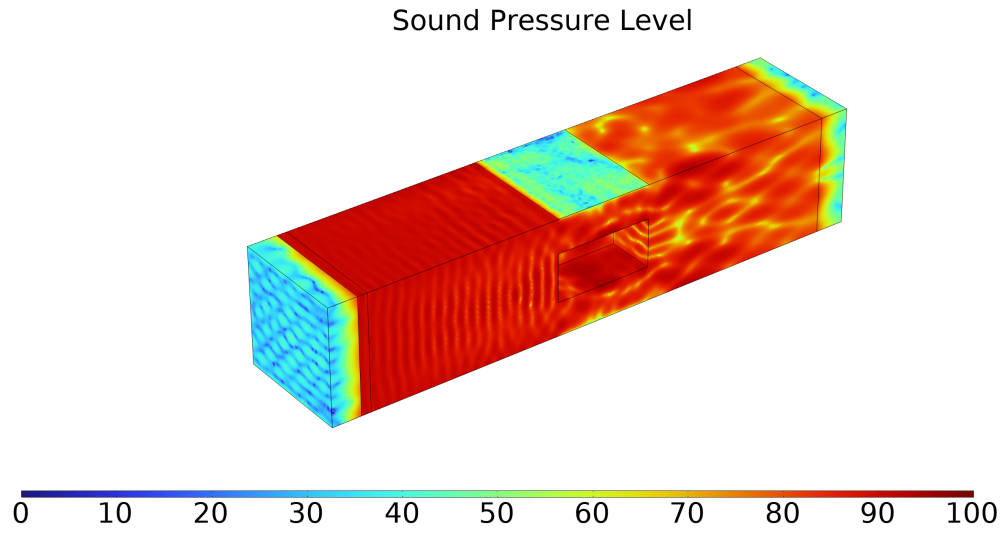

Figure 5.50: 3D SPL contour for Ma = 0.1 at 1500 Hz, with metamaterial

In the Mach 0.1 scenario, the inclusion of acoustic metamaterials (AMM) leads to a significant drop in SPL, particularly in the downstream area, as seen in Figure 5.52b. High-SPL regions, which previously peaked at 80-90 dB without the metamaterials, are now reduced to 60-80 dB. The areas of high pressure remain mostly concentrated near the sound source and do not propagate as far downstream as they did in the non-AMM simulations. Standing wave patterns, which were prominent without the metamaterials, are greatly reduced. The AMM's impedance boundary plays a key role by absorbing sound energy, reducing reflections, and preventing constructive interference. The pattern seems to have developed further due to the increase in the total number of reflections as a result of the smallest wavelength (visually observed in Figure 5.56). This leads to the best reduction in SPL seen yet with most of the downstream being significantly lower-end compared to other frequencies, with this region showing much smoother and more controlled sound distribution.
When analyzing the Mach 0.1 case along the y-axis, from Figure 5.53b it is evident that the AMM continues to demonstrate its effectiveness in reducing SPL, especially

in regions near the downstream boundary. Without the AMM, SPL values previously reached 90-100 dB, but with the metamaterials, they are now reduced to 70-80 dB. The impedance boundary provided by the AMM effectively dampens standing waves, creating a more even sound pressure distribution throughout the domain. The SPL seems to have dropped considerably with high SPL concentration (>80dB) mostly situated near the box boundaries. The combination of short wavelength and high flow speed along with turbulence appears to cover most of the downstream region in uniform and more consistent noise levels, while low-SPL areas upstream (ranging from 20-50 dB) reflect the metamaterials' ability to absorb sound energy and limit reflections and noise accumulation.

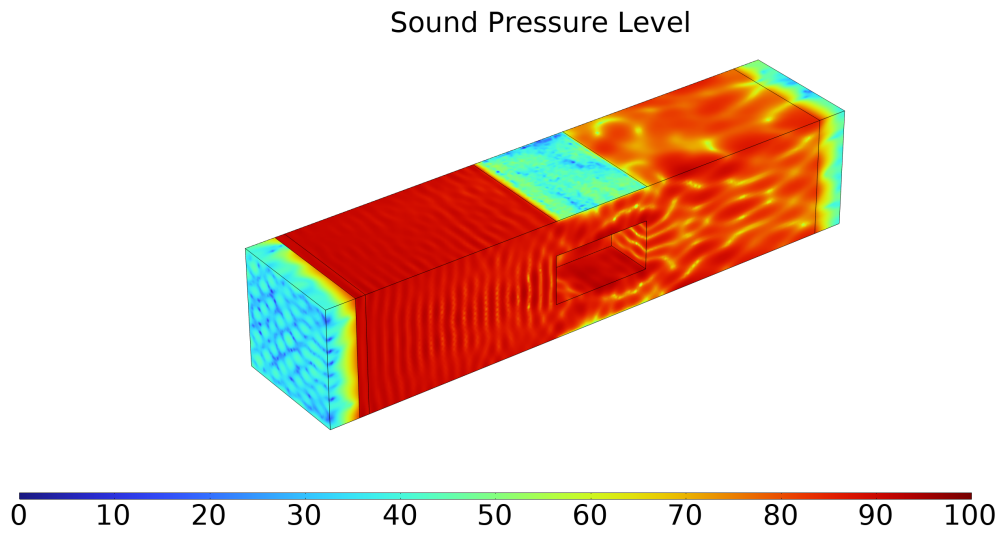

Figure 5.51: 3D SPL contour for Ma = 0.05 at 1500 Hz, with metamaterial

From Figure 5.52a, for the Mach 0.05 case, the AMM demonstrates slightly greater efficiency in noise reduction. SPL values throughout the domain range between 50-70 dB and is more spread out until the boundaries of the domain, with only small areas near the boundaries reaching 80 dB. Although the pattern appears to be similar to the Mach 0.1 case, the combination of slower airflow and the AMM enhances sound dissipation, with standing wave formations being significantly reduced. The sound pressure is more uniformly distributed across the under-cab region, highlighting how the metamaterials excel in controlling noise under lower-flow conditions.

In the y-axis view of the Mach 0.05 case, as observed from Figure 5.53a, the sound pressure distribution is very similar to the Mach 0.1 scenario. Most of the domain shows SPL values between 60-70 dB. This is a significant improvement compared to the simulations without AMM, where some areas saw SPL values as high as 100 dB. The AMM effectively absorbs sound energy and reduces the formation of standing waves, resulting in a smooth and controlled SPL distribution. This demonstrates the metamaterials' capability to efficiently mitigate noise, particularly in conditions with slower airflow like Mach 0.05.

5.6.3.1 Effectiveness of Acoustic Metamaterials at 1500 Hz

At 1500 Hz, the use of acoustic metamaterials (AMM) greatly improves how sound behaves, especially when it comes to reducing noise levels in both Mach 0.1 and Mach 0.05 flow conditions. The key feature of metamaterials is their impedance boundary, which plays a major role in absorbing sound energy, cutting down on reflections, and minimizing the formation of standing waves.

- Noise Reduction: In the Mach 0.1 case, the introduction of AMM leads to the most notable decrease in noise levels, particularly in the downstream region, where SPL values previously spiked to 100 dB. With the AMM, these levels drop to 60-70 dB, highlighting how effective the metamaterials are at controlling sound. In Mach 0.05, the improvement is even more striking and uniform. SPL levels across most of the domains fall significantly, demonstrating that slower airflow paired with AMM results in more efficient noise reduction.
- Standing Wave Control: Another benefit of AMM is its ability to dramatically reduce standing waves, which were a big issue in the simulations without the metamaterials. By absorbing sound and preventing it from bouncing back, AMM stops the sound waves from overlapping and interacting with the turbulence created due to the box which would otherwise create areas of high pressure. This results in smoother and uniform SPL distribution and fewer high-SPL spots, especially in the downstream areas where noise buildup was a problem.

5.6.3.2 Comparison to Simulations Without Metamaterials

In the Mach 0.1 case without AMM, noise levels peaked at 90-100 dB in the downstream region, with clear evidence of strong standing wave formations. After incorporating AMM, these SPL levels dropped to 60-70 dB, and the standing waves were significantly reduced. The metamaterials effectively absorb sound energy and prevent excessive reflections, leading to a much smoother and more controlled distribution of SPL across the domain. This simulation result showed the most promise in terms of reducing the SPL in the downstream region.

In Mach 0.05 without AMM, although noise levels were somewhat lower than in Mach 0.1, there were still areas of high SPL, particularly in the downstream region. With the addition of AMM, these high-SPL zones were significantly reduced, and the standing waves nearly disappeared. The slower airflow, combined with the metamaterials, creates a more balanced SPL distribution, including at the wall edges, with values ranging from 50-70 dB across the domain and far fewer areas with high noise levels. AMM shows its strength in lower-flow conditions, proving to be highly effective at controlling noise and reducing standing waves.

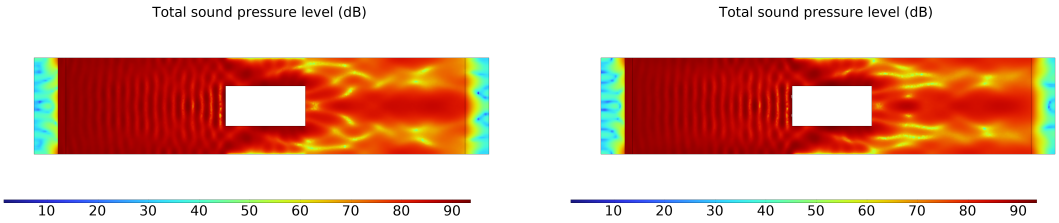

(a) Mach 0.05 **(b)** Mach 0.1

Figure 5.52: SPL contour along x-direction

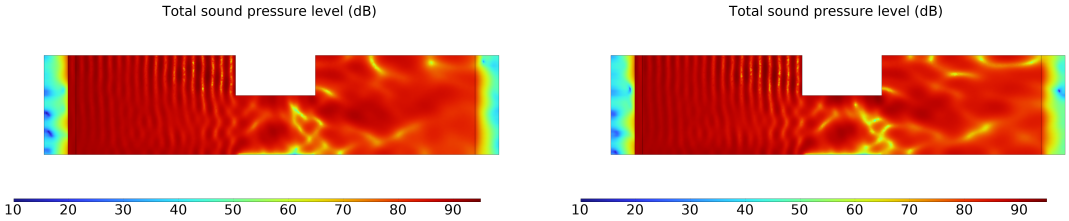

(a) Mach 0.05 **(b)** Mach 0.1

Figure 5.53: SPL contour along y-direction

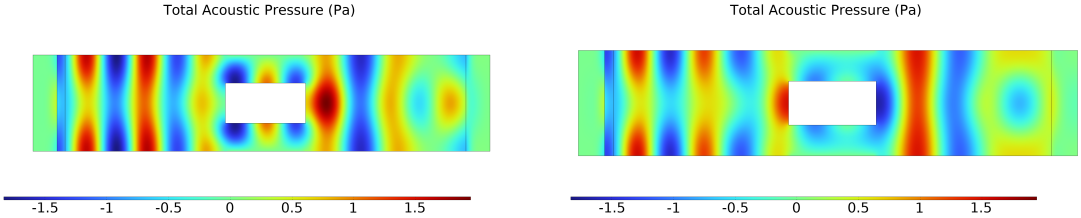

(a) Mach 0.05 **(b)** Mach 0.1

Figure 5.54: TAP contour along x-direction for $f = 500$ Hz

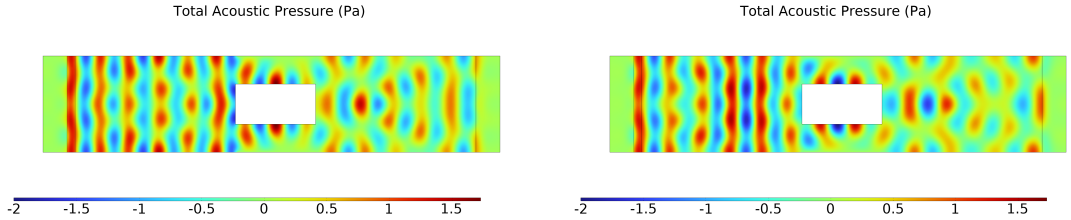

(a) Mach 0.05 **(b)** Mach 0.1

Figure 5.55: TAP contour along x-direction for $f = 1000$ Hz

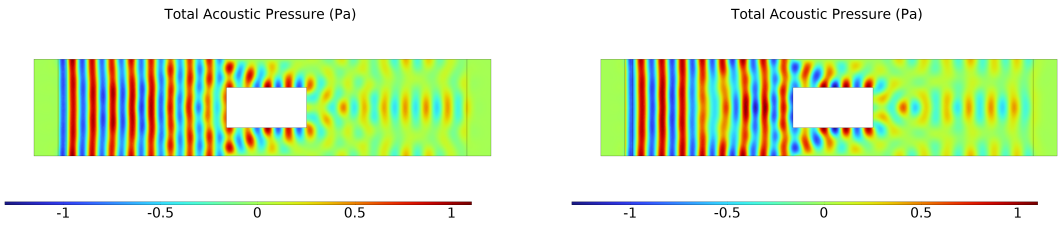

(a) Mach 0.05 **(b)** Mach 0.1

Figure 5.56: TAP contour along x-direction for $f = 1500$ Hz

6

Conclusion

This thesis aimed to address a key challenge in noise control – balancing sound absorption with minimal obstruction to airflow, particularly relevant in applications such as cooling fans in heavy-duty trucks. The design, optimization, and simulation of two types of conceptual AMMs were conducted to resolve the challenge.

The conceptual AMMs explored in this thesis include the space-coiling structure and the DLMPP, designed to attenuate tonal noise and broadband noise, respectively. Their performance was evaluated through theoretical calculations and computational simulations using COMSOL. Simulations incorporated flow conditions at Mach numbers 0.05, 0.06, and 0.1 within the acoustic field. A single space-coiling cell was simulated with its alignment parallel to the flow direction, while another simulation applied the designed acoustic impedance of the DLMPP in an under-cab scenario. Simulation results indicate that these AMMs have minimal impact on airflow velocity within the exhaust pipe, offering a promising solution for future fan noise reduction applications.

The **space-coiling** structure was developed to target the specific tonal noise generated by the fan's BPF and its harmonics. Using the principles of Fano-like resonance and sound wave interference, the structure was optimized to reduce tonal peaks while allowing airflow through its coiled channels. The theoretical model for this structure was developed using TMM as the sequence combination of subchannels. Simulations were performed under both no-flow and flow conditions. The results showed that the tuned space-coiling structure was effective in attenuating tonal noise around a fundamental frequency and its harmonics for both flow cases and no-flow cases. It can be observed that the flow will lower the peak absorption coefficient as well as its frequency. While the simulation case shows an agreement with theoretical calculation, the fundamental frequency has shifted from the original designed value. This is mainly because of a small deviation of the geometry parameters in the model. However, with a convincing absorption profile, these variations were minor and can be optimized in a future study.

Moreover, unequal opening space-coiling structures on noise absorption have been studied. Preliminary studies suggested that unequal openings might offer some benefits in noise reduction, but they did not yield significant advantages over the equal-opening designs in this study. The uneven way discussed in this study gave a similar absorption peak width with even one. Moreover, it lost the evenness distribution of harmonics. A more detailed investigation into the geometric variations and their effects on both tonal and broadband noise absorption could provide new insights.

The **DLMPP** was designed to target broadband noise in the range of 300 Hz to

2000 Hz. The absorption coefficient of the structure was presented by geometry parameters through the use of EEC. After a careful parameter sweep and sensitivity analysis, the DLMPP demonstrated effective sound absorption over a wide frequency range, with a particular focus on reducing mid to high-frequency noise. The optimized design showed a good broad absorption band spanning approximately 1300 Hz, which aligns well with the expected noise frequencies of fan operation.
From the aspect of the under-cab simulation scenario, the results clearly demonstrate the effectiveness of the AMM in reducing noise and controlling sound wave propagation across different flow conditions and frequencies. At Ma=0.1, noise levels and standing wave patterns were consistently higher compared to Ma=0.05. However, the addition of DLMPP significantly reduced SPL levels and controlled noise buildup in both cases. Also, the 1500 Hz simulation with the DLMPP showed a notable noise reduction, especially in the downstream area, where high-SPL zones dropped by as much as 10-20 dB. Lastly, without DLMPP, higher frequencies (1000 Hz and 1500 Hz) experienced more severe standing wave patterns and greater noise accumulation, but the DLMPP effectively mitigated these issues, resulting in smoother sound pressure distributions and less noise amplification.
These findings provide solid evidence that AMMs are a valuable solution for reducing noise in confined spaces where airflow and acoustic interactions occur. The impedance boundary created by the metamaterials is essential in absorbing sound energy, reducing reflections, and minimizing constructive interference. This research is particularly relevant for noise control applications in transportation, where better sound attenuation can enhance acoustic performance and improve environmental conditions.
Looking forward, there are several areas where future work could extend the findings of this thesis. One key direction would be further optimization of the space-coiling structure to enhance its performance across a wider frequency range. While the current design was effective for tonal noise reduction, increasing the bandwidth of absorption could make it more versatile for broader noise control applications. Additionally, experimental validation of these designs in real-world environments, such as in truck cooling systems, would be essential to confirm the effectiveness of AMMs under operational conditions.

Bibliography

[1] Patrick R. Amestoy et al. "A fully asynchronous multifrontal solver using distributed dynamic scheduling". In: *SIAM Journal on Matrix Analysis and Applications* 23.1 (2001), pp. 15–41. DOI: 10.1137/S0895479899358194.

[2] Ayyar, Eshaan, Patidar, Ashok, and LASHKARI, Vikas. "Assessment Optimization of Front End Cooling Module of a Commercial Vehicle by CFD Simulation Prototype Testing". In: *WCX SAE World Congress Experience*. SAE International, Apr. 2020. DOI: https://doi.org/10.4271/2020-01-0164. URL: https://doi.org/10.4271/2020-01-0164.

[3] Leo L. Beranek and Tim J. Mellow. "Chapter 3 - Electro-mechano-acoustical circuits". In: *Acoustics: Sound Fields and Transducers*. Ed. by Leo L. Beranek and Tim J. Mellow. Academic Press, 2012, pp. 65–118. ISBN: 978-0-12-391421-7. DOI: https://doi.org/10.1016/B978-0-12-391421-7.00003-8. URL: https://www.sciencedirect.com/science/article/pii/B9780123914217000038.

[4] Jens Blauert and Ning Xiang. *Acoustics for engineers: Troy lectures*. Springer, 2009.

[5] Zhigang Cao, Xin Li, and Bilong Liu. "Broadband sound absorption of a hybrid absorber with shunt loudspeaker and perforated plates". In: *Applied Acoustics* 203 (2023), p. 109185.

[6] I. Cohen and K. Kundu. *Fluid mechanics*. 4th ed. Elsevier Science Technology. Burlington, 2007.

[7] Lars Davidsson. *Fluid mechanics, turbulent flow and turbulence modeling*. unpublished. Division of Fluid Dynamics, Department of Mechanics and Maritime Sciences, Chalmers University of Technology. Gothenburg, 2023. URL: https://www.tfd.chalmers.se/~lada/comp_turb_model/ebook.html.

[8] Ian Davis, Andrew McKay, and Gareth J Bennett. "A graph-theory approach to optimisation of an acoustic absorber targeting a specific noise spectrum that approaches the causal optimum minimum depth". In: *Journal of Sound and Vibration* 505 (2021), p. 116135.

[9] Ahmed G Gad. "Particle swarm optimization algorithm and its applications: a systematic review". In: *Archives of computational methods in engineering* 29.5 (2022), pp. 2531–2561.

[10] Reza Ghaffarivardavagh et al. “Horn-like space-coiling metamaterials toward simultaneous phase and amplitude modulation”. In: *Nature communications* 9.1 (2018), p. 1349.

[11] Guangming Guo, Junjie Gong, and Mengqi Zhang. “Numerical investigation on flow characteristics of low-speed flow over a cavity with small aspect ratio”. In: *International Journal of Mechanical Sciences* 178 (2020), p. 105632. ISSN: 0020-7403. DOI: https://doi.org/10.1016/j.ijmecsci.2020.105632. URL: https://www.sciencedirect.com/science/article/pii/S0020740319346223.

[12] Hallqvist, Thomas. “The Cooling Airflow of Heavy Trucks - a Parametric Study”. In: *SAE International Journal of Commercial Vehicles* 1.1 (Apr. 2008), pp. 119–133. DOI: https://doi.org/10.4271/2008-01-1171. URL: https://doi.org/10.4271/2008-01-1171.

[13] Baoding Huang et al. “Numerical Investigation on the Aerodynamic and Aeroacoustic Characteristics in New Energy Vehicle Cooling Fan with Shroud”. In: *Processes* 12.2 (2024). ISSN: 2227-9717. DOI: 10.3390/pr12020333. URL: https://www.mdpi.com/2227-9717/12/2/333.

[14] ITTC. *Practical Guidelines for Ship CFD Applications*. 2013. URL: https://ittc.info/media/1357/75-03-02-03.pdf.

[15] Jack Killeen et al. “Fan-noise reduction of data centre telecommunications’ server racks, with an acoustic metamaterial broadband, low-frequency sound-absorbing liner”. In: *Applied Acoustics* 203 (2023), p. 109229.

[16] Mendel Kleiner. *Acoustics and audio technology*. J. Ross Publishing, 2011.

[17] Mendel Kleiner. *Electroacoustics*. CRC Press, 2013.

[18] Hassan Lakzayi, Zeinab Pouransari, and MohammadReza KargarAbjahan. “Numerical and experimental investigation of aerodynamic noise from a cooling fan in a turbulent flow”. In: *International Journal of Aeroacoustics* 23.1-2 (2024), pp. 38–59. DOI: 10.1177/1475472X241226937. eprint: https://doi.org/10.1177/1475472X241226937. URL: https://doi.org/10.1177/1475472X241226937.

[19] Heming Li et al. “Design and study of broadband sound absorbers with partition based on micro-perforated panel and Helmholtz resonator”. In: *Applied Acoustics* 205 (2023), p. 109262.

[20] Yu-Yu Lu. *Experimental Study of Installation Effects on Cooling Fan Noise*. 2021.

[21] D. Y. Maa. “THEORY AND DESIGN OF MICROPERFORATED PANEL SOUND-ABSORBING CONSTRUCTIONS”. In: 1975. URL: https://api.semanticscholar.org/CorpusID:115008933.

[22] Jang-oh Mo and Jae-hyuk Choi. “Numerical Investigation of Unsteady Flow and Aerodynamic Noise Characteristics of an Automotive Axial Cooling Fan”. In: *Applied Sciences* 10.16 (2020). ISSN: 2076-3417. DOI: 10.3390/app10165432. URL: https://www.mdpi.com/2076-3417/10/16/5432.

[23] COMSOL Multiphysics. *COMSOL Multiphysics® v6.0. (2021). COMSOL Multiphysics® User's Guide. COMSOL AB.* URL: www.comsol.com.

[24] MUMPS Solver. *MUMPS Official Documentation.* http://mumps-solver.org. 2023.

[25] HQ Nguyen et al. "A Fano-based acoustic metamaterial for ultra-broadband sound barriers". In: *Proceedings of the Royal Society A* 477.2248 (2021), p. 20210024.

[26] Pan, Fongloon Peter et al. "A Practical Simulation Approach for Truck Cooling System At Early Stage Design Process and Development". In: *SAE 2010 Commercial Vehicle Engineering Congress*. SAE International, Oct. 2010. DOI: https://doi.org/10.4271/2010-01-1927. URL: https://doi.org/10.4271/2010-01-1927.

[27] Allan D Pierce. *Acoustics: an introduction to its physical principles and applications*. Springer, 2019.

[28] N F D Razak et al. "Noise and vibration analysis for automotive radiator cooling fan". In: *IOP Conference Series: Materials Science and Engineering* 257.1 (Oct. 2017), p. 012083. DOI: 10.1088/1757-899X/257/1/012083. URL: https://dx.doi.org/10.1088/1757-899X/257/1/012083.

[29] Youcef Saad and Martin H. Schultz. "GMRES: A Generalized Minimal Residual Algorithm for Solving Nonsymmetric Linear Systems". In: *SIAM Journal on Scientific and Statistical Computing* 7.3 (1986), pp. 856–869. DOI: 10.1137/0907058.

[30] Yousef Saad. *Iterative methods for sparse linear systems*. SIAM, 2003.

[31] Olaf Schenk and Klaus Gärtner. "PARDISO: A high-performance serial and parallel sparse linear solver in IBM SP". In: *Future Generation Computer Systems* 20.3 (2004), pp. 475–487. DOI: 10.1016/j.future.2003.07.011.

[32] Olaf Schenk and Klaus Gärtner. "Solving unsymmetric sparse systems of linear equations with PARDISO". In: *Journal of Future Generation Computer Systems* 20.3 (2002), pp. 475–487. DOI: 10.1016/S0167-739X(03)00157-2.

[33] Barry F. Smith, Petter E. Bjørstad, and William D. Gropp. "Domain decomposition methods: Theory and algorithms". In: *Cambridge Monographs on Applied and Computational Mathematics* 34 (2004). DOI: 10.1017/CBO9780511614095.

[34] Srinivasa, Vinod Kumar, S, Renjith, and Shome, Biswadip. "Design of Experiments Enabled CFD Approach for Optimizing Cooling Fan Performance". In: *SAE 2014 World Congress Exhibition*. SAE International, Apr. 2014. DOI: https://doi.org/10.4271/2014-01-0658. URL: https://doi.org/10.4271/2014-01-0658.

[35] Andrea Toselli and Olof B. Widlund. *Domain Decomposition Methods–Algorithms and Theory*. Springer, 2006. DOI: 10.1007/3-540-34469-X.

[36] Henk Karle Versteeg and Weeratunge Malalasekera. *An Introduction to Computational Fluid Dynamics: The Finite Volume Method*. 2nd. Pearson, 2007.

[37] Tor Erik Vigran. *Building acoustics*. CRC Press, 2014.

[38] Yan Wang et al. “Advances in Integrated Vehicle Thermal Management and Numerical Simulation”. In: *Energies* 10.10 (2017). ISSN: 1996-1073. DOI: 10.3390/en10101636. URL: https://www.mdpi.com/1996-1073/10/10/1636.

[39] Zhike Xu et al. “Design approach of perforated labyrinth-based acoustic metasurface for selective acoustic levitation manipulation”. In: *Scientific Reports* 11.1 (2021), p. 7619.

[40] Dacheng Zhang et al. “Study on Noise-Reduction Mechanism and Structural-Parameter Optimization of Ventilated Acoustic Metamaterial Labyrinth Plate”. In: *Applied Sciences* 14.17 (2024). ISSN: 2076-3417. DOI: 10.3390/app14177865. URL: https://www.mdpi.com/2076-3417/14/17/7865.

[41] Zhang, Chunhui, Uddin, Mesbah, and Foster, Lee. “Investigation of the Under-Hood Aero-Thermal Flow Features Using 3D CFD Simulation”. In: *WCX™ 17: SAE World Congress Experience*. SAE International, Mar. 2017. DOI: https://doi.org/10.4271/2017-01-0142. URL: https://doi.org/10.4271/2017-01-0142.

A

Appendix A

The figures below show SPL contour about the z-axis for various configurations, where:

- a: z-plane before impedance layer
- b: z-plane in between the impedance layer
- c: z-plane after the impedance layer

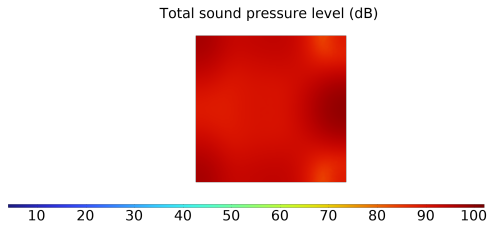

(a) a

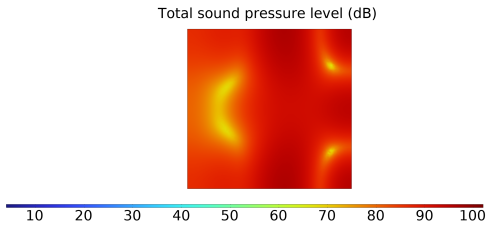

(b) b

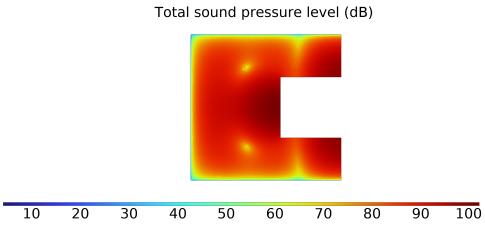

(c) c

Figure A.1: SPL along Z for Ma = 0.05 and f = 500Hz

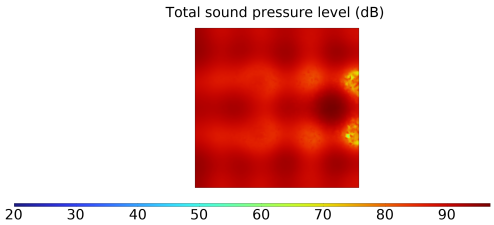

(a) a

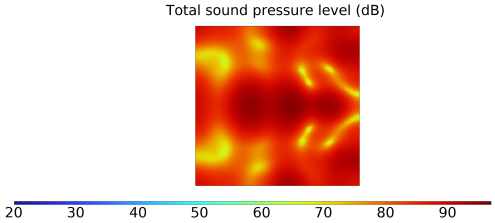

(b) b

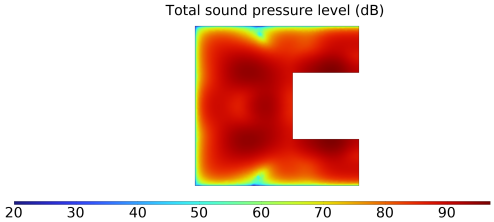

(c) c

Figure A.2: SPL along Z for Ma = 0.05 and f = 1000Hz

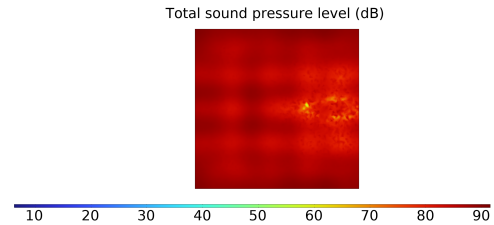

(a) a

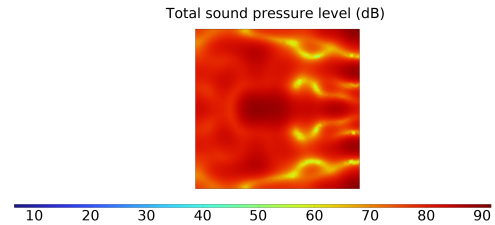

(b) b

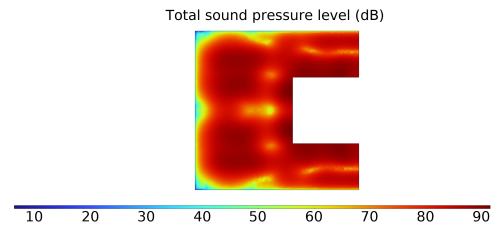

(c) c

Figure A.3: SPL along Z for Ma = 0.05 and f = 1500Hz

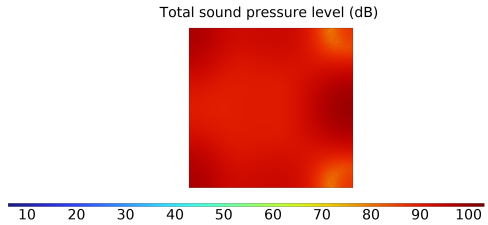

(a) a

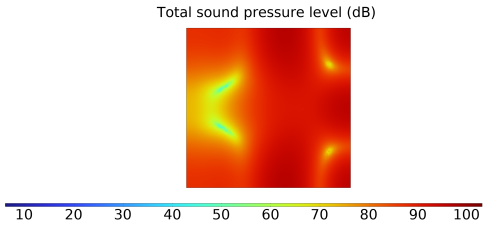

(b) b

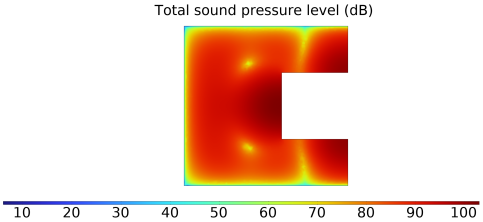

(c) c

Figure A.4: SPL along Z for Ma = 0.1 and f = 500Hz

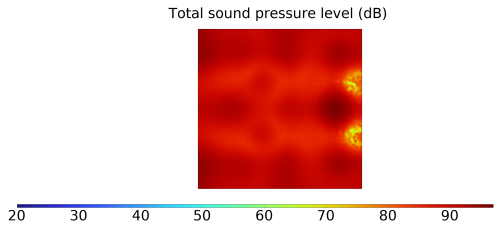

(a) a

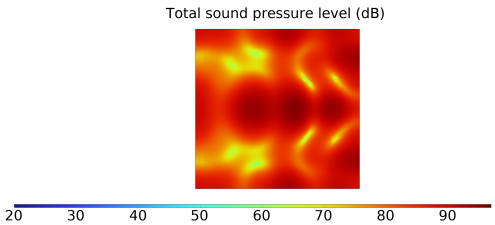

(b) b

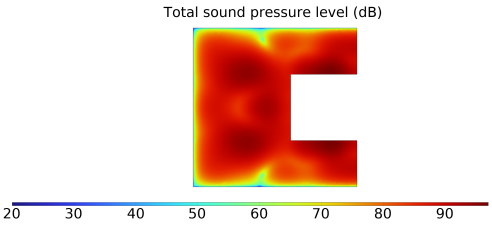

(c) c

Figure A.5: SPL along Z for Ma = 0.1 and f = 1000Hz

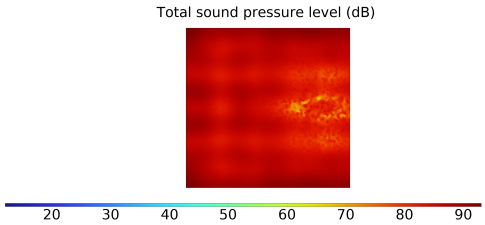

(a) a

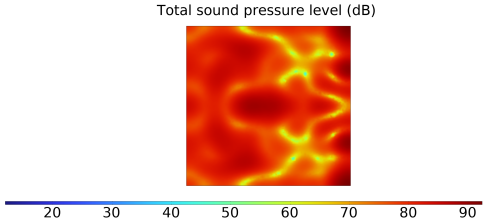

(b) b

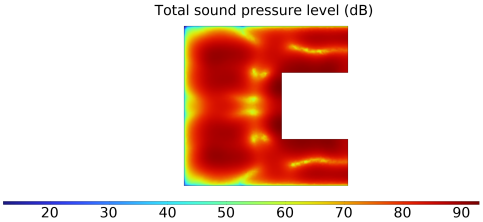

(c) c

Figure A.6: SPL along Z for Ma = 0.1 and f = 1500Hz

B

Appendix B

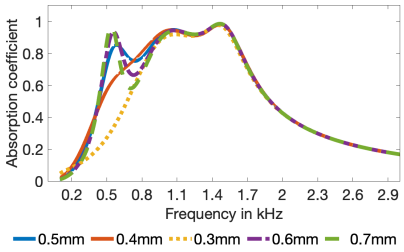

(a) d3

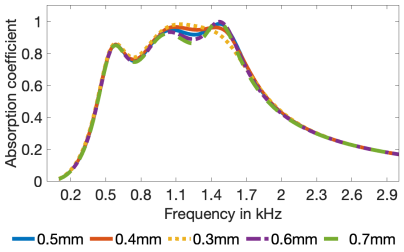

(b) d2

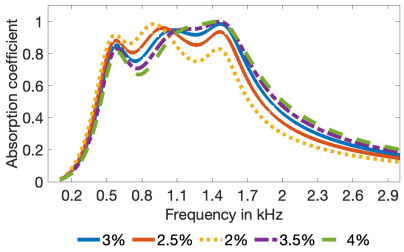

(c) p1

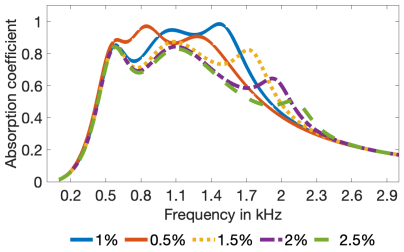

(d) p2

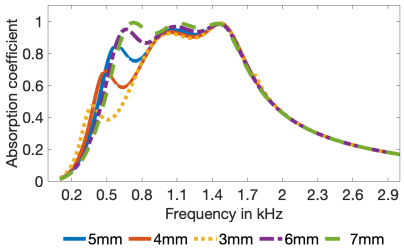

(e) R3

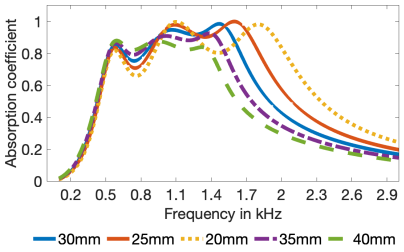

(f) D1

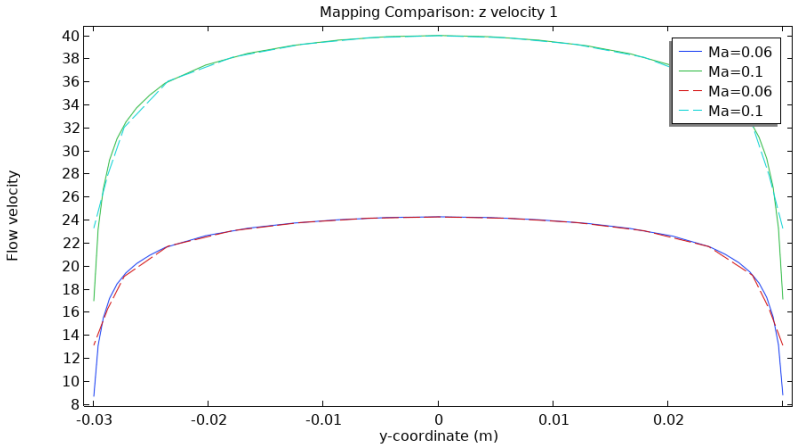

(g) Mapped value of the axial velocity

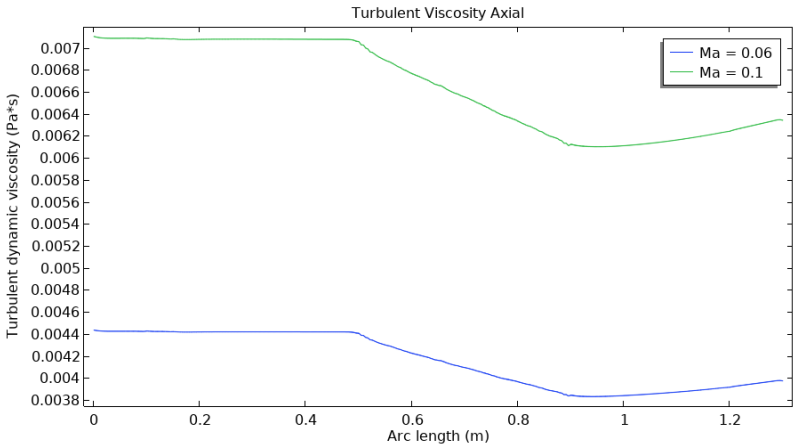

(h) Mapped value of the turbulent viscosity

Figure B.2: Mapped value compared to the value as evaluated on the CFD mesh

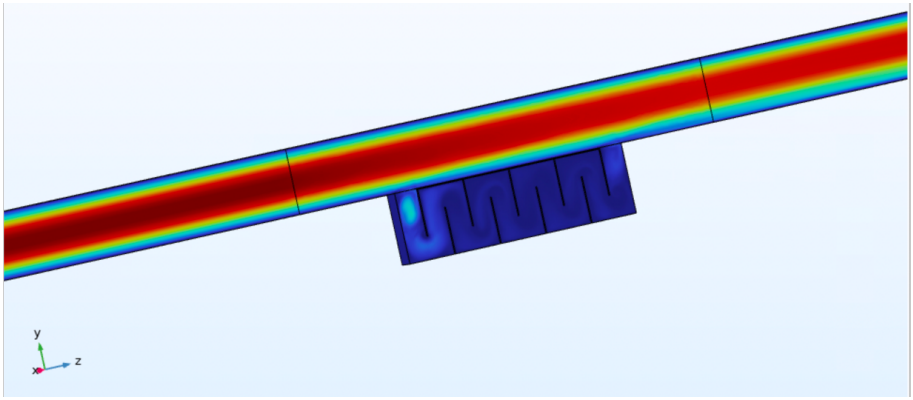

Figure B.3: Air viscosity Ma= 0.06

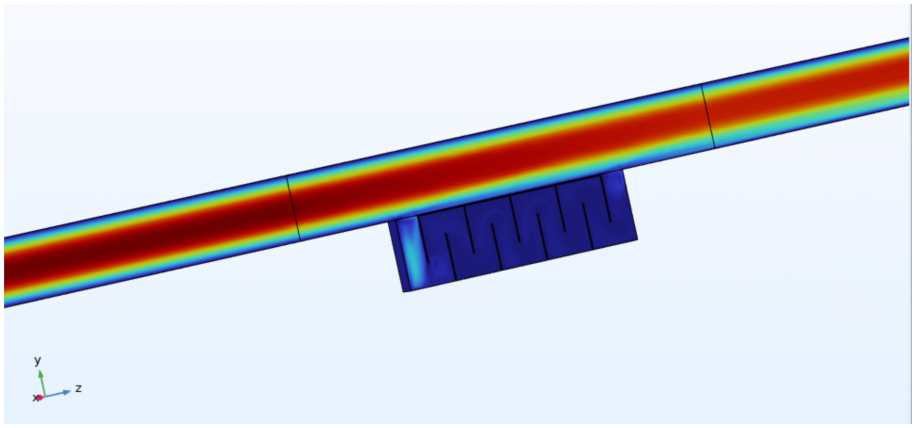

Figure B.4: Air viscosity Ma= 0.1

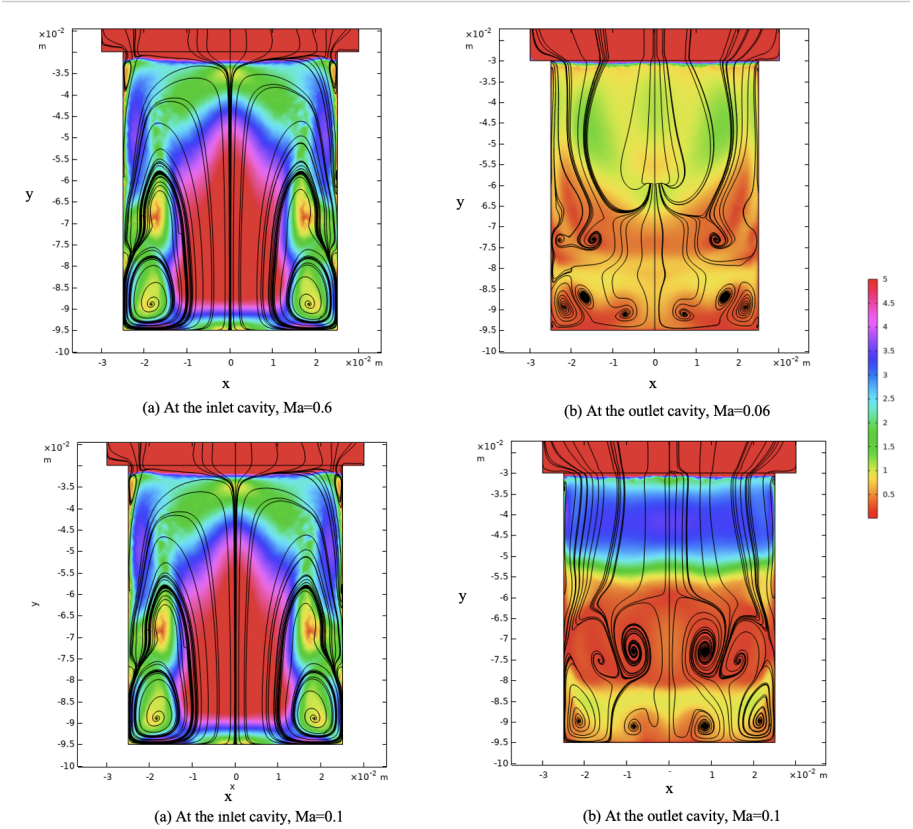

Figure B.5: Flow velocity in m/s and stream along Z at the inlet and outlet.

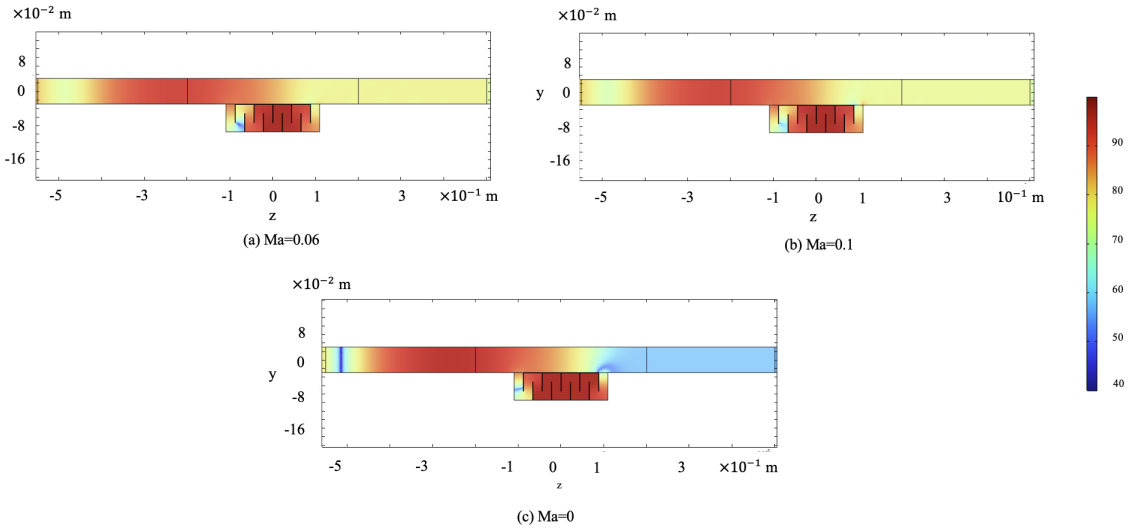

Figure B.6: SPL in dB at 330Hz

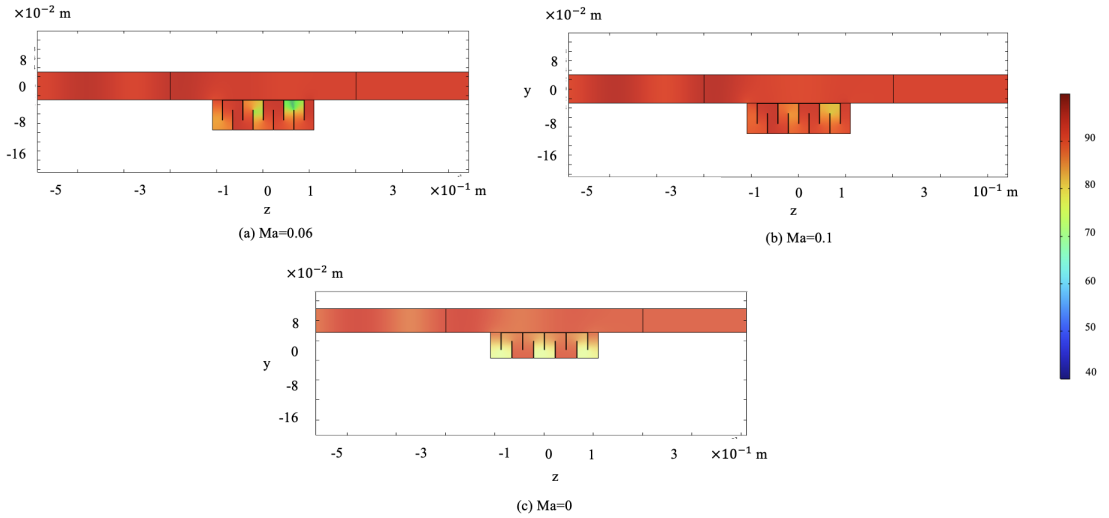

Figure B.7: SPL in dB at 816Hz

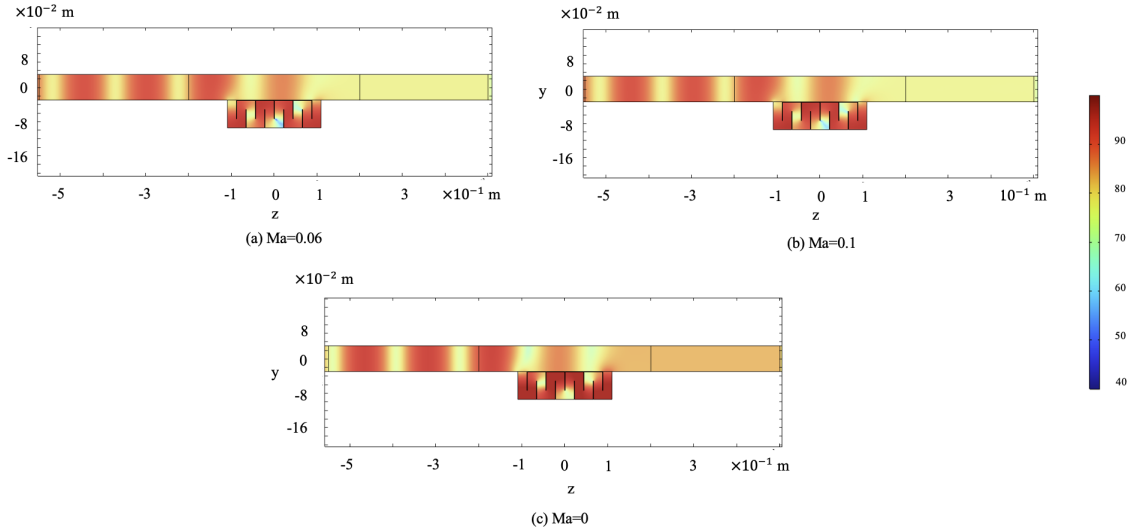

Figure B.8: SPL in dB at 1160Hz

DEPARTMENT OF SOME SUBJECT OR TECHNOLOGY
CHALMERS UNIVERSITY OF TECHNOLOGY
Gothenburg, Sweden
www.chalmers.se

CHALMERS
UNIVERSITY OF TECHNOLOGY